Bridging the Gap between Optical and RF Antennas: An Optical Patch Antenna Design inspired by RF Cavity Model

by

Gül Seda Ünal

Submitted to the Graduate School of Sciences and Engineering
in partial fulfillment of the requirements for the degree of

Doctor of Philosophy in Electrical and Electronics Engineering

at the

KOÇ UNIVERSITY

September 2014

Abstract

Optical antennas are still in infancy as compared to their RF counterparts although they have been proposed and studied with variety of shapes and for variety of applications. One would have expected that the maturity of RF antennas, both in design and analysis, would have had a more pronounced effect in the development of optical antennas. So far, optical antennas have only utilized the geometrical attributes of the RF antennas, but none of the analysis tools that provided a great deal of intuition to antenna engineers in the design of RF antennas.

This study intends to narrow the gap by introducing an easy-to-understand and easy-to-implement analysis tool, commonly known as the cavity model, for RF patch antennas into the optical regime.

Of course, due to some fundamental differences between RF and optical antennas, mapping the entirety of the cavity model and the functionality of patch antennas into optics may not be possible at all, or may require further studies.

The importance of this approach is not because of its simplicity in understanding and implementation, rather its applicability to a broad class of patch antennas, such as rectangular, circular, triangular, etc., with a wealth of applications developed in RF, and more importantly its ability to provide intuition with which one can assess the outcome (radiation pattern, polarization, impedance matching, loading and tuning antenna properties, etc.) without going through complex trial-and-error simulation studies with no or very little intuitive guidance by the user. This study intends to open up a new gateway full of new design approaches, functionalities and intuitions in optical antennas.

Keywords: plasmonics, nano-optics, nano-photonics, optical antenna, RF antenna, patch antenna, cavity model

Özetçe

Optik antenler çeşitli geometrilerde ve farklı uygulamalar için önerilmiş ve çalışılmıştır. Ancak RF antenlerle karşılaştırıldıklarında optik antenlerin henüz olgunlaşmadıkları görülür. RF antenlerin çok gelişmiş tasarım ve analiz yöntemlerinin optik antenlerin gelişiminde de etkili olması beklenir. Oysa ki optik antenler RF antenlerin sadece geometrilerini miras almış olup RF anten tasarımında mühendislere öngörü saglayan önemli analiz teknikleri henüz optiğe uyarlanamamıştır.

Bu çalışma iki frekans bölgesi arasındaki boşluğu kapatmak üzere bir köprü niteliğinde olup anlaşılması ve uygulaması çok basit bir RF yama anten analiz yöntemi olan kavite modelini optik antenler için önermektedir.

RF ve optikteki önemli birtakım farklılıklar sebebiyle kavite modelini ve yama antenlerin işlevselliğini tamamen optiğe eşleştirmek mümkün olmayabilir ya da daha ileri araştırmalar gerektirebilir. Bu çalışmanın amacı optik antenler için yeni tasarım yaklaşımları, işlevsellik ve öngörü sağlayan bir kapı açmaktır.

Bu yaklaşımın önemi sadece kolay anlaşılabilir ve uygulanabilir oluşu değil, dairesel, üçgensel, dikdörtgensel gibi radyo frekanslarında çok geniş uygulama alanı bulmuş çeşitli yama anten geometrilerine uygulanabilir oluşu ve daha da önemlisi sezgiden uzak deneme yanılma tekniklerinin aksine çok geniş öngörüye olanak sağlamasıdır.

Anahtar Kelimeler: plazmonik, nano-optik, nano-fotonik, optik anten, RF anten, yama anten, kavite modeli

Acknowledgments

Contents

List of Figures

9

10

11

12

13

List of Tables

Chapter 1

Introduction

Antennas are indispensable parts of all natural and man-made communication systems operating over almost the entire spectrum, when the terms *antenna* and *communications system* are used in a broader sense. Nature seems to have perfected the use of antennas in optical frequencies to harvest the light energy in photosynthetic systems through natural selection [1], in addition to all other frequencies with many different functionalities, while man-made systems have been employing them for about a century to control and manipulate electromagnetic radiation, having almost matured in the radio frequency (RF) band after having gone through market (military and commercial) selection [2–5]. Therefore, a wealth of knowledge and experience on the design and analysis is available in RF regime with a potential of use in the optical regime. However, with such a background on the topic, albeit over different frequency bands, it has been only recently that some use of antennas entered into man-made optics [6–11]. Their late arrivals in man-made optical systems were mainly due to the lack of fabrication techniques with nanometer precision. Once fabrication techniques have been improved to yield geometries with a few nanometers precision and become accessible to researchers in universities and research labs, there has been a flurry of activities and interests in optical antennas and their applications [12–25]. However, optical antennas have mainly exploited the geometric shape of RF antennas (dipole, bow-tie, yagi uda, etc.) and some of their fundamental performance characteristics, such as radiation pattern, directivity and gain, input impedance etc., even

though there are a few well-developed, tested and successfully utilized analysis and design tools in RF, apart from the full-wave approaches like Finite Element Method (FEM) [26], Finite-Difference Time Domain Method (FDTD) [27,28] and the Method of Moments (MoM) [29], that may provide some additional boost to the development and understanding of the potential of optical antennas [22,30]. Inspired by this assessment, in this study, we have focused on the transfer of accumulated knowledge in one of the most widely employed and versatile antenna configurations in RF, the patch antennas, also known as microstrip antennas, to the optical frequencies, with special emphasis given to their modeling and computational aspect [2]. To achieve this goal, the crucial step is to establish an equivalence, or some sort of mapping, of patch antennas in RF to those in optics, while maintaining the integrity of the model in RF that helps efficiently analyze and design the antenna as well as providing intuition upon the operation of the antenna.

The patch antennas, upon their ideation in 1950's [31] and realization in 1970's [32], have been one of the most studied and innovative classes of antenna work in RF, with several variations in patch shape, feeding and substrate configurations, array implementations, analytical and semi analytical models and design techniques [33]. They are still in demand in RF because of system requirements for antennas with low-profile, low-weight, low-cost, easy integrability, polarization diversity, or dual or multiple functionalities [34]. However, at least for now, most of these advantages of patch antennas in RF may not directly translate to optical frequencies, but some, like polarization diversity, dual or multiple functionalities and the variety in design may become useful in optics to some degrees.

A typical configuration of a patch antenna consists of a piece of metal trace on a substrate backed by a metal ground plane, as shown in Fig. 1-1 for a rectangular patch shape.
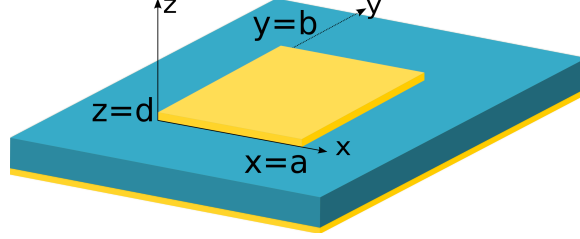
Figure 1-1: A typical rectangular RF patch antenna. A metal trace with dimensions a and b and thickness d on a dielectric substrate backed by a ground plane.

Since the main goal of this study is to establish a proper equivalence and mapping between RF and optical patch antennas, in order to pave the way to design optical patch antennas with similar intuitions, ease and functionalities, the basic operation of patch antennas in RF, as referenced to Fig. 1-1 for an example, need to be summarized in a few sentences, as to provide context for the following discussions. Regardless of the operating mode, transmitting or receiving, currents on the patch and the associated fields between the patch and the ground plane are excited either by a feed or incident wave. Since the distance between the patch and the ground plane, i.e., the thickness of the substrate, is usually quite small as compared to the wavelength of operation, electric field components parallel to the ground plane must be very small throughout the substrate, resulting in only significant $E_z(x,y)$, $H_x(x,y)$ and $H_y(x,y)$ field components. If the characteristic length of the patch (a or b for the rectangular patch in Fig. 1-1) is close to $\lambda/2$ or its integer multiple, the patch element resonates and sustains relatively large currents and associated field amplitudes in the structure, becoming the source of radiation. Due to the equivalence theorem, there are mainly two models, or interpretations, to describe the radiation mechanism of such antennas. Either the antenna can be viewed as the patch with the resonating current on, or equivalently, as a cavity formed by the patch and the ground plane enclosed laterally by the slot-type radiators with the resonating field inside [35]. So, the cavity interpretation for the radiation has inspired a model, known as the cavity model, that has proven to be very efficient, intuitive, easy to understand and use for the analysis and design of patch antennas of some canonical shapes [36–38]. Perhaps the most crucial trait of the cavity model for optics is that it can provide an understanding

of the operating principles of such antennas, making it useful in design as well as in the determination of the limitations in the performance of the antenna, and in the development of new antenna configurations or modifications to an existing antenna design.

After having established a strong analogy between optical and RF antennas [30], and having developed fabrication techniques that can produce structures at nanometer precision [22], both of which are essential to realize the full potentials of antennas, there has been an intense study on the use of antennas in optics, ranging from infrared imaging [8], high-resolution microscopy [6, 9, 39, 40] to solar cells [41, 42], optical sensors [43], metasurfaces [44] and graphene detectors [45], and many more. It should be stressed here that, in most optical antenna applications, the term "design" of the antenna merely refers to the optimization of the dimensions of the antenna using one of the commercially available full-wave Maxwell solvers, like FDTD and FEM, which are widely used in optical antenna optimization [46, 47]. Although such rigorous full-wave Maxwell solvers are readily available and provide accurate results, they are usually burdened with a large number of discretization of the solution domain (usually surfaces for MoM and volumes for FEM and FDTD), and perhaps more importantly for the antenna design, they are impenetrable and incapable of providing any intuition to users. Motivated from such an intense study and the possibility of widespread use of antennas in optics, and the need for a design tool that builds intuition on the operation of antennas in optics, the cavity model for patch antennas, with all their bells and whistles in RF, are introduced and translated into the optical frequencies, despite the fact that material properties and wave-matter interaction are almost completely different in these two frequency regimes. The cavity model, by itself, is an important tool for the design of patch antennas, as it covers not only the rectangular patch but also other canonical shapes like circular, elliptic, triangular and their many variations as well, which is likely to inspire variety of functionalities and use of patch antennas in optics with similar ease and intuition as in their RF counterparts.

Even before the introduction of an intuitive tool, there have been a few applications of patch antennas in optics; to achieve a large Purcell factor, collection efficiency

19

and spectral width [48], or to achieve inter- or intra-chip optical communications and sensing [23], or to control the spontaneous emission rate and the radiation pattern of quantum dots [49]. Apart from their intended use in optics, the tools that are used to analyze these patch antennas have been either the simplest model, namely the transmission line (TL) model [2], with mediocre accuracy, little intuition and limited to rectangular patches only [23, 50], or the full-wave approach with good accuracy but no intuition at all [48, 49]. However, the one that has been an inspiration for this study is the design of optical patch antennas for single photon emission using surface plasmon (SP) resonance [48], where they considered a thin metallic patch to enhance the capabilities of single photon sources. Hence, we have realized that, to employ the cavity model, one does not need to have two parallel metal plates to form a cavity, instead a free-standing metal patch of one of the canonical shapes as provided in the following chapters, or the metal patch over a dielectric substrate, or the metal patch over a dielectric substrate backed by another metal plane can be considered as an optical patch antenna suitable for the cavity model, provided the complex reflection coefficients regarding the propagating SPs, the so called surface plasmon polaritons (SPP), from the edges of the patch can be obtained. The main difference relevant to the subject matter of this study is the wave-matter interaction at the interface between dielectric and metal, which manifests itself as surface currents in RF and SPPs in optics. The key idea behind the use of the cavity model in optics is that the SPP modes supported by the patch are equivalent to and agree well with the surface current distribution corresponding to one or combination of the modes of the cavity. From the basic principles, it is clear that the use of the cavity model for optical patch antennas is possible as long as the differences of the wave-matter interactions in these frequency regimes, and in turn, the resonance conditions are properly adressed.

Optical antennas are strongly analogous to their RF counterparts, however, there are some crucial differences in their scaling and physical properties since metals in the optical regime are no longer perfect conductors as in RF. With the introduction of the SPs, that mainly is due to the metal behavior in the optical domain, a wave-matter interaction at the subwavelength scales has been reached. The subwavelength

interaction is introduced with a significant emphasis on the metal behavior in the second chapter that is entitled the Light-Matter Interaction, for the reason that light designates the electromagnetic wave in optics. In Chapter 2, the metal behavior in the optical regime is investigated in detail with Drude model and the interband transitions. Drude model, interband transition contributions and the experimental Johnson and Christy results are discussed for their validity and limitations on the determination of the metal dispersion. The propagating and localized forms of the SPs are introduced, moreover, the propagating SPs on single and multi interfaces and the localized SPs on nanostructures are examined analytically and numerically.

The robust analogy between RF and optical antennas inspires a mapping between the two domains but there is a gap in between these two domains due to the metal behavior and the scaling. The metal behavior in optics, as discussed in the second chapter, causes the SP excitations which replace the RF surface currents in optics. So, the optical antenna resonant lengths need to be calculated so that SPPs generate the standing waves. Also, for a powerful mapping of the cavity model, the intrinsic wavenumber, at which the optical antenna resonates, needs to be observed accurately. Due to their nanometer sizes, optical antennas can no longer be fed by TLs, but instead they are excited via coupling to the emission from nearby scatterers. In Chapter 3, an effective wavenumber is defined and derived and the optical antenna excitation techniques are introduced.

The patch antennas in RF and the cavity model for their design is introduced in Chapter 4. Under the light of the previous chapters, a mapping of the cavity model to optics is proposed and with the analytical and computational results regarding the antenna modes and the corresponding radiation patterns the proposed mapping is proven to be highly accurate.

Knowing the current distribution of a mode of an equivalent cavity guides us where to locate the surce in order to excite that mode, and provides intuition on how to tune the resonance, radiation pattern and the polarization. In Chapter 5, inspired by the cavity model, tuning of the resonant frequency and feeding for the CP operation are examined. The resonance of the antenna by introducing a slot on the patch is

proven to be tuned as expected by the cavity model, yet needs to be further studied in order to count in various slot sizes. CP operation research launches a new degree of freedom, the orientation of the source, different from the RF point of view where CP is obtained upon feeding the antenna from specific locations.

Lastly, in Chapter 6, we have given a conclusive information over this study and proposed some ideas to overcome the challenges we have experienced. As a result of the enormous ongoing research in the optical antennas, there are some new ideas that need to be explored in the future.

With this study, we intend to bridge the gap between RF and optical regimes by introducing an easy-to-understand and easy-to-implement RF analysis tool, the cavity model, into optics. The importance of this approach is not its simplicity in understanding and implementation, rather its applicability to a broad class of patch antennas and more importantly its ability to provide intuition with which one can assess the outcome without going through trial-and-error simulations with no or little intuitive guidance by the user. We have focused on transferring accumulated knowledge in patch antennas, to the optical frequencies, with special emphasis on their modeling and computational aspect. As such, we aim to open up a new gateway full of new design approaches, functionalities and intuitions in optical antennas. It has been observed that the cavity model equivalent in optics has achieved the intended goal, i.e., providing intuition on the operation of the patch antennas. That is, the current distribution on the patch and the associated radiation pattern can now be imagined for a given location of the feed in optics as well. The same analysis and intuitions can now be carried onto a range of patch geometries that the cavity model can be used. In addition, some of the tools that have been used for the rf patch antennas, like adding slot to tune the resonance and designing the CP operation, have been proposed and implemented in optics.

Chapter 2

Light-Matter Interaction

Optical antennas increase the efficiency of light-matter interaction at subwavelength scales and provide high field enhancement, strong field localization and large absorption cross section. In a similar fashion to their RF counterparts, optical antennas control and manipulate electromagnetic waves and efficiently convert propagating radiation to localized fields, and vice versa. Despite the strong analogy, optical antennas are crucially different in their scaling and physical properties due to the lossy metal behavior in the optical domain. Metals at microwave and radiowave frequencies are highly reflective and do not let electromagnetic waves propagate through them. However, at higher frequencies towards the visible regime the field penetration increases leading to increased dissipation. The physics behind the light-matter interaction is mainly designated in the metal's complex dielectric function, $\epsilon(\omega)$.

In contrast to antennas, traditional optical devices like lenses, mirrors and diffractive elements cannot control electromagnetic fields on subwavelength scales. The sizes of such optical devices are restricted by the diffraction limit that imposes a minimum guided mode size of $\lambda/2n$ where n is a positive integer number. There has been a revolutionary progress and innumerable discoveries in the miniaturization of these devices following the foundation of the photonic crystals [51]. Yet, light-matter interaction at subwavelength scale has been reached only after the introduction of plasmon waveguides as the smallest devices with optical functionality [52].

A new way of photon modulation, Surface Plasmon (SP), is observed due to

the negative dielectric constants of the metal in the optical regime hence similar behavior cannot be reproduced in other spectral ranges because of the dispersive nature of the metals. The existence of the SPs is a feature of the interaction of metal nanostructure with light. The field of SP study, dealing with the unique optical properties of the metallic nanostructures and the subwavelength scale light-matter interactions, is named as *Plasmonics* by Harry Atwater's group at Caltech in 2001 and there has been an immense research on the field since then [52].

Optical antennas exploit the unique properties of metal nanostructures. Since metals no longer behave as ideal conductors at optical wavelengths metallic nanostructures exploit the SPs, hence achieve optimum interaction with optical fields. SPs are collective oscillations of the charges at the same frequency of outside electromagnetic wave but with a much shorter wavelength allowing the manipulation of light below the diffraction limit.

"There is plenty of room at the bottom"

Feynman, 1959 [53]

A lecture "There is plenty of room at the bottom" given by Richard Feynman at Caltech in 1959 is considered as a seminal event in the nanotechnology history for the reason that it inspired the conceptual beginnings of the field decades ago. And, nowadays nanometer scale optical interactions open up new phenomena and perspectives into the nanoworld driven by recent advances in nanofabrication capabilities, sample characterization technologies, and theoretical and numerical simulation tools.

This chapter is dedicated to the metal behavior in optics and its consequences in optical antenna design. In the first part of this chapter, the physical properties of the metal behavior in the optical domain will be explored in detail whereas in the second part SPs, a new light modulation technique, caused by this metal behavior will be investigated both for localized and propagating cases.

2.1 Optical Properties of Metals

Metals are highly reflective at frequencies up to the optical regime and do not let electromagnetic waves propagate through them, whereas at higher frequencies towards the near-infrared (near IR) and visible, penetration of the field into the metal increases. Dispersive nature of the metal, simply determined by the free movement of conduction electrons within bulk and interband excitations due to photons with energy exceeding the bandgap, is described via a complex dielectric function $\epsilon(\omega)$ [54].

In the presence of an electric field, an electron that is identified with a dipole moment $\vec{\mu} = e\vec{r}$ is displaced by $\vec{r}$. A macroscopic polarization defined in (2.1) per unit volume is observed upon cumulative effect of n free electrons as $\vec{P} = n\vec{\mu}$.

$$\vec{P}(\omega) = \epsilon_0 \chi_e(\omega)\vec{E}(\omega) \tag{2.1}$$

$\vec{D}(\omega) = \epsilon_0\vec{E}(\omega)$ and $\vec{E}(\omega) = \epsilon_0\vec{E}(\omega) + \vec{P}(\omega)$ are very well known properties that lead to (2.2) where χ_e is the dielectric susceptibility.

$$\epsilon(\omega) = 1 + \chi_e(\omega) \tag{2.2}$$

2.1.1 Drude Model

The Drude model is a fast and practical way for rough estimates and basic pictures of the theory of metallic conduction, albeit more precise comprehension need complexity analysis. In Drude model, the highly successful kinetic theory of gases is applied to a metal that is considered as a gas of electrons. Gas molecules are treated as identical solid spheres in the kinetic theory and their movement is assumed to be in straight lines until they collide with each other where time for a single collision is neglected. All forces between the particles are neglected as well, except for the forces during each collision [55].

In gases there is only one kind of particle, however in metals there are at least two, since the electrons are negatively charged but the metal is electrically neutral. Upon close neighborhood of atoms, valence electrons are assumed to be detached

and wander freely through metal whereas metallic ions intact and act as immobile positive charges. Kinetic theory is applied to the gas of conductive electrons which has a number of n electrons with a mass of m_e per electron and moves against a background of positive immobile ions.

These electrons oscillate in response to the applied electromagnetic field and their motion is damped via collisions occurring with a characteristic collision frequency $\gamma = \frac{1}{\tau}$ where τ is the relaxation time of free electron gas and γ is the damping term.

The equation of motion for an electron of plasma sea is given in (2.3) where e is the charge of free electrons and $\vec{E}$ is the applied electric field.

$$m_e \frac{\partial^2 \vec{r}}{\partial t^2} + m_e \gamma \frac{\partial \vec{r}}{\partial t} = e\vec{E} \tag{2.3}$$

Damping term is given by $\gamma = \frac{v_F}{l}$ where v_F is the Fermi velocity and l is the electron mean free path between scattering events.

Considering the time harmonic driving field, $\vec{E} = \vec{E}_0 e^{-i\omega t}$ (2.3) changes into (2.4) which can be reorganized as (2.5) for $\vec{r}_0$.

$$m_e(-\omega^2)\vec{r}_0 e^{-i\omega t} + m_e \gamma(-i\omega)\vec{r}_0 e^{-i\omega t} = e\vec{E}_0 e^{-i\omega t} \tag{2.4}$$

$$\vec{r}_0 = \frac{e\vec{E}_0}{-m_e(\omega^2 + i\omega\gamma)} \tag{2.5}$$

Displaced electrons contribute to the macroscopic polarization in (2.1) as $\vec{P} = n\vec{\mu} = ne\vec{r}$, so (2.6) can be obtained which then leads to (2.7) for $\chi_e(\omega)$ where ω_p is the plasma frequency.

$$ne\frac{eE_0}{-m_e(\omega^2 + i\omega\gamma)} = \epsilon_0 \chi_e(\omega)\vec{E}_0 \tag{2.6}$$

$$\chi_e(\omega) = \frac{ne^2/m_e\epsilon_0}{-(\omega^2 + i\omega\gamma)} = \frac{\omega_p^2}{-(\omega^2 + i\omega\gamma)} \tag{2.7}$$

Drude model for the dielectric constant can finally be derived as in (2.8) and (2.9) in separate real and imaginary parts.

$$\epsilon_{Drude}(\omega) = 1 + \chi(\omega) = 1 - \frac{\omega_p^2}{\omega^2 + i\omega\gamma} \tag{2.8}$$

$$\epsilon_{Drude}(\omega) = 1 - \frac{\omega_p^2}{\omega^2 + \gamma^2} + i\frac{\gamma\omega_p^2}{\omega(\omega^2 + \gamma^2)} \tag{2.9}$$

Drude model gives quite accurate results for photon energies below the threshold of transitions between the electronic bands of the metals. It needs to be supplemented in the visible region by the response of the bound electrons. The failures of this model have found their solutions in the rich and subtle stucture of quantum theory of solids. Further details on the assumptions of Drude model and their consequences are beyond the scope of this study.

2.1.2 Interband Transitions

Since higher energy photons can promote electrons of lower-lying bonds into the conduction band, the measured imaginary part of the dielectric function increases much more strongly than the Drude model predictions. The inadequacy of the Drude model in describing the optical properties of gold and silver at visible frequencies can be overcome by the equation of motion (2.10) for a bound electron with an effective mass m and damping Γ (mainly radiative damping in the case of bound electrons) and resonance frequency ω_0.

$$m_e\frac{\partial^2\vec{r}}{\partial t^2} + m_e\Gamma\frac{\partial\vec{r}}{\partial t} + m_e\omega_0^2\vec{r} = e\vec{E} \tag{2.10}$$

(2.11) can be observed by representing (2.10) in time harmonic form.

$$m_e(-\omega^2)\vec{r_0}e^{-i\omega t} + m_e\Gamma(-i\omega)\vec{r_0}e^{-i\omega t} + m_e\omega_0^2\vec{r_0}e^{-i\omega t} = eE_0e^{-i\omega t}. \qquad (2.11)$$

The motion of electrons, $\vec{r_0}$, can be observed as in (2.12) by organizing (2.11).

$$\vec{r_0} = \frac{eE_0}{m_e(\omega_0^2 - \omega^2) - im_e\omega\Gamma} \qquad (2.12)$$

A similar procedure to Drude model derivations can be followed in order to obtain the complex dielectric function in (2.13) for the interband transitions.

$$\epsilon_{interband}(\omega) = 1 + \frac{w_p^2}{(\omega_0^2 - \omega^2) - i\omega\Gamma} \qquad (2.13)$$

Gold and silver are the most important metals for plasmonics studies in the visible and near-IR regions although there are other promising plasmonic materials like silicon, germanium, III-V semiconductors, transparent conducting oxides and many other oxides and sulfides recently proposed for different applications [56].

Considering gold as an example for noble metals, in Figure 2-1 the metal behavior in the visible regime can be better understood. The negative real part of the dielectric constant implies a strong imaginary part of the refractive index ($n = \sqrt{\epsilon}$) and leads to penetration of light into the metal, whereas the imaginary part describes the dissipation of energy associated with the motion of electrons in the metal. Contribution of the bound electrons to the dielectric constant is also given in Figure 2-1 through the interband transitions. A clear resonance behavior is seen for the imaginary part, whereas dispersion-like behavior is observed for the real part.
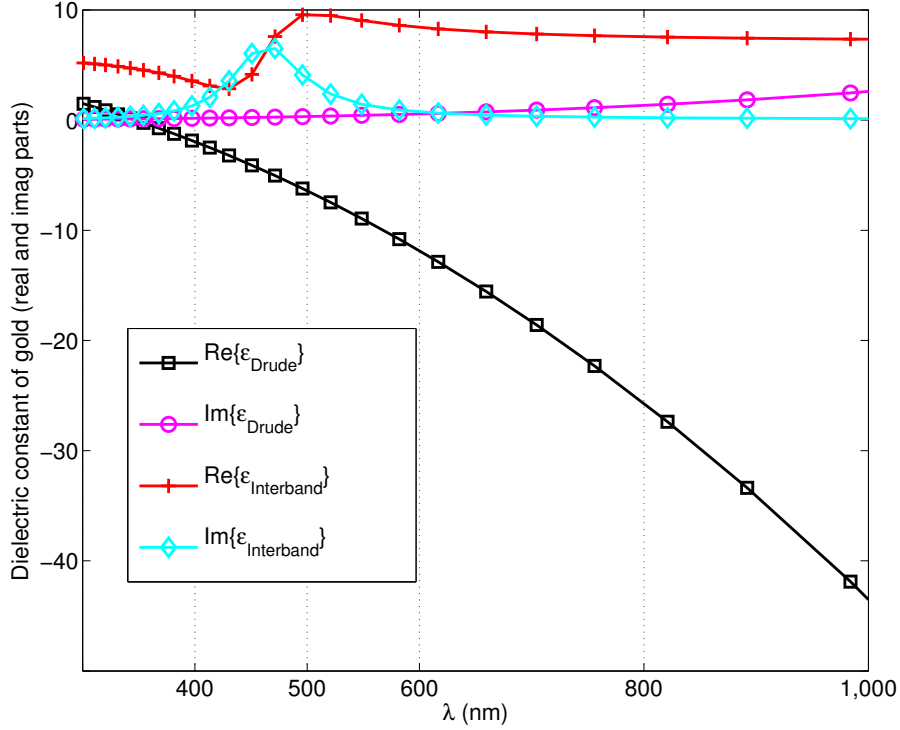
Figure 2-1: Real and imaginary parts of the dielectric constant of gold obtained analytically via Drude model and the interband contributions. Squares and circles demonstrate the real and imaginary parts of the dielectric constant of gold calculated using Drude model. Pluses and diamonds demonstrate the real and imaginary parts of the dielectric constant of gold by counting in the interband transmissions.

In Figure 2-2 the dielectric constant from the experimental Johnson and Christy data for gold is given with comparison to Drude model results incorporated with interband transmissions [57]. Both the experimental Johnson and Christy data and the Drude-Interband results have a similar behavior for wavelengths above 500nm. When Drude model is taken into account without the interband transitions, the results do not match below 650nm [54]. Considering only one interband transition improves the Drude model results, although the results cannot capture the Johnson and Christy data below 500nm.
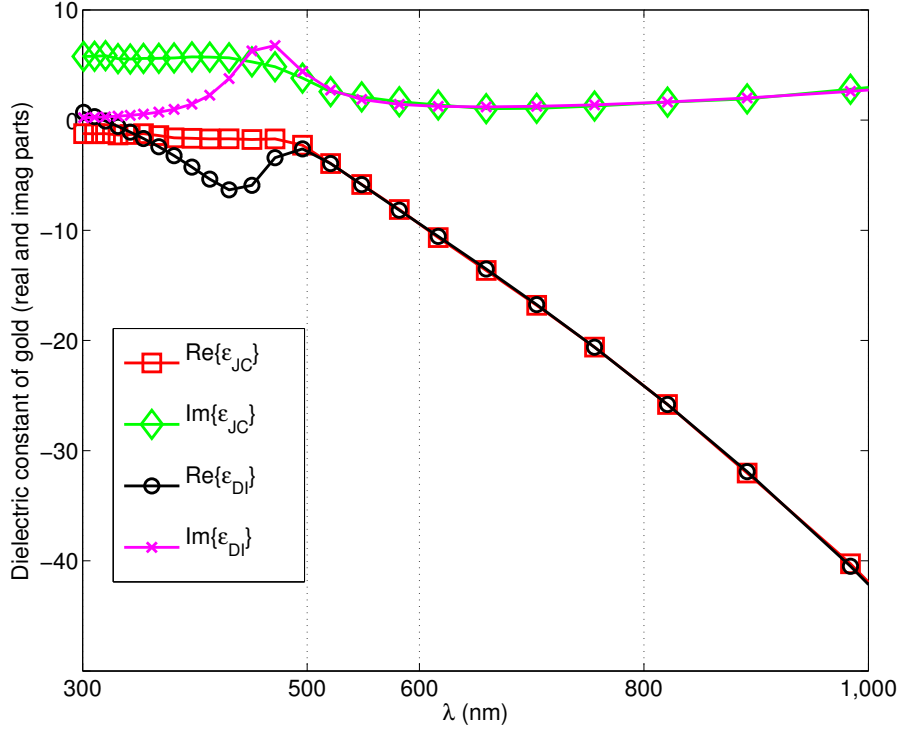
Figure 2-2: Comparison of the real and imaginary parts of the dielectric constant of gold calculated using i) Drude model including the interband transition contribution and ii) the experimental Johnson and Christy data. Squares and diamonds demonstrate the real and imaginary parts of the dielectric constant taken from experimantally obstained Johnson and Christy data, whereas the circles and crosses demonstrate the real and imaginary parts of the dielectric constant of gold calculated using the Drude model with the interband transitions. Drude model is improved with the interband transitions but still cannot reach the experimental data for wavelengths below 500nm.

In Appendix A, complex dielectric function expressions using Drude model with the interband transition contributions are supplied for metals: gold, silver, aluminum and nickel. Experimental Johnson and Christy data for the refractive index of gold and silver are also provided in Tables 7.1 and 7.2, respectively.

2.2   Surface Plasmons

Existence of self-sustained collective oscillations at metal surfaces is first predicted in 1957 by Ritchie in his pioneering study of characteristic energy losses of fast electrons passing through thin metal films [58] and demonstrated in a series of electron energy

loss experiments in 1959 by Swan and Powell [59, 60] and named as surface plasmon in 1960 by Stern and Ferrell [61]. SPs are widely recognized and both experimentally and theoretically investigated since then.

SPs are of great interest to physicists, chemists, metarial scientists, biologists and engineers due to the recent advances in structuring and characterizing metals at nanometer scale with the aid of control over specific applications with potentials in optics, magneto-optic data storage, microscopy, solar cells and such [62]. In plasmonics, one of the most attractive aspects of SPs is its capability to concentrate and channel light using subwavelength structures which lead to miniaturized devices.

SPs are light waves that are trapped on the surface because of their interaction with the free electrons of a conductor, metal. In this interaction the electromagnetic waves together with the surface charge oscillations generate SP. Surface Plasmon Polaritons (SPPs) are propagating dispersive electromagnetic waves coupled to free electrons of a conductor at a dielectric interface, whereas Localized Surface Plasmons (LSPs) are non-propagating excitations of the conduction electrons of metallic nanostructures coupled to the electromagnetic field [63]. In this section, fundamentals of the SPPs on single and multilayer interfaces and LSPs on nanostructures will be surveyed with a slight touch on their dispersive nature, excitation techniques and resonance conditions.

2.2.1   Surface Plasmon Polaritons

SP is a quasiparticle resulting from the quantization of surface charge density oscillations that is used to define the collective oscillations in the electron density at the metal surface where these oscillations naturally couple to electromagnetic waves appointing *polaritons* [54]. A homogeneous solution, the eigenmode of the system that is solved without external excitation, of the wave equation (2.14) define the electromagnetic behavior of the SPPs in any system under the appropriate boundary conditions.

$$\nabla \times \nabla \times \mathbf{E}(\mathbf{r}, \omega) - \frac{\omega^2}{c^2} \epsilon(\mathbf{r}, \omega) \mathbf{E}(\mathbf{r}, \omega) = 0 \tag{2.14}$$

Using the identity $\nabla \times \nabla \times \mathbf{E} = \nabla(\nabla \cdot \mathbf{E}) - \nabla^2 \mathbf{E}$ and remembering the absence of external excitation $\nabla \cdot D = 0$ the wave equation can be reorganized as in (2.15)

$$\nabla(\frac{1}{\epsilon(\mathbf{r}, \omega)} \mathbf{E}(\mathbf{r}, \omega) \cdot \nabla \epsilon(\mathbf{r}, \omega)) - \nabla^2 \mathbf{E}(\mathbf{r}, \omega) - \frac{\omega^2}{c^2} \epsilon(\mathbf{r}, \omega) \mathbf{E}(\mathbf{r}, \omega) = 0 \tag{2.15}$$

The negligible variation of the dielectric profile over distances on the order of λ ($\nabla \epsilon(\mathbf{r}, \omega) \to 0$) leads to the Helmholtz equation (2.16) which is the starting point of the general SPP analysis. A similar representation for the magnetic field can be observed naturally, as well.

$$\nabla^2 \mathbf{E}(\mathbf{r}, \omega) + k^2 \epsilon(\mathbf{r}, \omega) \mathbf{E}(\mathbf{r}, \omega) = 0 \tag{2.16}$$

Semi Infinite System

The SPP analysis for a planar interface between two media, one with a complex, frequency dependent dielectric constant $\epsilon_1(\omega)$ and the other with a real dielectric constant ϵ_2 (Figure 2-3) can be done by solving the Helmholtz equation (2.16) with $\epsilon(\mathbf{r}, \omega) = \epsilon_1(\omega)$ if $z < 0$ and $\epsilon(\mathbf{r}, \omega) = \epsilon_2(\omega)$ if $z > 0$.
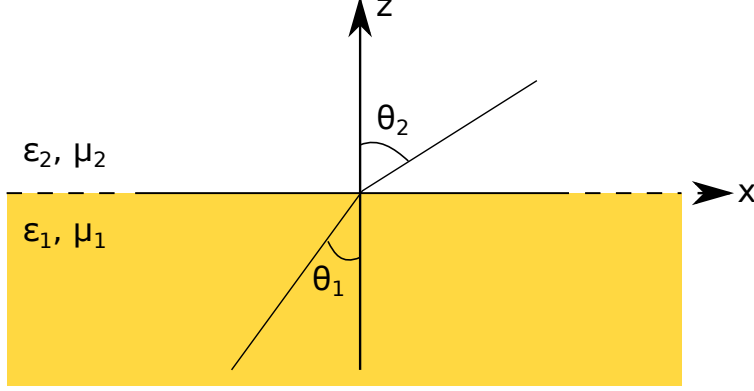
Figure 2-3: SPP excitation at a single metal-dielectric interface where the one of the regions ($z < 0$ in this figure) is a metal with dielectric constant $\epsilon_1(\omega)$ and the other medium ($z > 0$) is a dielectric with a real dielectric constant $\epsilon_2(\omega)$.

SPP excitation is achieved only for TM polarization which is easy to comprehend just by looking at the reflection coefficients. The Fresnel reflection coefficient for the TM polarized incidence in a simple two layer system, given in (2.17), in order to generate SPP at the interface in Figure 2-3, enforces $k_{z1} \neq k_{z2}$ upon maximum reflection of the incidence at the interface showing maximum transmission radiation.

$$R_{TM} = \frac{\epsilon_1 k_{z2} - \epsilon_2 k_{z1}}{\epsilon_1 k_{z2} + \epsilon_2 k_{z1}} \tag{2.17}$$

TE polarized incidence, on the other hand, would impose equal perpendicular wave numbers (k_z's) as easily seen in (2.18) since $\mu_1 = \mu_2$. The continuity is only satisfied for parallel component, k_x.

$$R_{TE} = \frac{\mu_1 k_{z2} - \mu_2 k_{z1}}{\mu_1 k_{z2} + \mu_2 k_{z1}} \tag{2.18}$$

SPPs are dispersive electromagnetic waves that propagate at a metal-dielectric interface where a negative permittivity metal exists. The field normal to the surface is evanescent, and decays exponentially with distance from the surface while SPP propagates along the surface. SPP modes on a planar metal surface are bound to the

surface and propagates until their energy is dissipated as heat in the metal. Hence, a TM polarized illumination originates SPP that propagates in x-direction and decays in z-direction which can be defined as $\mathbf{E}(x,y,z) = \mathbf{E}(z)e^{i\beta x}$ where $\beta = k_x$ is the propagation constant of the traveling wave and corresponds to the component of the wavevector in the propagation direction.

The solution to the Helmholtz equation (2.16) can be used to determine the spatial field profile and dispersion relation of the propagating waves, once the time harmonic electric and magnetic field components are explicitly expressed as coupled equations by using the curl (Faraday and Ampere) relations. These identities can be found in any Electromagnetics textbook, here only the governing equations for TM mode components E_x, E_z and H_y are given in (2.19).

$$
\begin{aligned}
E_x &= -i\frac{1}{\omega\epsilon_0\epsilon}\frac{\partial H_y}{\partial z} \\
E_y &= -\frac{\beta}{\omega\epsilon_0\epsilon}H_y \\
\frac{\partial^2 H_y}{\partial z^2} &+ (k_0^2\epsilon - \beta^2)H_y = 0
\end{aligned}
\tag{2.19}
$$

Using (2.19) in both half spaces yields (2.20) for $z < 0$ and (2.21) for $z > 0$.

$$
\begin{aligned}
H_y(z) &= A_1 e^{i\beta x}e^{k_{z1}} \\
E_x(z) &= -iA_1\frac{k_{z1}}{\omega\epsilon_0\epsilon_1}e^{i\beta x}e^{k_{z1}} \\
E_y(z) &= -A_1\frac{\beta}{\omega\epsilon_0\epsilon_1}e^{i\beta x}e^{k_{z1}}
\end{aligned}
\tag{2.20}
$$

$$
\begin{aligned}
H_y(z) &= A_2 e^{i\beta x}e^{-k_{z2}} \\
E_x(z) &= iA_2\frac{k_{z2}}{\omega\epsilon_0\epsilon_2}e^{i\beta x}e^{-k_{z2}} \\
E_y(z) &= -A_2\frac{\beta}{\omega\epsilon_0\epsilon_2}e^{i\beta x}e^{-k_{z2}}
\end{aligned}
\tag{2.21}
$$

The boundary conditions at $z = 0$ requires i) $A_1 = A_2$ due to continuity of H_y and ii) (2.22) due to contunuity of E_x where k_{zi}'s are as defined in (2.23).

$$\frac{k_{z2}}{k_{z1}} = -\frac{\epsilon_2}{\epsilon_1} \tag{2.22}$$

$$k_{z1}^2 = \beta^2 - k_0^2 \epsilon_1$$
$$k_{z2}^2 = \beta^2 - k_0^2 \epsilon_2 \tag{2.23}$$

Dispersion relation for the SPP can be observed as (2.24) upon combining (2.22) and (2.23) which is valid for conductors with or without attenuation.

$$\beta = k_x = k_{SPP} = k_0 \sqrt{\frac{\epsilon_1 \epsilon_2}{\epsilon_1 + \epsilon_2}} \tag{2.24}$$

The normal component of the wave numbers k_{zi} can be obtained as in (2.25). A bound mode on the interface can be reached if k_z's are purely imaginary in both media so that it gives rise to exponentially decaying solutions and this can only be achieved when the denominator in (2.25) is negative.

$$k_{zi}^2 = k_0^2 \frac{\epsilon_i^2}{\epsilon_1 + \epsilon_2} \tag{2.25}$$

The propagating nature of the SPP on the interface designates real k_x, which counting in the condition (2.26a) results in (2.26b).

$$\epsilon_1 + \epsilon_2 < 0 \tag{2.26a}$$

$$\epsilon_1 \epsilon_2 < 0 \tag{2.26b}$$

Therefore, the condition for the existence of the SPPs is that one of the dielectric constants must be negative with an absolute value exceeding the other. In order to excite SPPs both energy and momentum must be conserved which can be analyzed through dispersion relation. SPP properties like wavelength, propagation length and decaying length can also be analyzed via dispersion relation.

In order to accomodate the losses, a complex dielectric constant for the metal is considered as $\epsilon_1 = \epsilon_1' + i\epsilon_1''$ where ϵ_1' and ϵ_1'' are real. Then, parallel wavenumber $k_x = k_{SPP}$ can naturally be obtained as complex $k_x = k_x' + ik_x''$ where the real part k_x' determines the SPP wavelength λ_{SPP} as in (2.27) while imaginary part k_x'' accounts for damping of the SPP as it propagates along the interface.

$$\lambda_{SPP} = \frac{2\pi}{Re\{k_{SPP}\}} \tag{2.27}$$

The propagation length of the SPP, $1/e$ decay length of the electric field, is determined by k_x'' that is responsible for exponential damping of the electric field amplitude and is caused by the ohmic losses that finally result in the heating of the metal. Heating was considered as a disadvantage until recently, before the emerging research on the hot electrons. A recently proposed plasmonic energy conversion method based on the generation of hot electrons through electromagnetic decay of SPPs offers high conversion efficiencies with low cost for photovoltaic devices [64].

The $1/e$ decay length of the SPP electric fields away from the interface, by neglecting the imaginary parts can be observed from k_{zi}'s as $(1/k_{z1}, 1/k_{z2})$ for metal and dielectric respectively for the geometry in Figure 2-3. SPP electric field in z direction can pass through a thin enough metal film. Further discussion on thin films and the splitting SPPs due to the coupling will be given in the next section for three layer structures.

Dispersion relation shows two branches, one for high energy and one for low energy. The Brewster mode, high energy branch, does not describe a true surface wave since the normal component of the wavenumber is no longer purely imaginary. Low energy

branch corresponds to true interface wave, SPP. There is a continuous transition from SP dispersion into high energy branch when damping is fully considered. In Figure 2-4 the solid line is the light line in air that corresponds to $\omega = ck_x$. In the same figure, dispersion relations for gold-silica interface are demonstrated that are obtained via Drude Model with (pluses) and without (diamonds) interband transition contribution and via the experimental Johnson and Christy data (circles).
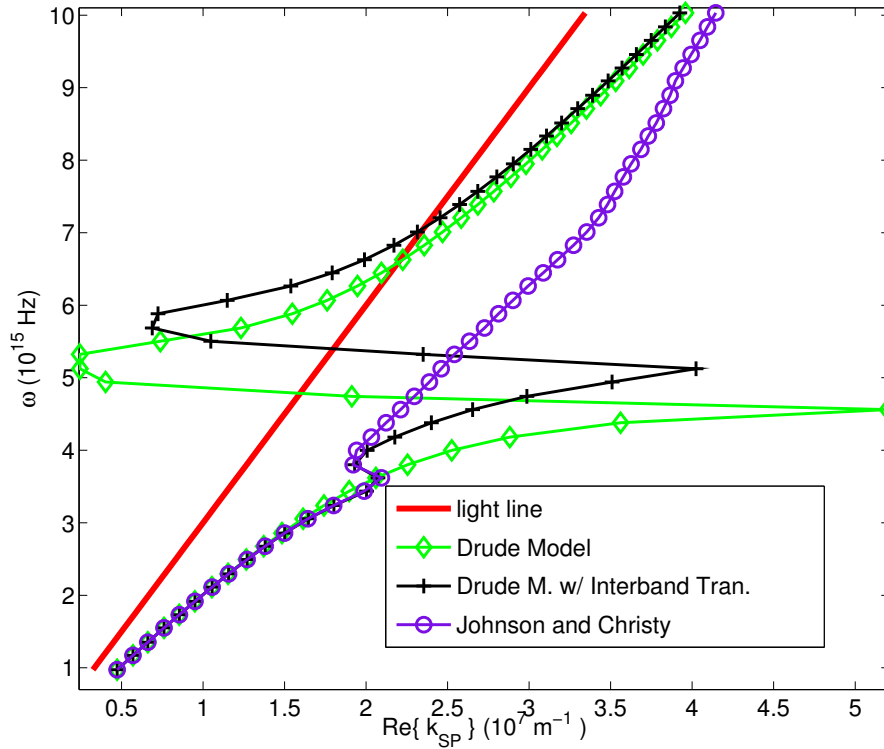
Figure 2-4: Dispersion diagram for SPP mode at gold-silica interface are obtained by using Drude Model (diamonds), Drude model with the interband transmissions contribution (pluses). The experimantal Johnson and Christy data is also shown (circles). Solid line is the light line. A backbending from low energy branch to high energy branch is seen. It posses a limit for maximum SP wavenumber, k_{SP}.
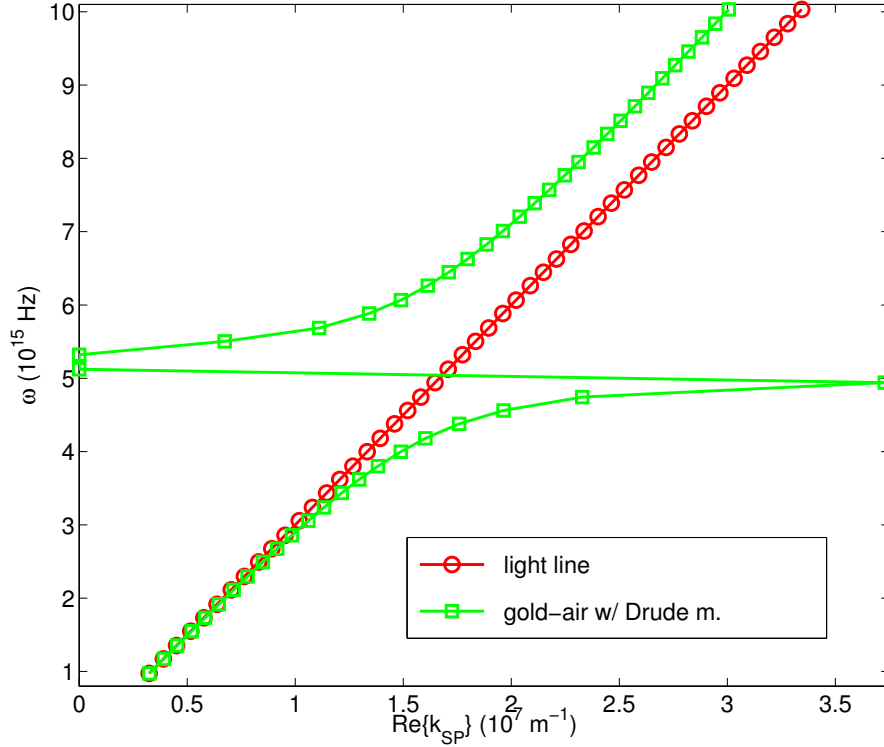
Figure 2-5: Dispersion relation of the SPP on the gold-air interface are obtained using only the real part of the dielectric function of gold.

Dispersion diagram for a gold-air interface can be obtained as in Figure 2-5 considering only the Drude model with the real parts of the dielectric constant. The high and low energy branches are clearly seen. The backbending effect has been verified experimentally [65]. It poses a limit to the maximum SPP wavenumber k_{SPP}.

An important consequence of the interaction between the surface charge density and the electromagnetic field is the momentum mismatch problem : momentum of the SP being greater than that of free space photon at the same frequency. The physical reason behind this momentum mismatch is the strong coupling between light and surface charges. In the form of an SPP, light drags electrons on the metal surface which can be pictured like light propagating with a cloud of electrons in the metal. Hence, SPP on the interface cannot be excited by light at any frequency, but by light with a wavevector component that can be increased over its free space value. There are many ways to achieve this behavior and couple light to SPPs known as the phase matching techniques on which details can be found elsewhere [54]. SPP dispersion

curve being on the right of the light's dispersion curve also proves that SPPs cannot be excited with conventional illumination from the adjacent dielectric.

SPPs have both transverse and longitidunal electromagnetic field components. Magnetic field is parallel to the surface and perpendicular to its propagation direction since only TM wave can excite the SPPs. Electric field has a component perpendicular to the surface and a component parallel to the propagation direction. Transverse component is the dominant electric field.

Two Interfaces

Single interface structure has been studied in the previous section on the semi infinite geometries and the corresponding SPP properties and dispersion relations are derived. There is a new degree of freedom due to coupling of the SPP modes introduced to the problem when two or more interfaces are considered. First, the two interface, three layer structure, will be investigated and that will be generalized to $N-$layer structures. Independent of the materials of each layer in Figure 2-6, the TM mode's H_y component can be expressed as (2.28).
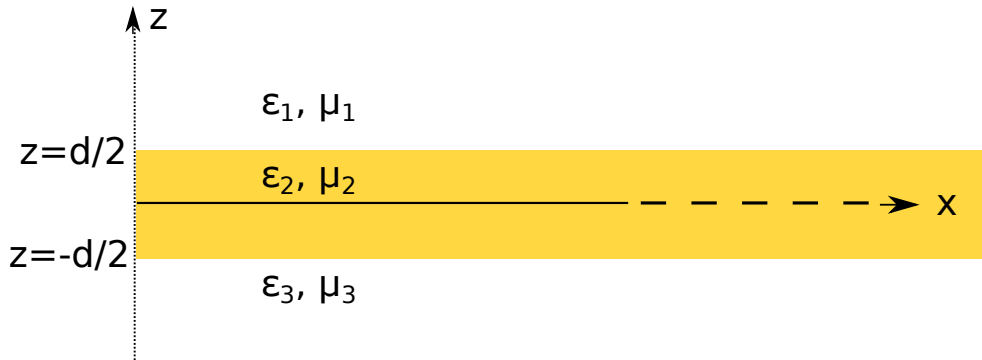
Figure 2-6: Three layers (two interfaces) structure.

$$
\begin{aligned}
\mathbf{H} &= \hat{y}Ae^{ik_{z1}z}e^{ik_x x}, & z &> d/2 \\
\mathbf{H} &= \hat{y}(Be^{ik_{z2}z} + Ce^{-ik_{z2}z})e^{ik_x x}, & -d/2 &< z < d/2 \\
\mathbf{H} &= \hat{y}De^{-ik_{z3}z}e^{ik_x x}, & z &< -d/2
\end{aligned}
\qquad (2.28)
$$

39

The electric field distributions in all three domains can be obtained as (2.29) applying the Ampere-Maxwell law to (2.28).

$$
\mathbf{E} = \hat{x}\frac{k_{z1}}{\omega\epsilon_1}Ae^{ik_{z1}z}e^{ik_x x} - \hat{z}\frac{k_x}{\omega\epsilon_1}Ae^{ik_{z1}z}e^{ik_x x},
$$

$$
z > d/2
$$

$$
\mathbf{E} = \hat{x}\frac{k_{z2}}{\omega\epsilon_2}(Be^{ik_{z2}z} - Ce^{-ik_{z2}z})e^{ik_x x} - \hat{z}\frac{k_x}{\omega\epsilon_2}(Be^{ik_{z2}z} + Ce^{-ik_{z2}z})e^{ik_x x},
$$

$$
- d/2 < z < d/2
$$

$$
\mathbf{E} = -\hat{x}\frac{k_{z3}}{\omega\epsilon_3}De^{-ik_{z3}z}e^{ik_x x} - \hat{z}\frac{k_x}{\omega\epsilon_3}De^{-ik_{z3}z}e^{ik_x x},
$$

$$
z < -d/2
$$

(2.29)

Applying the boundary conditions of the continuity of E_x and H_y at $z = d/2$ and $z = -d/2$, the transcendental equation, dispersion relation, can be observed as in (2.30). For infinite thickness $d \to \infty$ (2.30) reduces to the semi-infinite case derived previuosly in (2.24).

$$
e^{-2k_2 d} = \frac{k_2/\epsilon_2 + k_3/\epsilon_3}{k_2/\epsilon_2 - k_3/\epsilon_3}\frac{k_2/\epsilon_2 + k_1/\epsilon_1}{k_2/\epsilon_2 - k_1/\epsilon_1}
$$

(2.30)

Three layer structures with symmetry in terms of the dielectric functions like Metal-Insulator-Metal (MIM) or Insulator-Metal-Insulator (IMI) show an interesting special case of symmetric and anti-symmetric modes with dispersion relations in (2.31) and (2.32), respectively. Symmetry corresponds to even $E_x(z)$ mode (odd $H_y(z)$ and $E_z(z)$).

$$
tanh(k_2 d/2) = -\frac{k_1\epsilon_2}{k_2\epsilon_1}
$$

(2.31)

$$
tanh(k_2 d/2) = -\frac{k_2\epsilon_1}{k_1\epsilon_2}
$$

(2.32)
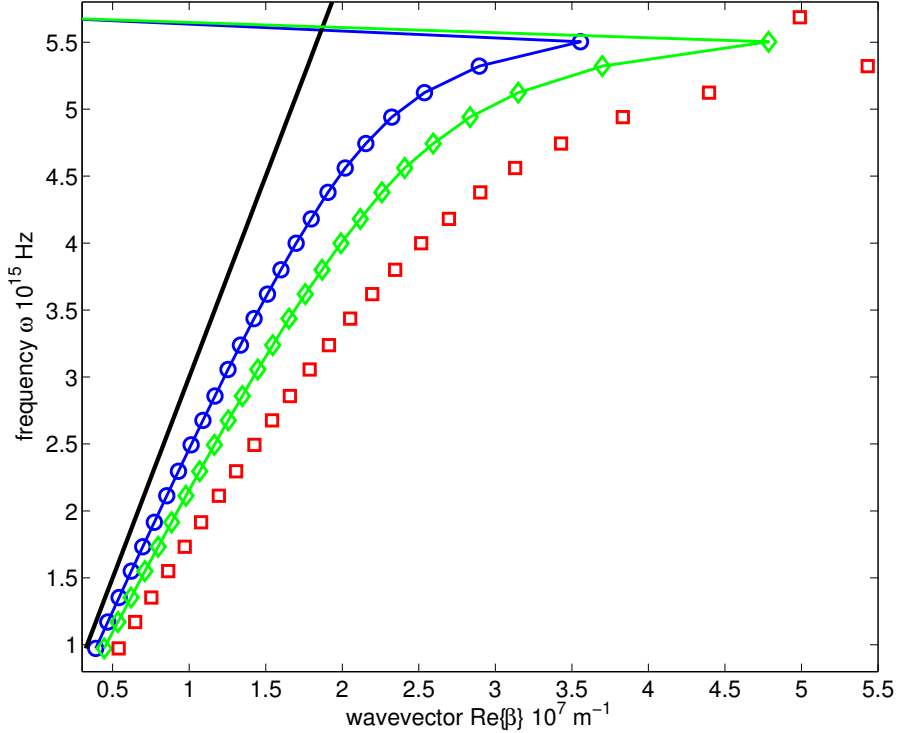
Figure 2-7: Dispersion relation of the symmetric SPP mode supported in Ag|air|Ag structure for an air core of thickness 25nm (squares), 50nm (diamonds), 100nm (circles). Also shown the light line (solid line). Johnson and Christy data is used for silver.

In the symmetric case of a three layer structure, two identical SPP modes may couple with each other when the mid-film is thin enough and form two distinct waves where the propagation constants of the symmetric and the anti-symmetric modes differ. Odd modes have higher frequencies whereas even modes have smaller frequencies. Figure 2-7 shows the dispersion relation of the fundamental symmetric mode of an MIM (Ag|air|Ag) structure for various dielectric thicknesses of $d_{air} = 100$nm, 50nm, 25nm where a backbending is observed for the k_{SP}.

In Figure 2-8 the low energy (symmetric) modes in the (Au|SiO$_2$|Au) structure is investigated for SiO$_2$ thicknesses of 100nm (squares), 50nm (stars), 10nm (diamonds), 5nm (circles). As seen in Figures 2-7 and 2-8, with the decreasing insulator thickness the wavenumbers increase for a specified excitation, and that corresponds to shorter wavelengths, λ_{SPP}.
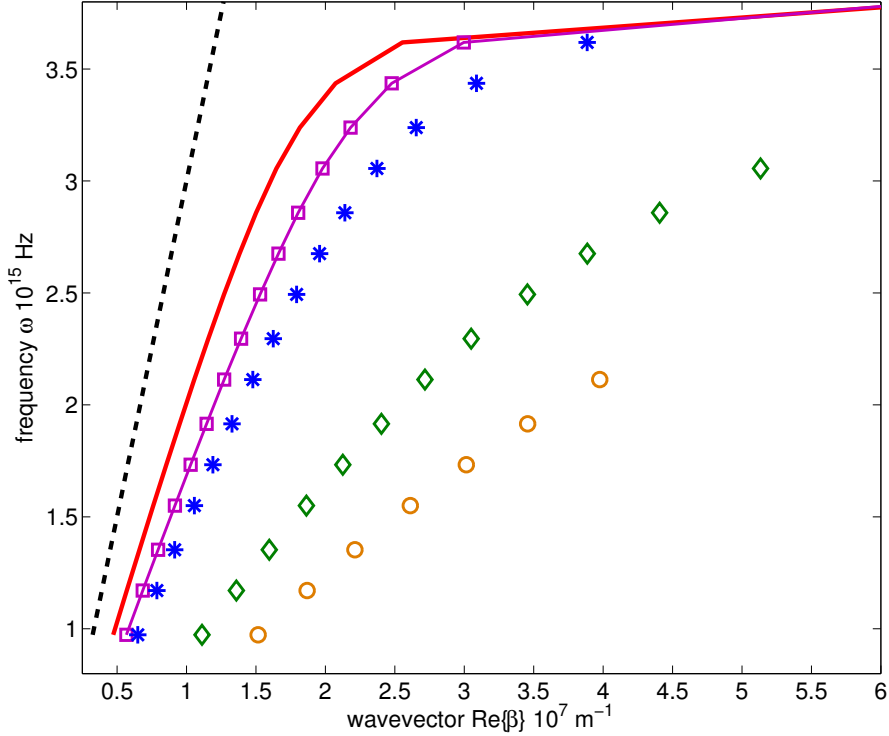
Figure 2-8: Dispersion relation for the symmetric SPP mode supported by the MIM (Au|SiO$_2$|Au) structure for a dielectric thickness of 100nm (squares), 50nm (stars), 10nm (diamonds), 5nm (circles) for low energy modes. Also shown the dispersion at single Au|SiO$_2$ interface (solid line) and the light line (dashed line). As the metal thickness reduces the k_{SP} increases for specified ω. Johnson and Christy data is used for gold. Backbending is not shown in the results.

MIM structures can squeeze the light in the dielectric region, or in other words they can shrink the SPP wavelength [66]. SPP wavelength can be shrunk to ten times smaller values of the free space wavelength which is a property that can lead to miniaturized plasmonic structures for various applications in nano-medicine and cancer therapy [67]. In order to visualize the possibility of very small sized structures with decreasing insulator thicknesses in MIM structures, in Figure 2-9 the SPP wavelengths for $\lambda_0 = 582$nm excitation on Ag|air|Ag structure are given. In the same figure, the losses with respect to the insulator thicknesses can also be found, stressing the increasing propagation losses for smaller insulator thicknesses. Hence, in order to engineer small structures, on the order of $1/20^{th}$ of the excitation wavelength, one needs to contemplate the losses.
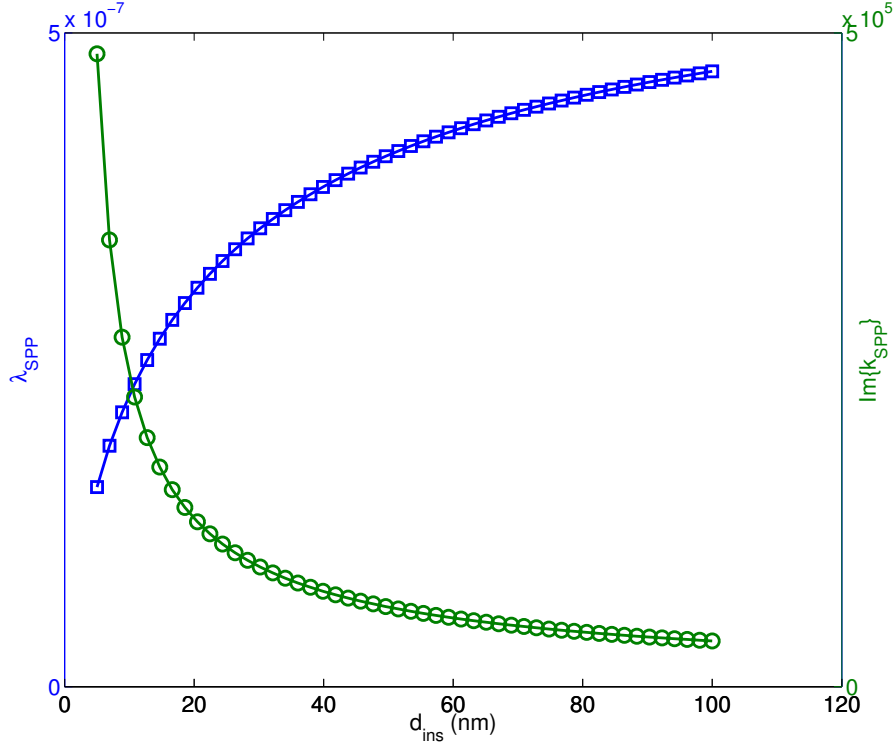
Figure 2-9: The SPP wavelength (squares) and the dispersion losses ($Im\{k_{SPP}\}$) (circles) with respect to the insulator thickness.

The confinement of the SPP mode to the metal film decreases as the mode evolves into a plane wave which for real metals means increased SPP propagation length. Anti-symmetric modes have this behavior and they are called long-ranging SPPs. Symmetric modes confine the metal, so they are short-ranging and due to the increasing attenuation they are slow.

Another symmetric case is the IMI case inspected in Figure 2-10 for the dispersion relation where a splitting into high and low energy modes, i.e., odd and even modes are experienced. The splitting between the energy of odd and even modes increase with the decreasing thickness since the even mode confines more and more whereas odd mode confines less.
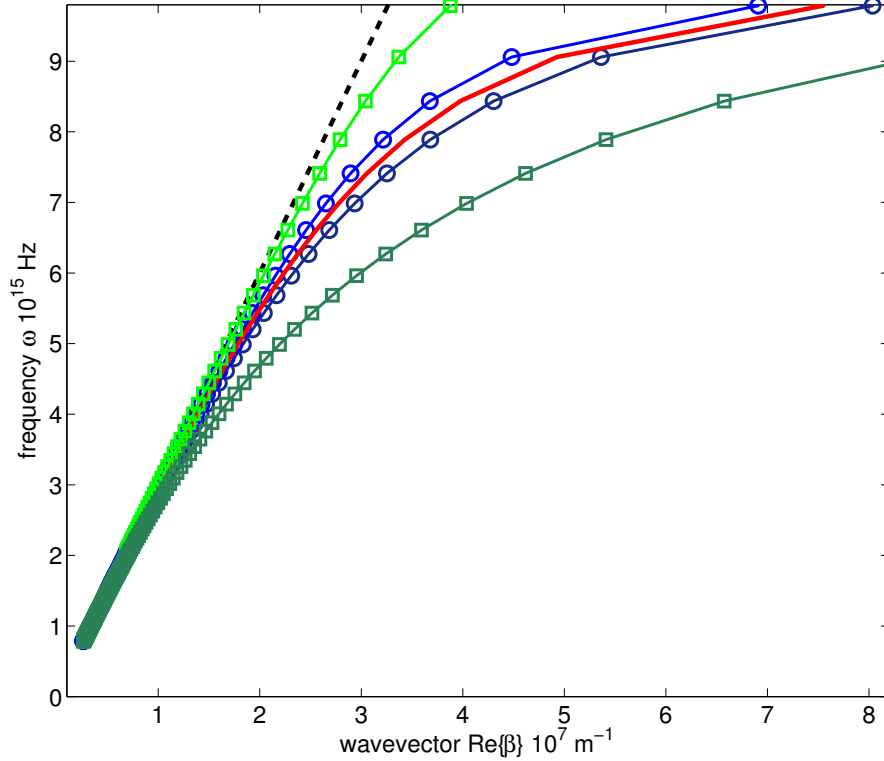
Figure 2-10: Dispersion relation of odd and even modes on air|Ag|air structure. Metal core thicknesses of 50nm (circles) and 20nm (squares). High energy modes are odd, low energy modes are even. Silver is modeled as Drude metal with no loss. Solid line is the single air-Ag interface and dashed line is the light line.

The dispersion relation observed by the electromagnetic theory corresponds to the poles in the expression of the transition radiation, moreover, since the denominators in the transmission radiation and the reflection coefficient expressions are exactly the same; dispersion relation can also be determined from the poles of the reflection coefficient [68] and references therein.

Multiple Interfaces

The eigenmodes of the planar multilayer structure in Figure 2-11 can be found via the vector wave equation under the continuity constraint of the tangential E-field and the normal H-field. Uniqueness of the solutions is guaranteed by the Helmholtz theorem.
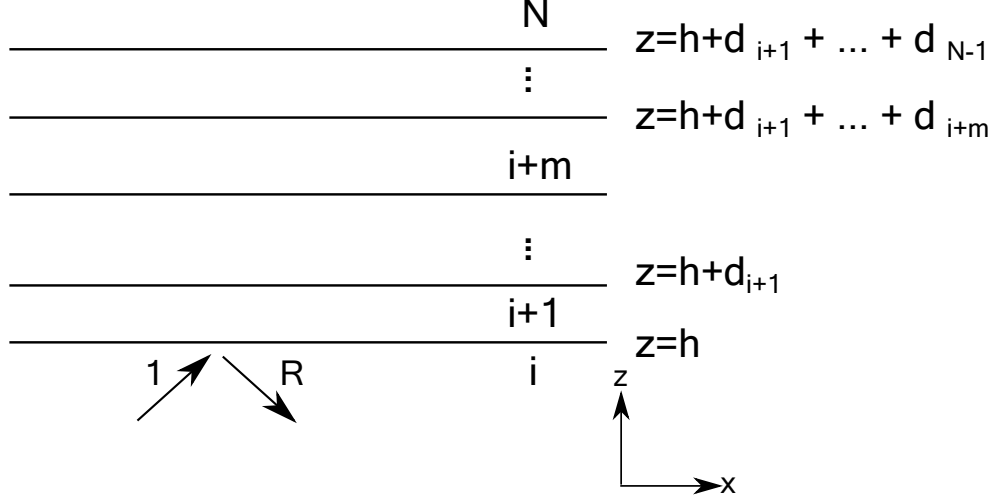
Figure 2-11: Multilayer structure where all supported modes including the SPP mode can be obtained via GRC algorithm.

Various SPP modes can be observed in multiple interface systems since SPPs associated with individual metal-dielectric interfaces may interact with each other.

The poles of the reflection coefficient from a plane wave incidence on a multilayer structure define the SPP resonance locations. An implicit dispersion relation is shown in (2.33) where $\tilde{R}^{i+1,i+2}$ is the Generalized Reflection Coefficient (GRC) for a wave passing from layer $i+2$ to $i+1$. The GRC derivation for multilayer structures can be found elsewhere [69]. Replacing $i=1$ in (2.33) leads to (2.30) which is valid for 3 layer symmetric MIM and IMI structures. GRC root finding algorithm can be applied to geometries to detect SPP wavenumbers in each and all layers [70].

$$R^{i,i+1}\tilde{R}^{i+1,i+2} = e^{jk_{z(i+1)}2d(i+1)} \tag{2.33}$$

The SPP wavenumbers supported in the symmetric MIM structure are observed analytically in Figure 2-12 for different mid-layer thicknesses. As the core thickness reduces in MIM structures a very strong shrinking behaviour is observed. Shrinking the SPP wavelength 10 times smaller than the free space wavelength is possible in these structures, with a simultaneous increase in the loss mechanism given in Figure 2-12. The split into symmetric and antisymmetric modes after certain dielectric thickness

can be seen in the same figure obtained using the GRC root finding algorithm.

The coupling and splitting of the SPP modes into odd and even modes as shown in Figure 2-10 can be further analyzed using the GRC root finding algorithm as the peak of the magnitude of the reflection coefficients refer to the SPP mode locations. In Figure 2-12 the split of the k_{SP} values at specific metal-film thickness is seen.

The dispersion relation for the propagating SPs are observed both analytically and via poles of the reflection coefficient using the GRC root finding algorithm for multilayer structures. The electromagnetic signature of the SPP is identified through the dispersion relation like its propagation and decay lengths.

(a)

(b)

(c)
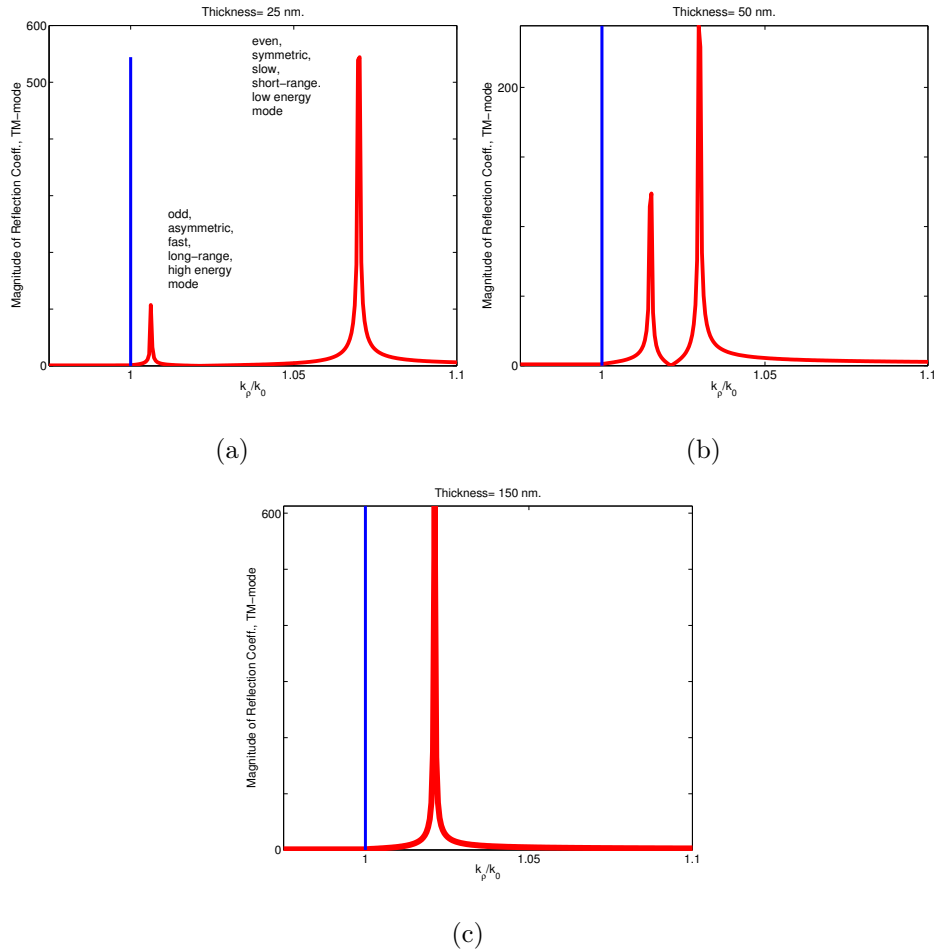
Figure 2-12: The magnitude of the reflection coefficients calculated via GRC root finding algorithm for air|Ag|air multilayer structure with metal film thickness of a) 25nm, a) 50nm, c) 150nm. The splitting of the k_{SP} into high and low energy modes is seen for thin enough films. Solid line shows the excitation wavenumber k_0.

2.2.2 Localized Surface Plasmons

A molecule is strongly excited in the vicinity of a metallic nanoparticle (NP) since the near field is enhanced at the plasmon resonance wavelength of the particle. Non-propagating excitations of the conduction electrons of the metallic NPs coupled to the electromagnetic field result in localized surface plasmon (LSP) [63]. NPs are usually approximated via spheres or spheroids for which analytically exact solutions exist to all orders as carried out by Mie [71]. Due to the curved nature of the NP, LSPs can achieve plasmon resonance by direct illumination without phase matching techniques. Frequency and spectral width of the LSP modes are determined by particle's shape, material, size and environment.

The resonant electromagnetic behavior of noble-metal NPs occurs due to the confinement of the conduction electrons to a small particle volume. For particles with diameter much smaller than the wavelength of the incident light ($a << \lambda$), the quasistatic approximation is valid where the entire structure experiences uniform electric field at any instant of time. Maxwell's equations are solved directly for the scattering of electromagnetic waves, and only the dipolar term is retained in the quasistatic approach whereas higher order modes should be considered for larger particles.

For the particles with diameter $a << \lambda$, the in-phase movement of the conduction electrons upon plane wave excitation leads polarization charges to buildup on the particle surface. These charges act as an effective restoring force and allow resonance to occur at a specific frequency. The resonance builds up a dipolar field outside the particle as well as a resonantly-enhanced field inside the particle, which is homogeneous throughout its volume. This leads to enhanced absorption and scattering cross sections for the electromagnetic waves along with a strongly enhanced near field in the vicinity of the surface of the particle.

In the quasistatic limit, electric fields E_1 inside and E_2 outside of a spherical metallic NP with a dispersive dielectric response ϵ_m and a radius $a << \lambda$ embedded in a nonabsorbing surrounding medium of dielectric constant ϵ_d as shown in Figure 2-13 can be found solving (2.34) under the boundary conditions given in (2.35).
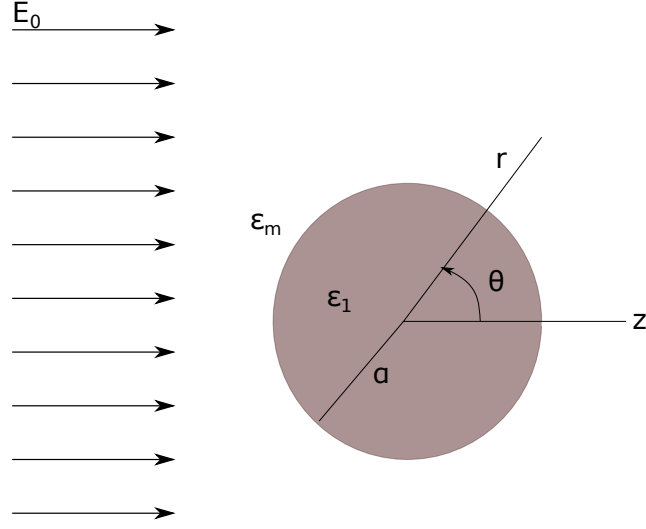
Figure 2-13: Spherical metallic NP in a uniform electric field.

$$E_i = -\nabla \Phi_i \quad \text{where} \quad i = 1, 2. \tag{2.34}$$

$$\Phi_1 = \Phi_2 \quad \text{and} \quad \epsilon_1 \frac{\partial \Phi_1}{\partial r} = \epsilon_m \frac{\partial \Phi_2}{\partial r} \tag{2.35}$$

At large distances from the sphere, the electric field is the unperturbed applied field (2.36) by which the potentials can be obtained as in (2.37a) and (2.37b).

$$\lim_{r \to \infty} \Phi_2 = -E_0 z = -E_0 r \cos \theta. \tag{2.36}$$

$$\Phi_1 = -\frac{3\epsilon_m}{\epsilon_1 + 2\epsilon_m} E_0 r \cos \theta \tag{2.37a}$$

$$\Phi_2 = -E_0 r \cos \theta + a^3 E_0 \frac{\epsilon_1 - \epsilon_m}{\epsilon_1 + 2\epsilon_m} \frac{\cos \theta}{r^2} \tag{2.37b}$$
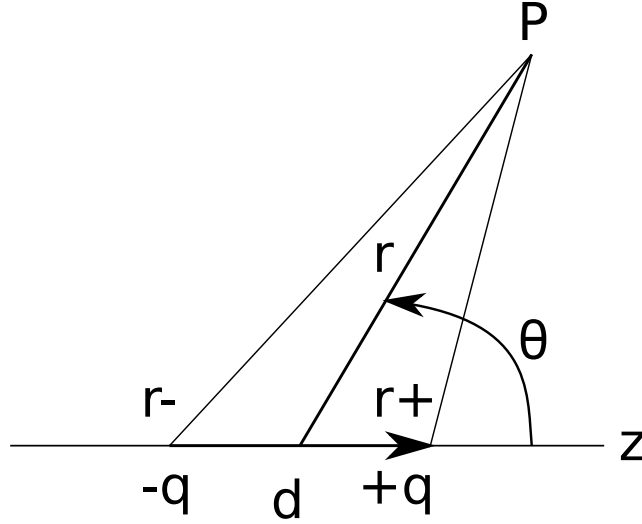
Figure 2-14: Electric dipole approximation for a NP.

A NP in the quasistatic limit can be modeled as a dipole that can be considered as two point charges $+q$ and $-q$ separated by a distance d as given in Figure 2-14.

The potential of the dipole at any point P can be given as in (2.38) where $r_\pm = r\sqrt{1 \pm \frac{\vec{r}\hat{e_z}}{r^2}d + \frac{d^2}{4r^2}}$.

$$\Phi = \frac{q}{4\pi\epsilon_m}\left(\frac{1}{r_+} - \frac{1}{r_-}\right) \tag{2.38}$$

If d approaches zero in such a way that qd product remains constant, the potential of an ideal dipole can be obtained (2.39).

$$\Phi = \frac{\vec{p}\,\vec{r}}{4\phi\epsilon_m r^3} = \frac{p\cos\theta}{4\phi\epsilon_m r^2}. \tag{2.39}$$

In Figure 2-15, the magnitude of the scattered electric field regarding a dipole and a gold sphere of radius $20nm$ are shown at the near field $h = 500$nm above the scatterer whare both the dipole and the gold sphere radiate at $\lambda_0 = 660$nm.
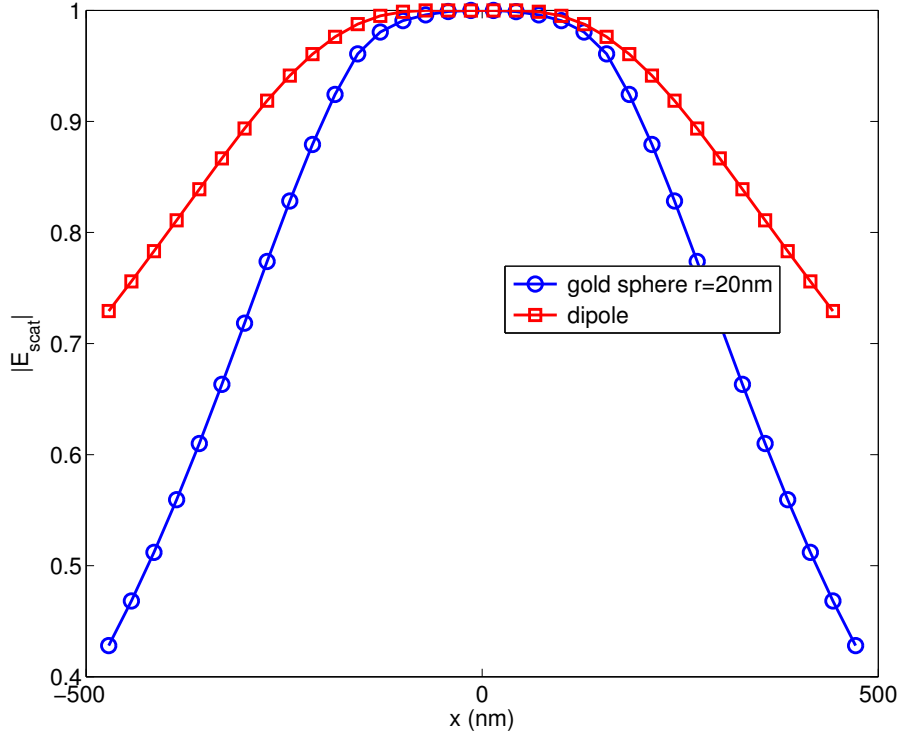
Figure 2-15: Near field scattered electric field from a gold sphere and a dipole. A NP, sphere, is in the quasistatic limit equal to a dipole.

By comparison of the potential outside the sphere (2.37a) to the potential of the dipole (2.39) the applied field is seen to induce a dipole moment proportional to the field (2.40) which can also be expressed as in (2.41) in terms of polarizability α.

$$\overrightarrow{p} = 4\phi\epsilon_m a^3 \frac{\epsilon_1 - \epsilon_m}{\epsilon_1 + 2\epsilon_m} E_0 \tag{2.40}$$

$$\overrightarrow{p} = \epsilon_m \alpha \overrightarrow{E_0} \tag{2.41}$$

The polarizability α of a NP in Figure 2-14 can be derived finally as (2.42).

$$\alpha = 4\phi a^3 \frac{\epsilon_1 - \epsilon_m}{\epsilon_1 + 2\epsilon_m} \tag{2.42}$$

The polarizability and the induced homogeneous polarization inside the particle are resonantly driven at a frequency, Fröhlich frequency, where the denominator shows a minimum as in (2.43) which is limited by the imaginary part of ϵ describing the ohmic heating losses due to the creation of electron-hole pairs.

$$\epsilon_m + 2\epsilon_d \longrightarrow 0 \qquad (2.43)$$

Conclusion

Optical antennas, despite their strong analogy to RF antennas, are crucially different than their RF counterparts mostly due to the nanometer sizes and the physical properties of the metals in the optical regime. The physics of the metal behavior is studied in this chapter by exploring the complex dielectric function, $\epsilon(\omega)$. It is observed that the dispersive nature of the metal, determined by the free electron movements, leads to SPs through collective oscillations of the free electrons in metal with light.

SPs, trapped on a metal-dielectric interface and exhibit collective electron oscillations in metal coupling to the light wave in the dielectric and propagating as a whole, the so called SPPs, are studied in single as well as many metal-dielectric interfaces.

NPs supporting LSPs are by themselves optical antennas, yet they can also be treated as sources for optical antennas where coupling from NP's emission to the SPP creates antenna modes. SPP on metal-dielectric interface is the propagating mode that creates the antenna mode by performing standing waves.

SPPs of an optical wavelength concentrate light in a region that is considerably smaller than their wavelength, a feature that suggests possibility of using SPPs for the fabrication of nanostructures operating at optical frequencies.

In this chapter the fundamental physics behind the dispersive behavior of the metals in optical frequencies are clarified, the SPPs are investigated in single and multi-layer interfaces with odd and even modes due to coupling and lastly, the NPs exhibiting LSPs are examined.

Chapter 3

RF vs. Optical Antennas

The history of antennas dates back to James Clerk Maxwell who is well-known for Maxwell's equations unifying the theory of electricity and magnetism and representing their relations as a set of profound equations. Maxwell also showed that light is an electromagnetic wave and propagates with a particular speed. The first wireless system was demonstrated by Heinrich Rudolph Hertz in 1886, however it was 1901 when Guglielmo Marconi managed to send signals over large distances [3].

During World War II modern antenna technology launched and new elements were primarily introduced. The invention of the microwave sources with frequencies of 1GHz and above was a contributing factor to this new era. The advances in computer architecture and technology during 1960s through 1990s had a major impact on the progress of modern antenna technology. With the introduction of numerical methods like MoM, FDTD and FEM previously intractable complex antenna system configurations were analyzed and designed accurately, contributing significantly to the maturity of the antenna field.

While antennas are a key enabling technology for devices like cellular phones and televisions using electromagnetic radiation in the radiowave and microwave regime, their optical analog is basically nonexistent in today's technology. Once fabrication techniques have been improved to yield geometries with a few nanometers precision, since it was the main reason of the late arrival of optical antennas, and become accessible to researchers in universities and research labs, there has been a flurry of

activities and interests in optical antennas and their applications [15–20,22,23,30,72]. Even so, one would have expected that the maturity of the RF antennas would have had a more pronounced effect in the development of optical antennas.

A strong analogy between optical antennas and their RF counterparts has been observed in terms of the desired operation. The main attraction of RF antennas is their ability to collect radiated electromagnetic energy efficiently into a small volume on the receiver side (Rx), and to provide more directive and efficient radiation of electromagnetic energy into a target volume on the transmitter side (Tx). Likewise, optical antennas enable the control, manipulation and visualization of light on subwavelength structures. (Figure 3-1)
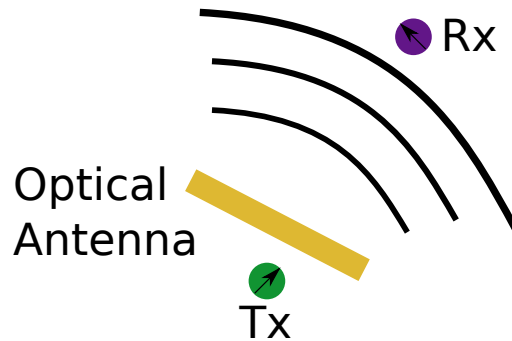
Figure 3-1: Analogy between optical and RF antennas. The information regarding the emitter (Tx) in the vicinity of the optical antenna is radiated directively to the destination (Rx). Since antennas are reciprocal, the opposite way of information transmission is also possible.

Recent research in nanooptics and plasmonics has generated considerable interest in the optical antenna concept and several studies are currently focused on how to translate established radiowave and microwave antenna theories into the optical frequency regime [11, 18, 20]. The robust analogy between the optical and the RF antennas inspires a possible mapping between the two domains.

Though there is a high analogy, there are some important differences between the optical and RF antennas mainly due the metal behavior and the nanoscale dimensions. The main difference relevant to the subject matter of this thesis is the wave-matter interaction at the interface between dielectric and metal, which manifests itself as surface current at RF and SPPs at optical frequencies. Though metals

at RF do not let electromagnetic waves propagate through them, at higher frequencies penetration of the radiation into metal increases, leading to increased dissipation. In the optical regime, the metals become lossy behaving as a free electron gas; and, as we go higher to ultraviolet frequencies they achieve a completely different character acting as a dielectric. While SPPs are highly localized to the dielectric-metal interface and propagate along the interface with the wavelength smaller than the wavelength in the dielectric, the electromagnetic fields due to the surface current in RF extend to the whole dielectric region with the same wavelength as the surrounding dielectric medium. Therefore, for antennas operating at optical wavelengths, the resonance of the structure is fundamentally defined by the SPPs and their interactions with the antenna structure, which introduces a new term, the effective wavelength, λ_{eff} [13].

The feeding mechanism in RF and optical antennas differ since optical antennas cannot be fed via TLs as opposed to their RF counterparts due to the nanoscale dimensions. Optical antennas are rather fed through coupling to the radiation of a nearby emitter. Antenna feeding is one important concept since antenna parameters like radiation, gain, directivity and polarization depend on the feed location due to the excited resonant antenna mode. As stated above, the resonant antenna modes are formed by the SPPs in optics and surface currents in RF.

In this chapter, the differences arising due to the metal behavior in optics will be investigated in terms of the effective wavenumber. Effective wavenumber is a complex quantity which possesses the information of other important variables like the effective wavelength, imperfect reflections and the Q factor. In the second half, the physics of antenna feeding in optics will be discussed.

3.1 Effective Wavenumber

The effective wavenumber is a complex quantity whose real part is related to the effective wavelength as $Re\{k_{eff}\} = \frac{2\pi}{\lambda_{eff}}$ and imaginary part is related to the quality factor (Q) as in (3.1).

$$k_{eff} = \frac{2\pi}{\lambda_{eff}}(1 + i\frac{1}{2Q}) \qquad (3.1)$$

In the second chapter the SPP behavior with its dispersion relation has been studied. Here, the effective wavenumber will be derived with a review on the effective wavelengths, the reflections due to the finite antenna sizes and the Q factor.

3.1.1 Effective Wavelength

RF antennas are at resonance when their characteristic lengths are integer multiples of half of the wavelength of the incoming radiation. However, for antennas operating at optical wavelengths, the resonance of the structure is fundamentally defined by the SPPs and their interactions with the antenna structure, which requires a new definition of the resonant length, rather than half of the wavelength of the illumination as in RF. Optical antennas resonate at sizes fundamentally half of the effective wavelength. The SPPs form the standing waves, creating the resonant antenna modes that will generate the radiation. The resonance condition for an optical antenna of length l can be observed via TL or Fabry-Perot resonator analogy. Assumption here is that the SPP, supported by the antenna, goes through imperfect, complex reflections from the antenna terminations.

The resonance condition for the SPP propagating in the TL of length l shown in Figure 3-2 with characteristic impedance Z_0, load impedance Z_L and imperfect reflection due to mismatched loads $\Gamma = |\Gamma|e^{i\Phi_\Gamma}$ is given in (3.2) due to an in-phase interference of the propagating SPs.

$$e^{ik_{SP}2l}|\Gamma|^2 e^{i2\Phi_\Gamma} = \alpha e^{i2\pi m} \qquad (3.2)$$
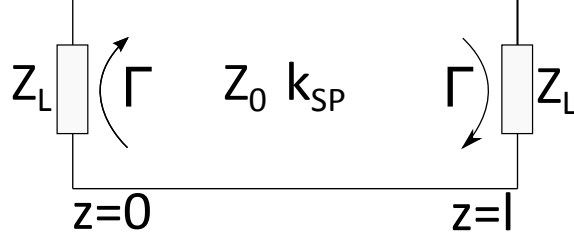
Figure 3-2: TL with length l, characteristic impedance Z_0 where SP propagates and imperfectly reflects from boundaries due to mismatched loads Z_L.

In a passive system, only the magnitude or the phase of (3.2) can be conserved, therefore a phase matching condition, (3.3), related to the resonant antenna length l can be derived from (3.2).

$$Re\{k_{SP}\}l + \Phi_\Gamma = m\pi \tag{3.3}$$

Effective wavelength calculations are available in the literature for various geometries [13,73–75]. The effective wavelength λ_{eff} at which the optical antenna responds to the external excitation is related to the antenna resonant length l as $\lambda_{eff} = m2l$ via TL resonance analogy, that being so the effective wavelength can be represented for the fundamental mode $m = 1$ as in (3.4) in terms of the SP wavenumber and the complex reflection coefficient.

$$\lambda_{eff} = 2\frac{\pi - \Phi_\Gamma}{Re\{k_{SP}\}} = 2l \tag{3.4}$$

The calculation of the complex reflection coefficient is very important to observe the correct antenna resonant lengths, therefore different approaches to the problem are visited here in detail.

3.1.2 Reflection Coefficients

The calculation of the complex reflection coefficients regarding the SPPs propagating on various structures like antennas, waveguides, resonators is important in order to design these structures at their resonant lengths for in-phase interference of the incident and the reflected SPPs. The dielectric waveguide model is proposed for the

guided SPPs via Fresnel reflections by taking the refractive index of the medium as $n_{eff} = k_{SP}/k_0$ [76]. This approach implicitly assumes SPP as a plane wave. The reflections of SPPs propagating on a semi-infinite metal-dielectric interface is further studied in a more accurate vectorial approach [77]. This method assumes that SPP is the dominating field distribution in the region enclosing the metal-dielectric interface. There is an indirect method for metal nano-strips using full-wave simulations based on Finite Difference Frequency Domain (FDFD) method where the reflection coefficient is formalized as the ratio of the incident to reflected electric field measured at a specific location on the nano-strip [75]. An analytical method for the reflections from MIM structures is proposed for lossless and dispersion free metals [74]. This model is improved for real metals with the introduction of the continuity of the poynting flux in the SP propagation direction [73].

Semi-Infinite Structures

The parallel x and y components of the electric and magnetic fields are matched at the boundary as in (3.5)-(3.6) where Γ is the complex reflection coefficient, i refers to incident field, SP refers to SPP field and FS refers to free space field (Figure 3-3).

$$(1 + \Gamma)E_{x,i}^{SP} = E_x^{FS} \qquad (3.5)$$

$$(1 - \Gamma)cos(\theta)H_{y,i}^{SP} = H_y^{FS} \qquad (3.6)$$

Upon Fourier expansion of the magnetic field H_y^{FS} and using the boundary conditions the reflection coefficient Γ can be analytically calculated as (3.7) for the semi-infinite structure in Figure 3-3.
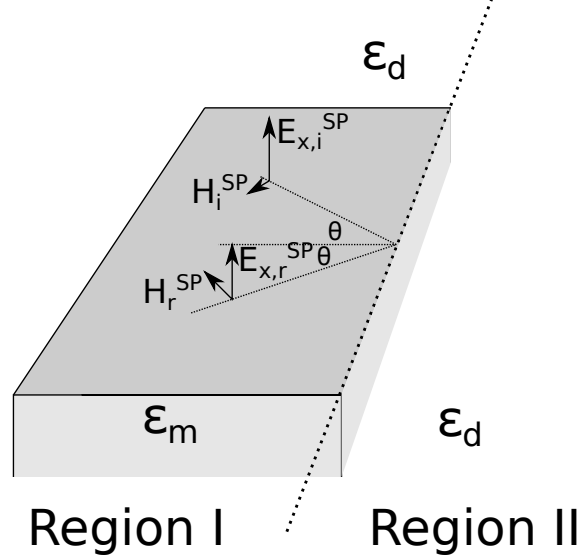
Figure 3-3: Geometry for the SPP reflection at free space boundary on a semi-infinite metal-dielectric interface. Region I is a metal slab with dispersive dielectric constant (ϵ_m) that extends infinitely in $y-$direction and semi-infinitely in $x-$ and $z-$ directions. Region II is the dielectric region with a dielectric constant ϵ_d.

$$\Gamma = \frac{I cos(\theta)\epsilon_p^2(\epsilon_d - \epsilon_m) - \pi\sqrt{-\epsilon_d\epsilon_m}}{I cos(\theta)\epsilon_p^2(\epsilon_d - \epsilon_m) + \pi\sqrt{-\epsilon_d\epsilon_m}} \tag{3.7}$$

The new defined terms ϵ_p and I in (3.7) are expressed in (3.8) where $u_z(u)$ in the integration I is $u_z(u) = \sqrt{\epsilon_d - u^2 - \epsilon_p sin(\theta)^2}$.

$$\epsilon_p = \epsilon_m\epsilon_d/(\epsilon_m + \epsilon_d)$$

$$I = \int_{-\infty}^{\infty} \frac{(\epsilon_d - u^2)du}{u_z(u)(u^2 - \frac{\epsilon_p\epsilon_d}{\epsilon_m})(u^2 - \frac{\epsilon_p\epsilon_m}{\epsilon_d})} \tag{3.8}$$

Upon numerical implementation of the analytically observed representation, the magnitude and phase of the complex reflection coefficient for the SPPs propagating on Silver-air interface excited with $\lambda_0 = 632$nm illumination are shown in Figures 3-4(a), 3-4(b) to be in good agreement with the reference study [77].

(a)   (b)
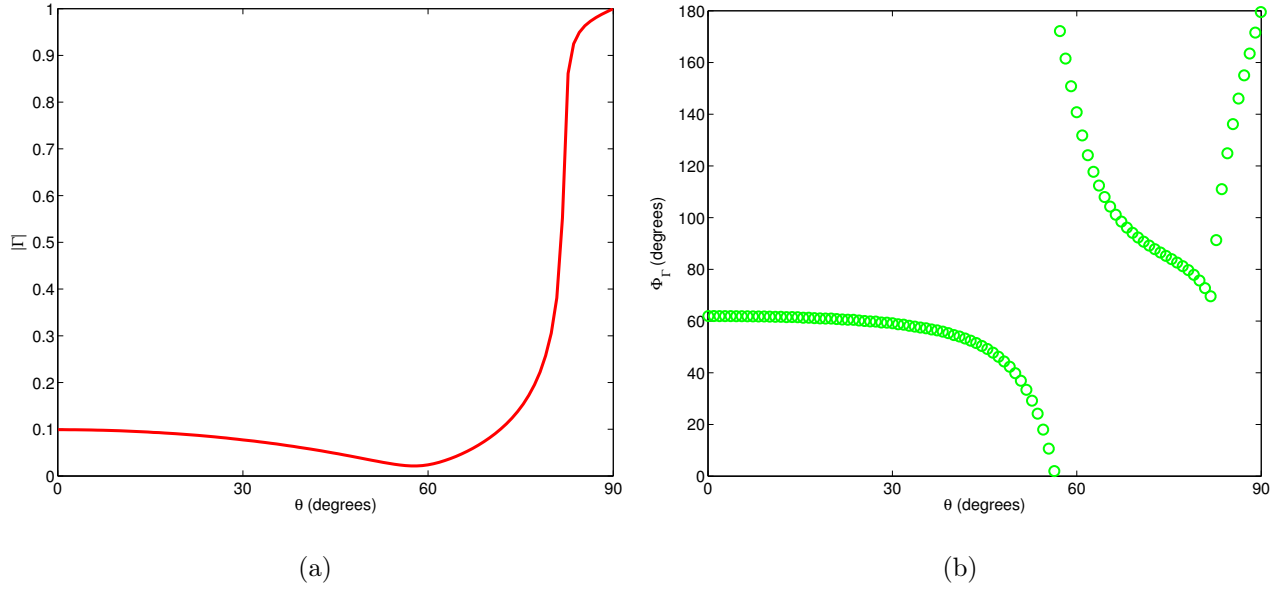
Figure 3-4: Amplitude and phase of the complex reflection coefficient with respect to excitation ($\lambda_0 = 632nm$) angle θ for semi-infinite silver-air structure a) magnitude b)phase.
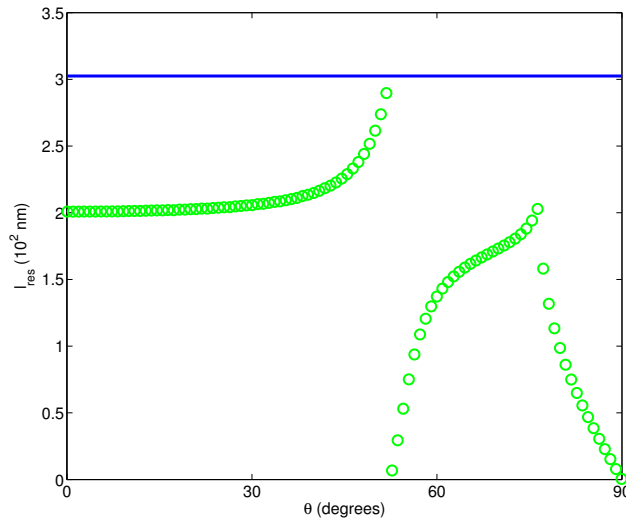
Figure 3-5: Resonant lengths for semi-infinite silver-air structure upon $\lambda_0 = 632nm$ excitation with respect to various illumination angles θ. Solid blue line shows $\lambda_{SP}/2$.

The resonant lengths for the semi-infinite silver-air structure upon $\lambda_0 = 632nm$ excitation with respect to different θ excitation angles in Figure 3-5 with a solid line for the resonant length for SPP, half of the SPP wavelength, is given.

For all the excitation angles the resonant length is smaller than the SPP resonant length due to imperfect reflection losses.

Two-Interface Structures

Consider a 3-layer structure infinite in y direction, discontinuous in z direction and has a boundary to air in x direction, in Figure 3-6, where part of the SPPs supported in the structure can couple to and propagate as free space modes. This structure is first studied for lossless and dispersionless metals [74], later improved for real metals with the introduction of the energy conservation at the boundaries in the SPP propagation direction [73].
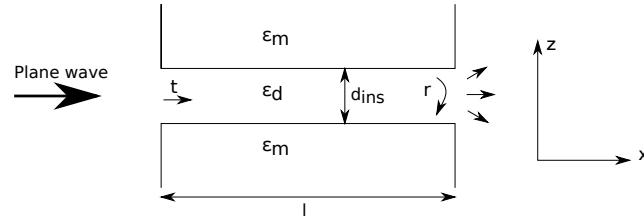
Figure 3-6: Finite length MIM cavity supporting an SPP mode propagation.

In addition to the boundary conditions regarding the continuation of the tangential fields, an intuitive boundary condition for the conservation of the energy of the fields on both sides of the termination are given in (3.9).

$$(1 + \Gamma)E_z^{SP} = E_z^{FS}$$
$$(1 - \Gamma)H_y^{SP} = H_y^{FS}$$
$$\int_{-\infty}^{\infty} S_x^{SP} dz = \int_{-\infty}^{\infty} S_x^{FS} dz \qquad (3.9)$$

The free space energy is derived in (3.10) using the boundary conditions given above.

$$
\begin{aligned}
\int_{-\infty}^{\infty} S_x^{FS} dz &= -\int_{-\infty}^{\infty} E_z^{FS} H_y^{FS*} dz \\
&= -\int_{-\infty}^{\infty} (1+\Gamma) E_z^{SP} (1-\Gamma^*) H_y^{SP*} dz \\
&= -(1+\Gamma)(1-\Gamma^*) \int_{-\infty}^{\infty} E_z^{SP} H_y^{SP*} dz
\end{aligned} \tag{3.10}
$$

The z component of the free space electric field E_z^{FS} can be expressed as a super-position of the plane waves, using the Fourier transform as in (3.11).

$$
E_z^{FS} = \int_{-\infty}^{\infty} f(k_z) e^{ik_z z} dk_z \tag{3.11}
$$

Rearranging (3.11) for $k_z = k_0 u$ leads to (3.12) via the boundary conditions, where $f(k_z) = \frac{1}{2\pi}(1+\Gamma) \int_{-\infty}^{\infty} E_z^{SP} e^{-ik_z z} dz$.

$$
E_z^{FS} = \int_{-\infty}^{\infty} f(k_z) e^{ik_0 uz} k_0 du \tag{3.12}
$$

Transforming from k_z to u space; $f(u)$ is defined as a function of $I_1(u)$ in (3.13).

$$
\begin{aligned}
f(u) &= \frac{1+\Gamma}{2\pi} \int_{-\infty}^{\infty} E_z^{SP} e^{-ik_0 uz} dz \tag{3.13} \\
&= \frac{1+\Gamma}{2\pi} I_1(u) \tag{3.14}
\end{aligned}
$$

The magnetic field can be observed as in (3.15) correspondingly.

$$
H_y^{FS} = \frac{-1}{\omega \mu_0} \int_{-\infty}^{\infty} \frac{(1+\Gamma) I_1(u)}{2\pi} \frac{k_0^2 e^{ik_z z}}{\sqrt{k_0^2 - k_z^2}} dk_z \tag{3.15}
$$

The free space energy can be derived as in (3.16).

$$\int_{-\infty}^{\infty} S_x^{FS} dz = -\int_{-\infty}^{\infty} E_z^{FS} H_y^{FS*} dz$$

$$= -\int_{-\infty}^{\infty} (1+\Gamma) E_z^{SP} (1-\Gamma^*) H_y^{SP*} dz$$

$$= -(1+\Gamma)(1-\Gamma^*) \int_{-\infty}^{\infty} E_z^{SP} H_y^{SP*} dz$$

$$= -(1+\Gamma)(1-\Gamma^*) \int_{-\infty}^{\infty} E_z^{SP} \frac{-1}{\omega\mu_0} \int_{-\infty}^{\infty} \frac{(1+\Gamma^*)I_1^*(u)}{2\pi} \frac{k_0^2 e^{-ik_z^* z}}{\sqrt{k_0^2 k_z^{*2}}} dk_z dz$$

$$= -(1+\Gamma)(1+\Gamma^*) \frac{-1}{2\pi\omega\mu_0} \int_{-\infty}^{\infty} \frac{|I_1|^2 k_0^2}{\sqrt{k_0^2 - kz^{*2}}} dk_z \tag{3.16}$$

The reflection coefficient Γ is observed in (3.17) via matching the free space and SPP energies through (3.10) and (3.16).

$$\frac{1-\Gamma^*}{1+\Gamma^*} = \frac{\int_{-\infty}^{\infty} du \frac{-|I_1(u)^2|}{\sqrt{1-u^2}}}{\lambda_0 \sqrt{\frac{\mu_0}{\epsilon_0}} \int_{-\infty}^{\infty} dz E_z^{SP} H_y^{SP*}} \tag{3.17}$$

The original study [74] for lossless and dispersionless metal and without the energy conservation on the boundary, by using the rest of the boundary conditions above calculates the reflection coefficient as in (3.18) for a G defined in (3.19) .

$$\Gamma = \frac{1-G}{1+G} \tag{3.18}$$

$$G = \frac{1}{2\pi} \frac{\int_{-\infty}^{\infty} \frac{k_0}{Z_0 \sqrt{k_0^2 - k_x^2}} [F.T\{E_z^{SP}\}]^2 dkz}{\int_{-\infty}^{\infty} E_z^{SP} H_y^{SP*} dz} \tag{3.19}$$

The magnitude and phase of the complex reflection coefficient with respect to incident wavelength for various insulator thicknesses $d_{ins} = 20$nm, 50nm, 100nm are given in Figure 3-7 for Ag-air-Ag structure.
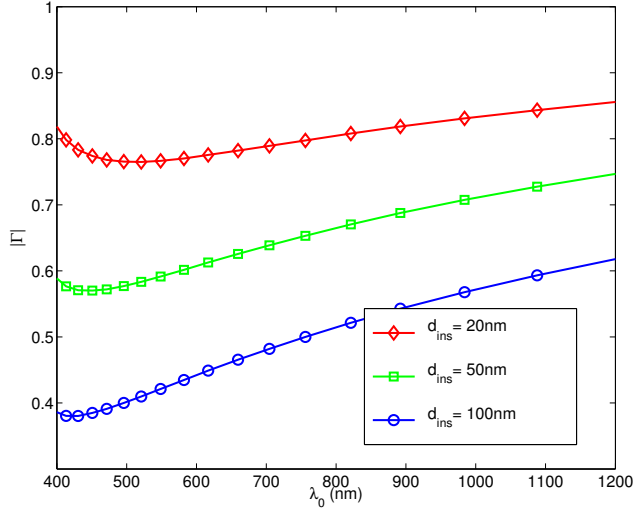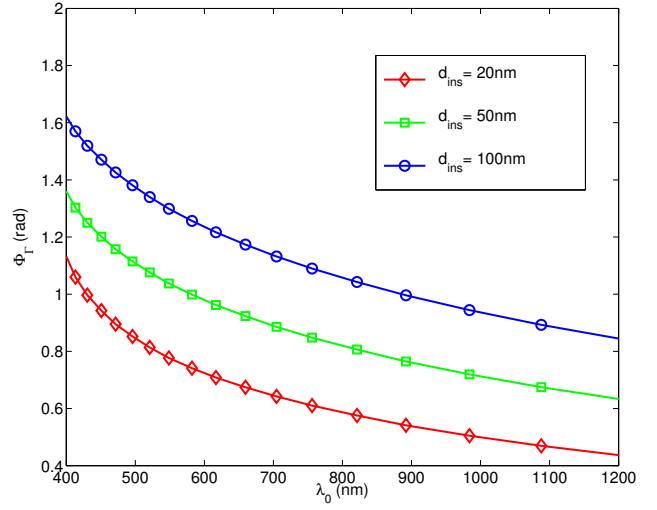
Figure 3-7: Reflection coefficient amplitude and phase with respect to incident wavelength on Ag-air-Ag MIM structure a)amplitude of the reflection coefficient b)phase of the reflection coefficient. Results observed from analytical derivations and implemented in Matlab.
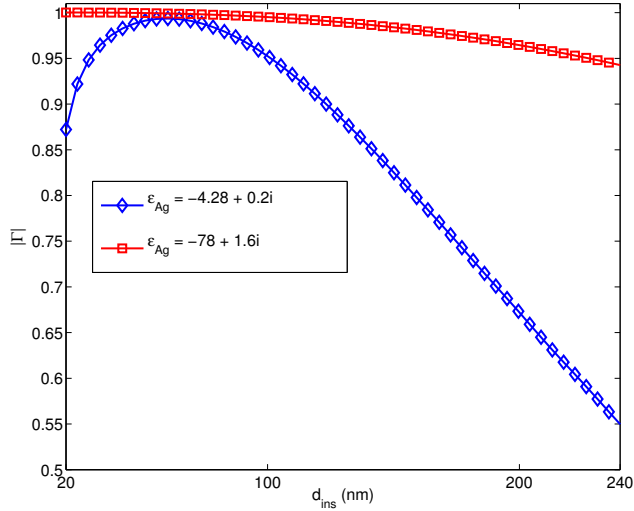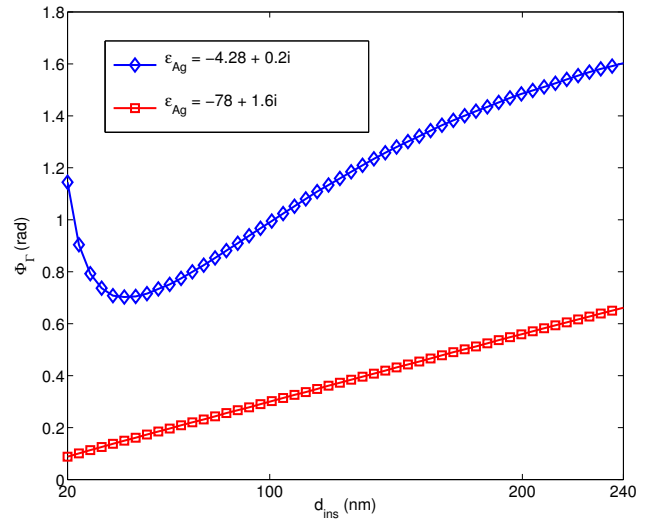
Figure 3-8: Reflection coefficient amplitude and phase with respect to the insulator thickness on Ag-air-Ag MIM structure a)amplitude of the reflection coefficient b)phase of the reflection coefficient. Results observed from analytical derivations and implemented in Matlab.

The magnitude and phase of the complex reflection coefficient for various incidences $\lambda_0 = 397$nm, 1216nm are given in Figure 3-8 for Ag-air-Ag structure as a function of insulator thickness.

The resonant lengths, mainly the effective wavelengths, are calculated using the TL resonance condition. In Figure 3-9 the resonant lengths regarding the Ag-air-Ag structure under an illumination of $\lambda_0 = 892$nm are shown as a parameter of the insulator thickness. The dispersive, real silver is considered with continuation of the energy at the boundary [73].
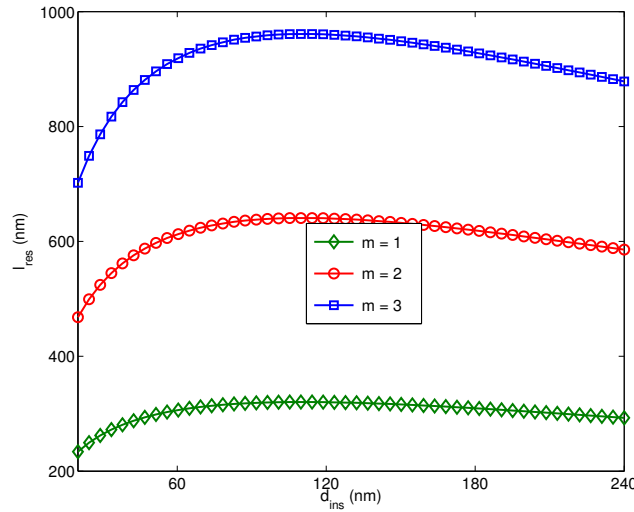
Figure 3-9: Resonance lenghts as a function of insulator thickness for different orders under $\lambda_0 = 892$nm excitation on Ag-air-Ag MIM structure

The SPP dispersion and propagation on symmetric two-interface structures like MIM and IMI were given in a similar manner in Chapter 2. The nature of physical behavior and the mathematical derivations inspires calculation of the SPP reflection coefficient on IMI structures by using the same method introduced above.

In the literature, the SP reflection on an IMI structure (Figure 3-10), representing a nano-strip antenna, has been examined using full-wave simulations based on FDFD method [75] where the reflection coefficient is expressed as the ratio of the incident to reflected electric field measured at a location x_m.
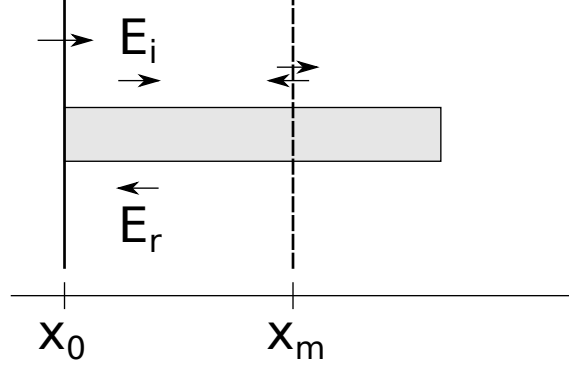
Figure 3-10: IMI structure with launch point x_0, end-face x_e and the measurement point x_m

In order to solve the IMI problem analytically, the MIM algorithm given above for dispersive, real metals [73] is implemented for IMI in Figure 3-11 considering a silver film of various thicknesses for three different excitation wavelengths $\lambda_0 = 500$nm, 600nm, 700nm.

(a)   (b)
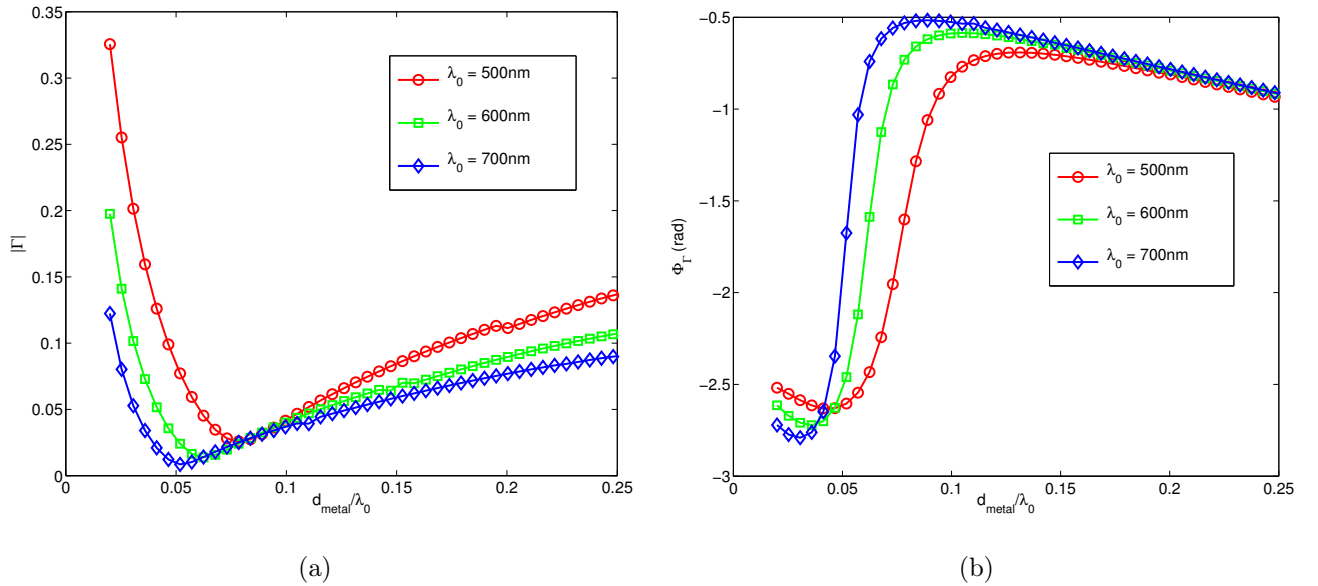
Figure 3-11: Reflection coefficient amplitude and phase with respect to the thickness of the metal layer in air-Ag-air IMI structures upon three different excitations $\lambda_0 = 500$nm, 600nm, 700nm calculated by the analytical approach introduced for MIM structures. a)amplitude of the reflection coefficient b)phase of the reflection coefficient.

The observation of the complex reflection coefficients for IMI structures through the analytical method introduced here for MIM structures is proven to be valid when

compared to the FDFD results in [75]. In the optical antenna design chapter this will be more clear as we will be running a test for the antenna resonant lengths, since the accuracy of the complex reflection coefficients are very important in the resonant length calculation.

3.1.3   Quality Factor

For an ideal lossless case, the response of an antenna to external excitation is a discrete set of infinitely narrow peaks, one for each eigenfrequency. Q factor is a figure of merit in antenna design that is related to the spectral energy density associated to the resonant mode and the electric field enhancement on resonance and it is a function of the antenna's size, shape and the surrounding environment. Q factor is defined as the product of the angular frequency and the ratio of time averaged energy stored to the power loss per second as given in (3.20).

$$Q = \omega_0 \frac{\text{Stored energy}}{\text{Power loss}} = \omega_0 \frac{U}{P} \tag{3.20}$$

In the frequency domain, the antenna modes are defined by considering analytical continuations of the Maxwell's equations in the complex frequency plane, with eigenmodes $(\mathbf{E}, \mathbf{H}, \tilde{\omega})$ where $k_{eff} = \tilde{\omega}\sqrt{\epsilon\mu}$. For real ϵ and μ, $(\mathbf{E^*}, -\mathbf{H^*}, \tilde{\omega}^*)$ is also a solution of the Maxwell's equations. Applying the Green-Ostrogradski formula to the vector $\mathbf{E} \times \mathbf{H^*} + \mathbf{E^*} \times \mathbf{H}$ on an arbitrarily closed surface, $\sum$ defining a volume V, (3.21) can be observed.

$$\iint_{\Sigma} (\mathbf{E} \times \mathbf{H^*} + \mathbf{E^*} \times \mathbf{H}) \cdot d\mathbf{S} = i(\tilde{\omega} - \tilde{\omega}^*) \iiint_V (\epsilon|\mathbf{E}|^2 + \mu|\mathbf{H}|^2)dV \tag{3.21}$$

Introducing the time averaged real power through the closed surface $\sum$

$$P = 1/2 \iint_{\Sigma} Re\{\mathbf{E} \times \mathbf{H^*}\}d\mathbf{S}$$

and time-averaged electromagnetic energy stored in the volume V,

$$U = 1/4 \iiint_V (\epsilon|\mathbf{E}|^2 + \mu\mathbf{H}^2)dV$$

equation (3.21) can be reorganized as $P = 2Im\{\tilde{\omega}\}U$ where U and P are defined for the eigenmode. From (3.20) one can interpret (3.22).

$$Q = \frac{Re\{\tilde{\omega}\}}{2Im\{\tilde{\omega}\}} \tag{3.22}$$

In the time domain picture, the energy stored in the cavity is exponentially decaying in time with a decay constant τ as $U = U_0 e^{-t/\tau}$. Radiated power P can be found from derivation of U with respect to time as $P = -1/\tau U_0 e^{-t/\tau}$. Decay constant is defined as $\tau = Q/\omega_0$, as a result Q factor is a measure of the resonant mode lifetime.

Both frequency and time domain pictures are completely equivalent. Therefore, a damped oscillation with a real frequency ω_0 and time decay $\tau = Q/\omega_0$ is equivalent to a lossless oscillation at a complex resonance frequency $\tilde{\omega} = \omega_0 + i\omega_0/2Q$.

Another approach is via the circuit analysis. The general topology of the equivalent circuit of an antenna, given in Figure 3-12 for TM_{mn} modes, can be built with series connections of parallel resonant sections for each eigenfrequency which for the special case of the (m, n) mode excitation can be given as in Figure 3-13 with L' indicating the negligible contribution of all higher order modes.
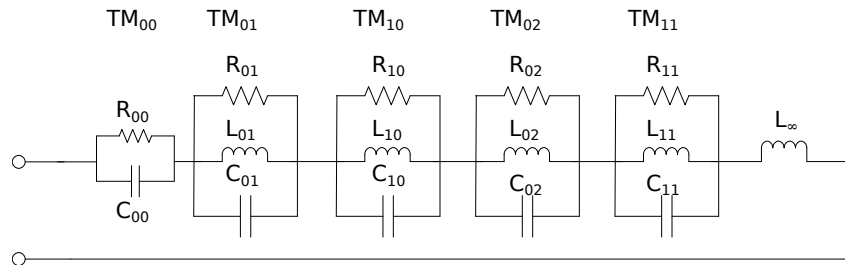
Figure 3-12: The equivalent circuit of the RF patch antenna. Q factor definition through circuit equivalent of an RF patch antenna.
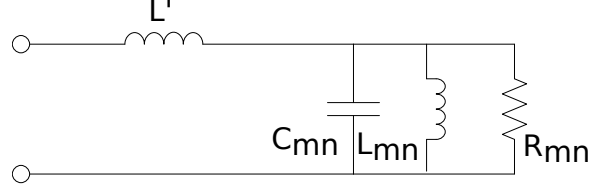
Figure 3-13: The circuit model for patch antenna operating at its (m, n) mode band where L' corresponds to the (negligible) higher order modes' contribution.

Q factor is a measure of loss of a resonant circuit and it increases as loss decreases. Q factor for circuits can be derived as in (3.23) starting from (3.20) where the power loss (P_{loss}) and the time averaged energy stored in the capacitor (W_e) and the inductor (W_m) are defined in (3.24) for the RLC circuit shown in Figure 3-13.

$$Q = \omega \frac{W_m + W_e}{P_{loss}} \tag{3.23}$$

$$
\begin{aligned}
P_{loss} &= \frac{|I_R|^2 R}{2} \\
W_e &= \frac{|I_C|^2}{4C} \\
W_m &= \frac{|I_L|^2 L}{4}
\end{aligned}
\tag{3.24}
$$

Considering the resonance of the circuit in Figure 3-13, the antenna behavior can be examined for Q factor, input impedance and the resonance frequency. The input impedance of the RLC circuit can be derived as $Z_{in} = (\frac{1}{R} + \frac{i}{\omega L} - i\omega C)^{-1}$. At resonance due to $W_m = W_e$, the resonance frequency is found as $\omega_0 = 1/\sqrt{LC}$. Q factor at resonance can then be observed as $Q = R/\omega_0 L = \omega_0 RC$ which implies that as losses decrease (R increase) Q increases.

Since Q factor is related to the inverse of the bandwidth, these quantities can be examined for their near resonance behavior through reformalized input impedance relation, $Z_{in} = (\frac{1}{R} - i\omega C(1 - \omega_0^2/\omega^2))^{-1}$. Near resonance, $\omega^2 - \omega_0^2 \approx 2\omega\Delta\omega$, hence input impedance can be derived as $Z_{in} = j\omega C[\omega - \omega_0(1 + i\frac{1}{2Q})]$ from where a complex

angular frequency can be defined as in (3.25).

$$\tilde{\omega} = \omega_0(1 + i\frac{1}{2Q})$$ (3.25)

Examination of the Q factor through frequency and time domain pictures and the circuit equivalent of a resonator (antenna, cavity) proved that a complex angular frequency, hence an effective wavenumber, can be defined using Q factor of the resonator.

Derivation of the Q Factor

Q factor can be derived through the transmitted irradiance which will be maximized at resonance. A parallel plate under an illumination of a narrow beam can be analyzed for reflectance and transmittance irradiation [78].
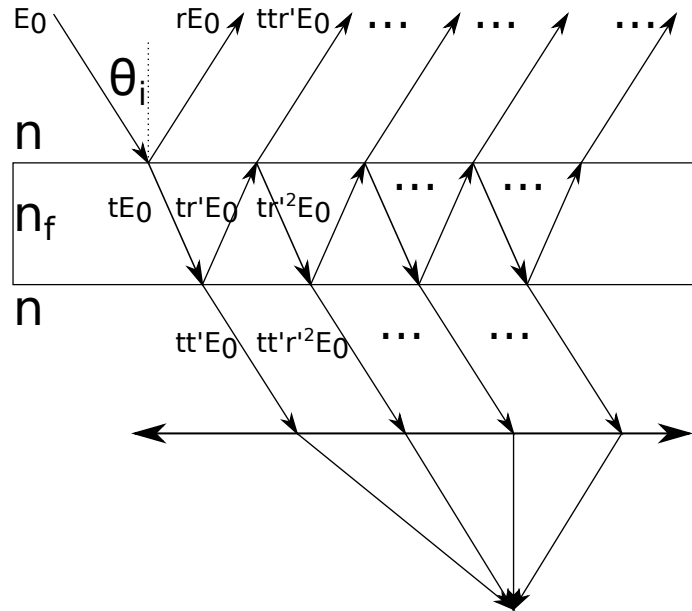
Figure 3-14: Multiply reflected and transmitted beams in a parallel plate

The parallel plate in Figure 3-14 is illuminated with a plane wave with amplitude E_0 and angle of incidence θ_i where the phase difference between successive transmitted beams is $\delta = k\nabla$, $\nabla = 2n_f t cos\theta_t$ and r and t refer to external r' and t' refer to internal reflection and transmission coefficient amplitudes [78]. The successive terms in the transmission area are as follows :

$$E_1 \qquad = tt'E_0$$

$$E_2 \qquad = tt'r'^2 E_0 e^{-i\delta}$$

$$E_3 \qquad = tt'r'^4 E_0 e^{-i2\delta}$$

$$E_4 \qquad = tt'r'^6 E_0 e^{-i3\delta}$$

$$...$$

$$E_N \quad = tt'r'^{(2N-2)} E_0 e^{-i(N-1)\delta} \tag{3.26}$$

The total transmitted field E_T is a superposition of all N modes collected by the converging lens below and is given in (3.27) which can be further organized to obtain (3.28).

$$E_T = \sum_{N=1}^{\infty} E_N = tt'E_0 + \sum_{N=2}^{\infty} tt'r'^{(2N-2)} E_0 e^{-i(N-1)\delta} \tag{3.27}$$

$$E_T = E_0[tt' + tt'r'^2 e^{-i\delta} \sum_{N=2}^{\infty} r'^{(2N-4)} e^{-i(N-2)\delta)}] \tag{3.28}$$

Factoring $x = r'^2 e^{-i\delta}$ in form of geometric series, due to $|x| < 1$ (3.28) can be expressed as in (3.29).

$$E_T = E_0[tt' + \frac{tt'r'^2 e^{-i\delta}}{1 - r'^2 e^{-i\delta}}] \tag{3.29}$$

The relations $tt' = 1 - r^2$ and $r = -r'$ being used in 3.29 results in a much simpler version of E_T in (3.30) from which the intensity can be obtained as $|E_T|^2$ as in (3.31) and normalized as (3.32).

$$E_T = E_0 \frac{1 - r^2}{1 - r^2 e^{-i\delta}} \tag{3.30}$$

$$|E_T|^2 = |E_0|^2 \frac{(1 - r^2)^2}{1 + r^4 - 2r^2 cos\delta} \tag{3.31}$$

$$I_T = \frac{(1 - r^2)^2}{1 + r^4 - 2r^2 cos\delta} I_i \qquad (3.32)$$

Using the trigonometric identity $cos\delta = 1 - 2sin^2(\frac{\delta}{2})$, (3.32) can be simplified and the Airy function (transmittance) can be observed as in (3.33).

$$T = \frac{I_T}{I_i} = \frac{1}{1 + [4r^2/(1 - r^2)^2]sin^2(\delta/2)} \qquad (3.33)$$

Transmittance T will be maximum at resonance, hence its denominator will approach to 0 in the limit. Upon placing the reflection intensity $|r|^2 = R$ in the Airy function the denominator can then be expressed as (3.34) for a resonance at λ_0 with a beamwidth of $\Delta\lambda$ where phase difference δ is represented as a function of wavelength as $\delta = \frac{4\pi n L_c}{\lambda}\phi_r$.

$$\frac{(1 - R)^2}{4R} = sin^2 \frac{\delta(\lambda_0 + 1/2\Delta\lambda)}{2} \qquad (3.34)$$

The value of the total phase delay of the parallel plate δ at resonance can be replaced into (3.34). From the resonance condition, introduced also in (3.3), $\delta = m2\pi = 2k_{SP}l + 2\phi_r$, (3.35) is derived where k_{SP}^r is the real, propagating part of the SPP mode.

$$\frac{(1 - R)^2}{4R} = sin^2\{k_{SP}^r l + \phi_r\} \qquad (3.35)$$

By defining n_{SP} as $k_{SP} = k_0 n_{SP} + i\alpha/2$ and introducing it to (3.35), one can extract (3.36) which can be expressed as Taylor series around zero, the first term of which is the first order derivative that leads to (3.37).

$$\frac{(1 - R)^2}{4R} = sin^2\{\frac{2\pi l}{\lambda_0 + \frac{1}{2}\Delta\lambda} n_{SP}(\lambda_0 + \frac{1}{2}\Delta\lambda) + \phi_r(\lambda_0 + \frac{1}{2}\Delta\lambda)\} \qquad (3.36)$$

$$\frac{(1 - R)^2}{4R} = sin^2\{\frac{2\pi n_{SP}l}{\lambda_0}[1 - \frac{1}{2}\frac{\Delta\lambda_0}{\lambda_0}][1 + \frac{1}{2}\frac{\Delta\lambda}{n_{SP}}(\frac{\partial n_{SP}}{\partial\lambda})_{\lambda_0}] + \Phi_r(\lambda_0) + \frac{1}{2}\Delta\lambda(\frac{\partial\Phi_r}{\partial\lambda})_{\lambda_0}\}$$
$$(3.37)$$

Reorganizing the terms in (3.37) and having a separate paranthesis for $Q = \lambda/\Delta\lambda$ (3.38) can be obtained.

$$\frac{(1-R)^2}{4R} = sin^2\{\frac{2\pi n_{SP}l}{\lambda_0} + \phi_r(\lambda_0) + \frac{\Delta\lambda}{\lambda_0}[\pi l(\frac{\partial n_{SP}}{\partial\lambda})_{\lambda_0} - \frac{\pi n_{SP}l}{\lambda_0} + \frac{\lambda_0}{2}(\frac{\partial\phi_r}{\partial\lambda})_{\lambda_0}]\} \quad (3.38)$$

Since at resonance the term $\frac{2\pi n_{SP}l}{\lambda_0} + \phi_r(\lambda_0)$ will be $2\pi m$, (3.38) reduces down to (3.39) at resonance.

$$\frac{(1-R)^2}{4R} = sin^2(\frac{\Delta\lambda}{\lambda_0}[\pi l(\frac{\partial n_{SP}}{\partial\lambda})_{\lambda_0} - \frac{\pi n_{SP}l}{\lambda_0} + \frac{\lambda_0}{2}(\frac{\partial\phi_r}{\partial\lambda})_{\lambda_0}]) \quad (3.39)$$

The small angle approximation $sin(\theta) \approx \theta$ results in Q as in (3.40).

$$Q = \frac{\sqrt{R}}{1-R}[\frac{2\pi}{\lambda_0}n_{SP}l - \lambda_0(\frac{\partial\phi_r}{\partial\lambda})_{\lambda_0} - 2\pi l(\frac{\partial n_{SP}}{\partial\lambda})_{\lambda_0}] \quad (3.40)$$

By defining a group index $n_g = n_{SP} - \lambda_0(\frac{\partial n_{SP}}{\partial\lambda})_{\lambda_0}$, an effective length $l_{eff} = l - \frac{\lambda_0^2}{2\pi n_g}(\frac{\partial\phi_r}{\partial\lambda})_{\lambda_0}$ and a round-trip effective loss via imperfect reflection r as $R_{eff} = |r|^2 e^{-\alpha l}$, (3.41) can be obtained [79].

$$Q = \frac{\sqrt{R_{eff}}}{1-R_{eff}}[k_0 n_g l_{eff}] \quad (3.41)$$

For narrow resonances and by neglecting the wavelength dependence of the magnitude of the reflection coefficient, r, a Q factor given in (3.42) can be obtained. Generally the penetration length L_p in $l_{eff} = l + 2L_p$ is less than 10% of the length.

$$Q = \frac{k_0}{1-R_{eff}}n_g l \quad (3.42)$$

3.2   Excitation of the Antenna

The optical antennas, due to their nanometer sizes, cannot be fed by TLs. Feeding of the antenna is important in order to generate the desired modes, hence antennas need to be fed from a precise feed location. In optics, feeding is via coupling of the

radiation from a scatterer in the vicinity. Such a coupling shows some interesting physics of the fluorescence enhancement and quenching.

We can consider fluorescence enhancement as a function of plasmon energy and NP scattering efficiency though we cannot examine each characteristic independently. There is a clear correlation between the plasmon resonance wavelength and the maximum radiative rate enhancement such that the radiative rate enhancement is maximal when the plasmon resonance is tuned to the emission wavelength of the molecule. NP scattering is highly dependent on the plasmon excitation since the NP scattering cross section on resonance is strongly enhanced compared to its off resonance value. NP scattering is optimal when the plasmon resonance corresponds to the molecule's emission wavelength as well.

Fluorescence is the product of two processes: i) Excitation by the incident field influenced by the local environment, and ii) emission of radiation influenced by the balance of radiative and nonradiative decay. While the source of process i) is the external radiation field, in process ii) it is the molecule itself which constitutes the source [72].

The intensity of the light in the near field of the NP is enhanced strongly at the plasmon resonance frequency. Hence, at a distance of a few nanometers from the NP the fluorescent of the molecule can be strongly enhanced. Metallic NPs alter the quantum yield of the molecule by modifying the molecular radiative decay rate and so influencing the molecular emission. The coupling efficiency of the fluorescence emission to far field can be increased through NP scattering.

Metallic NPs can be utilized in several ways by controlling the molecule-NP separation, size and geometry of the NP in order to achieve fluorescence enhancement and influence emission [80].

Upon understanding the dependence of the fluorescence enhancement on the plasmon energy and the NP scattering efficiency we can design strategies for the optimization of the enhancement using adjacent metallic nanostructures. The fluorescence enhancement can be changed by tuning the plasmon resonance since the plasmon resonance influences both the radiative rate enhancement and the NP scattering ef-

ficiency [80]. Any internal or external mechanism tuning the plasmon resonance influences fluorescence enhancement.

Optical antennas have strong influence on the excitation and emission of a single molecule. Metallic NPs behave as an elementary resonant dipole antenna given a dipolar radiation pattern and a well defined resonance spectrum as the quasistatic limit of Mie theory describes the scattering properties and the plasmon spectra of the NPs. An excited molecule in the vicinity of an optical antenna behaves like a transmitter, and similarly a molecule in its ground state excited by the localized field near the optical antenna acts as a receiver. So an optical antenna used to enhance the molecular fluorescence acts as a two way antenna [72]. Coupling of light to dipolar radiators lies at the heart of light-matter interaction, furthermore it opens the way to imaging of nano-objects with nonclassical light.

Conclusion

The strong analogy between optical antennas and their RF counterparts inspires a mapping between these domains. In order to bridge the gap between RF and optics which is due to the metal behavior and the scaling, a method for the accurate calculations of the resonant lengths for the optical antennas are examined here, so that the SPPs can generate the standing waves upon reflections from the antenna terminations. Also, for a powerful mapping of the cavity model, the intrinsic wavenumber, at which the optical antenna resonates, is obtained. Due to their nanometer sizes, optical antennas can no longer be fed by TLs, but instead they are excited via coupling to the emission from nearby scatterers. In this chapter the coupling mechanism with a slight touch on the fluorescence enhancement is explored, and a feed mechanism through coupling to a NP emitter in the vicinity of the antenna is proposed.

Chapter 4

Optical Patch Antenna Design

RF antennas have been proposed, optimized and designed for various applications with lots of different configurations since the late 19th century. In the past, antenna design has been considered as a secondary issue in overall system design, yet today it is truly an engineering art and plays a critical role since many systems rely on the design and performance of the antenna [3]. Optical antennas have arrived in the 21st century thanks to the nano-scale fabrication capabilities. Although there is a wealth of knowledge and experience on the design of RF antennas with a potential to be mapped to optics, optical antennas have mainly utilized the RF antenna geometries only. Since optical antennas have recently become quite popular in the scientific community, due to their potential applications in the fields of nanotechnology, biology, biomedical research and nanophotonics, it would be interesting to study the traditional antenna concepts in the realm of optical frequencies.

Although the introduction of the full-wave approaches like MoM, FDTD, FEM and FDFD contributed significantly to the maturity of the antenna field with the ability to analyze and design previously incontrollable complex antenna systems, they are incapable of providing any intuition to the antenna engineers and they create computational complexity due to large number of discretization of the solution domain. In addition to full-wave methods there are a number of antenna systems that can be analyzed with closed form solutions of a boundary value problem. Patch antennas are one of these structures for which analytical and semi analytical models and design

techniques are available.

Inspired by this assessment, the transfer of accumulated knowledge in one of the most widely employed and versatile antenna configurations in RF, the patch antennas, to the optical frequencies, with special emphasis given to their modeling and the computational aspect will be presented in this chapter. Cavity model will be introduced for patch antennas in order to provide an understanding of the operating principles, determination of performance limitations and development of new antenna configurations. As such, this thesis intends to open up a new gateway full of new design approaches, functionalities and intuitions in optical antennas. In the first part of this chapter, the RF patch antennas and their modeling techniques will be introduced. Considering the differences between RF and optical properties, given in the third chapter, a mapping of the cavity model will be proposed with optical feeding analogs and appropriate resonant lengths. Lastly, antenna mode excitations and the corresponding radiation patterns obtained both analytically using the cavity model and numerically using commercial FDTD solver [81] will be given to prove that the proposed mapping of the cavity model to optics is highly accurate.

4.1   RF Patch Antennas and the Cavity Model

The patch antennas, upon their ideation in 1950's [31] and realization in 1970's [32], have been one of the most studied and innovative classes of antenna work in rf, with several variations in patch shape, feeding and substrate configurations, analytical and semi analytical models and design techniques [33]. Patch antennas are prefered low profile antennas for high performance applications like aircrafts and satellites due to their simple fabrication, low-weight, low-cost, easy installation, modification and customization, polarization diversity or dual or multiple functionalities [34].

A typical configuration of a patch antenna consists of a piece of metal trace on a substrate backed by a metal ground plane, as shown in Figure 4-1 for a rectangular patch shape.
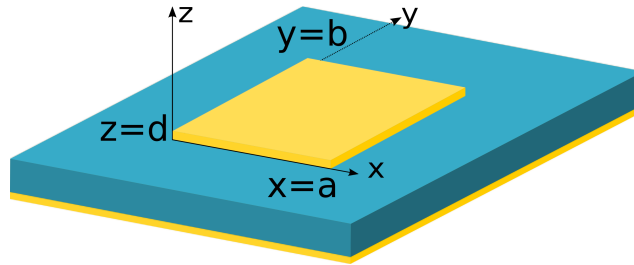
Figure 4-1: A typical rectangular patch antenna in RF, consisting of a metallic patch with dimensions $a \times b$ and thickness d on a dielectric substrate backed by the ground plane.

Regardless of the operating mode, transmitting or receiving, the current on the patch and the associated fields between the patch and the ground plane are excited either by a feed or incident wave. Since the thickness of the substrate is usually quite small as compared to the wavelength of operation, the electric field components parallel to the metal plane would be negligible throughout the substrate, resulting in $E_z(x, y)$, $H_x(x, y)$ and $H_y(x, y)$ field components only. If the characteristic length of the patch (a or b for the rectangular patch in Figure 4-1) is close to $\lambda/2$ or its integer multiple, the patch element resonates and sustains relatively large currents and associated fields in the structure, becoming the source of radiation.

Due to the equivalence theorem, there are basically two interpretations of the radiation mechanism of such antennas [35]: Either the antenna can be viewed i) as the patch with the resonating current on, or equivalently, ii) as a cavity formed by the patch and the ground plane enclosed laterally by the slot-type radiators with the resonating field inside. As a result, the cavity interpretation for the radiation has inspired a model, known as the cavity model, that has proven to be very efficient, intuitive, easy to understand and use for the analysis and design of patch antennas of some canonical shapes [36–38].

The most popular RF patch antenna analysis methods are the cavity model, transmission line and the full-wave method using the MoM. TL model is the easiest of all, yet with less accuracy. Full wave method has computational constraints. Cavity model, on the other hand, is an easy-to-understand and easy-to-implement analysis tool. The importance of this method is not its simplicity in understanding and imple-

mentation, rather its applicability to a broad class of patch antennas with a wealth of applications developed in rf, and more importantly its ability to provide intuition with which one can assess the outcome without going through trial-and-error simulations with no or little intuitive guidance by the user.

4.1.1   RF Patch Antenna Feeding Methods

Currents on the RF patch antenna and the corresponding electric and magnetic field distributions inside the dielectric substrate are excited by a feed. There are various methods for feeding the patch antenna [36] while the most common two are the probe and the slot feeding shown in Figures 4-2(a) and 4-2(b) respectively. RF antennas are fed via TLs that excite electric or magnetic currents and these excited currents couple to electric ($\mathbf{J} \cdot \mathbf{E}$) or magnetic ($\mathbf{M} \cdot \mathbf{H}$) fields. The aim of the feeding is precise in antenna theory, to generate proper antenna modes so that the antenna radiates in a particular direction.

(a)   (b)
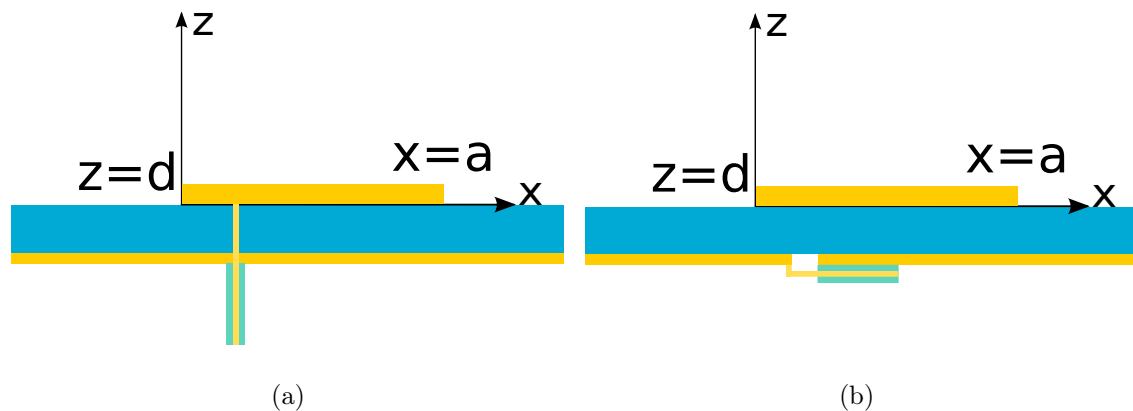
Figure 4-2: RF patch antenna feeding methods a) RF patch antenna probe feeding. TL is soldered beneath the patch generating an electric current in the dielectric substrate that couples to the electric field within the cavity b) RF patch antenna slot feeding. TL is soldered on both ends of a slot on the ground plane, exciting a magnetic current that couples to magnetic fields of the cavity for slot feeding.

4.1.2 Cavity Model

Equivalence theorem demonstrates that the radiation due to the surface current resonating on the patch antenna resembles the one due to the resonating fields inside the cavity equivalent of the patch antenna [35] and inspires the cavity model that calculates the normalized fields within the dielectric substrate by treating that region as a cavity, bounded by electric conductors above and below and magnetic walls along the perimeter of the patch as shown in Figure 4-3. In order to reach the cavity equivalent of the RF patch antenna, the electric field parallel to the metal plane is neglected since the substrate is considered to be thin enough. The patch is replaced with a metal slab slightly larger than the actual patch size so that the fringing fields are included. The cavity equivalent for the patch antenna is observed in Figure 4-3 with metal planes on top and bottom, considered to be Perfect Electric Conductor (PEC), and Perfect Magnetic Conductor (PMC) walls on the sides.
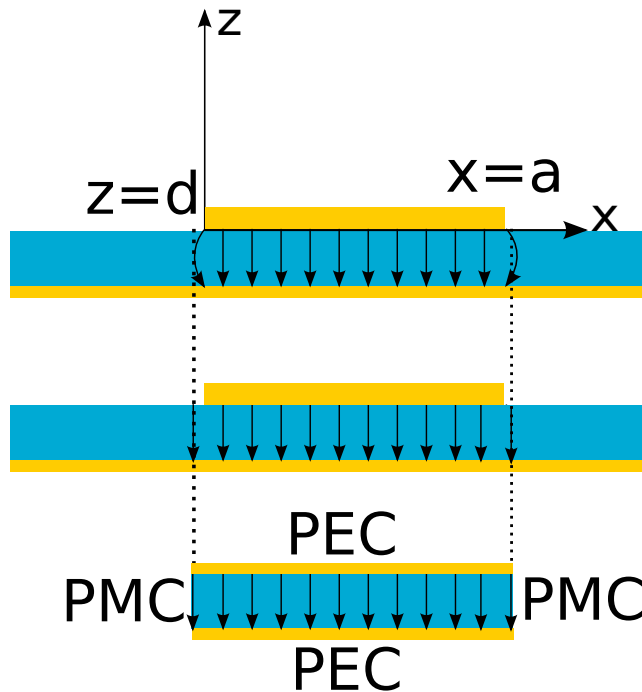
Figure 4-3: Cavity equivalent of the RF patch antenna. PEC at $z = 0, d$ and PMC at $x = 0, a$ and at $y = 0, b$ for a rectangular patch antenna as in Figure 4-1.

The salient feature of the approach is that it can provide analytical expressions for the fields inside the cavity of some canonical shapes [37], where the closed-form solutions Ψ_{mn} of the scalar wave equation $\nabla^2\Psi + k^2\Psi = -\delta$ are possible with appropriate boundary conditions.

Once the equivalence is established between the cavity and the patch, the fields inside the cavity can be expressed as a superposition of all possible orthonormal modes

$$E_z = \sum_{m,n=0}^{\infty} E_{mn}\Psi_{mn} \tag{4.1}$$

where $\Psi_{mn}(x,y) = cos(\frac{m\pi}{a}x)cos(\frac{n\pi}{b}y)$ for a rectangular patch as in Figure 4-1, and are shown below for other shapes [37]. Hence, all relevant antenna parameters, such as, current distribution on the patch, stored and radiated energy, radiation pattern and related impedances, can be obtained in closed forms, enabling the computation of these parameters, and in turn, the design of the antenna with little effort and great intuition.

Table 4.1: Patch Antenna Shapes and Closed-form Mode Distributions

Rectangle
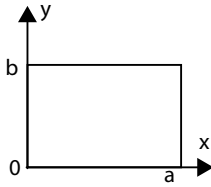
$\Psi_{mn} = cos(\frac{m\pi}{a}x)cos(\frac{n\pi}{b}y)$

$k_{mn} = \sqrt{(\frac{m\pi}{a})^2 + (\frac{n\pi}{b})^2}$

Circle
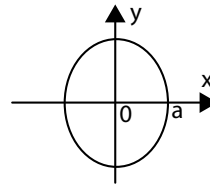
$\Psi_{mn} = J_n(k_{mn}\rho)e^{jn\phi}$

$J'_n(k_{mn}a) = 0$

Ellipse
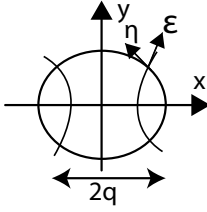
$$\Psi_{mn} = Re_m(\epsilon, \chi e_n) Se_m(\eta, \chi e_n)$$

$$Re_m(a, \chi e_n) = 0, chie_n = kq$$

major axis $2q\cosh(a)$ minor axis $2q\sinh(a)$

odd modes: replace e by o above

Equilateral Triangle

$$\Psi_{mn} = cos(\tfrac{2\pi l}{3b})(\tfrac{u}{2} + b)cos(\tfrac{\pi(m+n)(v-w)}{9b}) +$$

$$cos(\tfrac{2\pi m}{3b})(\tfrac{u}{2} + b)cos(\tfrac{\pi(n-L)(v-w)}{9b}) +$$
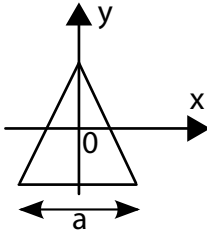
$$cos(\tfrac{2\pi n}{3b})(\tfrac{u}{2} + b)cos(\tfrac{\pi(L-m)(v-w)}{9b})$$

$$L = -(m+n), u = \tfrac{\sqrt{3}}{2} + \tfrac{1}{2}y$$

$$v - w = -\tfrac{\sqrt{3}}{2}x + \tfrac{3}{2}y, b = a/2\sqrt{3}$$

$$k_{mn}^2 = (\tfrac{4\pi}{3a})^2(m^2 + n^2 + mn)$$

Right Isosceles

$$a)\Psi_{mn} = cos(\tfrac{m\pi}{a}x) - cos(\tfrac{m\pi}{a}y)$$
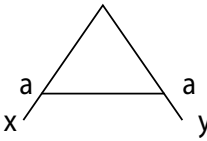
$$k_{mn} = \sqrt{2}\tfrac{m\pi}{a}$$

$$b)\Psi_{mn} = cos(\tfrac{m\pi}{a}x)cos(\tfrac{m\pi}{a}y)$$

$$k_{mn} = \sqrt{2}\tfrac{m\pi}{a}$$

Circular Ring Segment
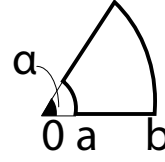
$$\Psi_{mn} = [N'_\nu(k_{m\nu}a)J_\nu(k_{m\nu}\rho) -$$

$$J'_\nu(k_{m\nu}a)N_\nu(k_{m\nu}\rho)]cos(\nu\rho)$$

$$\nu = n\pi/a$$

$$\frac{J'_\nu(k_{m\nu}a)}{N'_\nu(k_{m\nu}a)} = \frac{J'_\nu(k_{m\nu}b)}{N'_\nu(k_{m\nu}b)}$$

Circular Ring
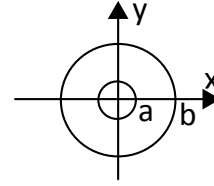
$$\Psi_{mn} = [N'_n(k_{mn}a)J_n(k_{mn}\rho) -$$

$$J'_n(k_{mn}a)N_n(k_{mn}\rho]e^{jn\phi}$$

$$\frac{J'_n(k_{mn}a)}{N'_n(k_{mn}a)} = \frac{J'_\nu(k_{m\nu}a)}{N'_\nu(k_{m\nu}a)}$$

Circular Segment

$$\Psi_{mn} = J_\nu(k_{m\nu}\rho)cos(\nu\phi)$$
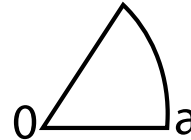
$$\nu = n\pi/a, J'_\nu(k_{m\nu}a) = 0$$

Disk with slot
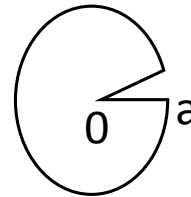
$$\Psi_{mn} = J_{n/2}(k_{mn}\rho)cos(n\phi/2)$$

4.2 Optical Patch Antennas

After having established a strong analogy between optical and RF antennas [30], and having developed fabrication techniques that can produce structures at nanometer precision [22], both of which are essential to realize the full potentials of antennas, there has been an intense study on the use of antennas in optics, ranging from infrared imaging [8], high-resolution microscopy [6, 9, 39, 40] to solar cells [41, 42], optical sensors [43], metasurfaces [44] and graphene detectors [45], and many more. It should be stressed here that, in most optical antenna applications, the term "design" of the antenna merely refers to the optimization of the dimensions of the antenna using one of the commercially available full-wave Maxwell solvers, like FDTD and FEM, which are widely used in optical antenna optimization [46, 47]. Although such rigorous full-wave Maxwell solvers are readily available and provide accurate results, they are usually burdened with a large number of discretization of the solution domain (usually surfaces for MoM and volumes for FEM and FDTD), and perhaps more importantly for antenna design, they are impenetrable and incapable of providing any intuition to users. Motivated from such an intense study and the possibility of widespread use of antennas in optics, and the need for a design tool that builds intuition on the operation of antennas in optics, the cavity model for patch antennas, with all their bells and whistles in RF, are introduced and translated into the optical frequencies, despite the fact that material properties and wave-matter interaction are almost completely different in these two frequency regimes.

It would be instructive to briefly mention and to give due credits to a few uses of patch antennas in optics, mainly to put things into perspective. Recently, there have been a few applications of patch antennas in optics; namely, to achieve a large Purcell factor, collection efficiency and spectral width [48], or to achieve inter- or intra-chip optical communications and sensing [23], or to control the spontaneous emission rate and the radiation pattern of quantum dots [49]. Apart from their intended use in optics, the tools that are used to analyze these patch antennas have been either the simplest model, namely the transmission line model [2], with mediocre

accuracy, little intuition and limited to rectangular patches only [23, 50], or the full-wave approach with good accuracy but no intuition at all [48, 49]. However, the one that has been an inspiration for this study is the design of optical patch antennas for single photon emission using surface plasmon resonance [48], where they considered a thin metallic patch as an SPP cavity. Hence, we have realized that, to employ the cavity model, one does not need to have two parallel metal plates to form a cavity, instead a free-standing metal patch of one of the canonical shapes, or the metal patch over a dielectric substrate, or the metal patch over a dielectric substrate backed by another metal plane can be considered as a patch antenna suitable for the Cavity Model, provided the complex reflection coefficients from the edges of the patch can be obtained.

Here, considering the optical patch antenna geometry in Figure 4-4 the validity of the proposed mapping of the cavity model for intuition on the optical antenna behaviour and the resonance will be validated.
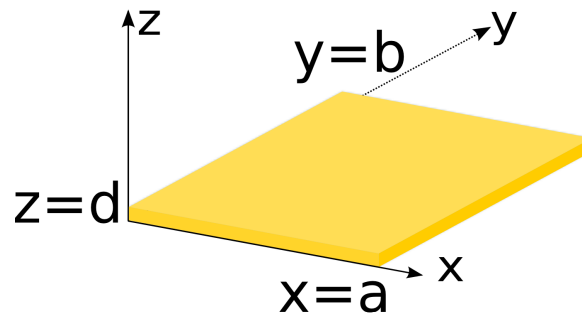
Figure 4-4: Optical patch antenna made of a single metal layer with sizes a, b and thickness d.

4.2.1 Mapping of the Cavity Model to Optics

In the RF patch antenna design and analysis by the cavity model, the complex excitation wavenumber k, at which the antenna operates, can be obtained by lumping all the losses into a single "effective dielectric loss" as $k = k_0\sqrt{\epsilon_r}$ [82]. A reasonable mapping of RF to optical regime is reached through the equivalency of the effective wavenumber as $k = k_0\sqrt{\epsilon_r} = k_{eff}$. Thus, the cavity model, in order to predict the

optical antenna behavior, is mapped to optics by embedding metal losses, arising due to real, dispersive metal behavior in the optical regime and the imperfect reflections from the antenna terminations, into a complex dielectric permittivity of the substrate ϵ_r in Figure 4-1, as in (4.2).

$$\epsilon_r = (\frac{k_{eff}}{k_0})^2 \tag{4.2}$$

Optical antennas cannot be fed via TLs, instead optical means of the two most commonly used RF patch antenna feeding techniques are given in Figure 4-2.

(a) (b)
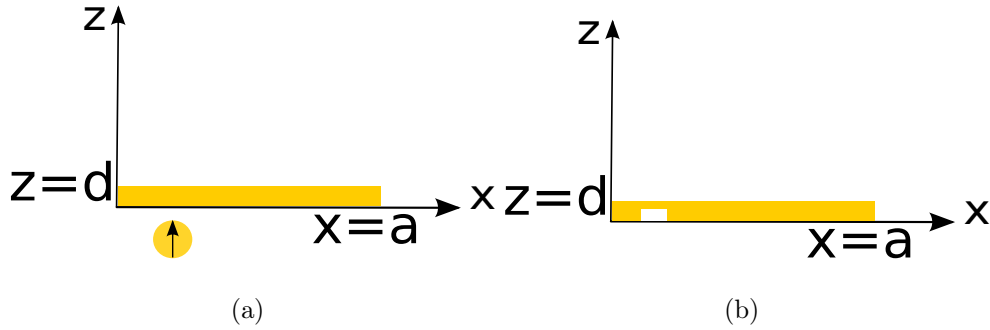
Figure 4-5: Practical means of feeding in RF and Optical regimes. a) Optical means of probe feeding with a NP in the vicinity. b) Optical means of slot feeding via a hole/dent.

The resonant lengths have to be obtained for the optical patch antennas as well as a feed analog has to be defined. Both these challanges are identified in the previous chapters, and some solutions are proposed.

For the sake of illustration, a free-standing, rectangular gold patch in Figure 4-4 with the thickness $d = 50$nm is illuminated by a plane wave ($\lambda_0 = 1100$nm) to support the SPP at the gold-air interface, with $k_{SP} = 5.8 \times 10^6 + i1.05 \times 10^4$ ($\lambda_{SP} = 1083$nm). It is safe to assume that k_{SP} is independent of the length and width of the antenna, as the resonator (i.e., the patch) is not well below the diffraction limit. Therefore, the effective wavelength is computed as $\lambda_{eff} = 540$nm from (3.4) by using the complex reflection coefficient $\Gamma e^{i\Phi_\Gamma} = 0.095e^{i0.49\pi}$ obtained analytically for the IMI structure in (3.17).

In order to verify the computed data for the effective wavelength and the reflection

coefficient, the total scattered power from the gold patch antenna, with the dimensions of $a = b = \lambda_{eff}/2 = 270$nm and $d = 50$nm, as a function of wavelength is obtained from a commercial-grade simulator based on the FDTD method [81] (Figure4-6). Knowing that the scattered field intensity is at its maximum at resonance, the peak of the scattered field upon plane wave excitation in Figure 4-6 shows the resonant wavelength at 1040nm, which is off by 60nm, corresponding to around 5° error in the phase of the reflection coefficient, that is 1.5nm difference in the antenna resonant length. Considering that the fabrication precision is on the order of a few nm, the calculated effective wavelength based on the analytical calculation of the reflection coefficient can be used for all practical purposes. As a result, the quality factor Q can be calculated as 1.65 and the effective wavenumber k_{eff} is obtained as $1.16 \times 10^7 + i3.5 \times 10^6$.

With this verification, it has been established that the square gold patch antenna ($a = b = 270$nm, $d = 50$nm) can be used for the demonstration of the cavity model in optics.
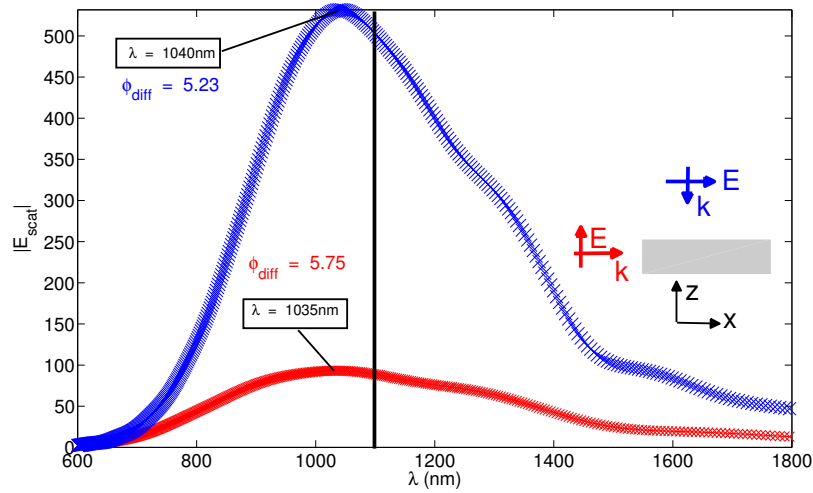
Figure 4-6: Total scattered power measured on a box of monitors around the optical patch antenna made of gold with sizes $a = b = 270$nm and thickness $d = 50$nm for plane wave excitations of two different polarizations: TM given in (blue) plus and TE in (red) cross at the insets. The black line shows the excitations wavelength $\lambda_0 = 1100$nm. ϕ_{diff} refers to the difference between the analytically calculated and the indirectly observed phases of the reflection coefficient.

87

4.2.2 Mode Excitations and Radiation Patterns

The cavity model provides a strong insight and intuition on the modes as well as the radiated fields of the antenna. This statement still holds for the optical patch antenna studied here, where there is no actual cavity, provided that the similar surface currents (antenna modes) are observed upon similar feeding strategy.

As a result of the cavity model, one can define modes of the antenna in terms of the modes of the cavity which are referred to TM_{mn} modes. Therefore, the field profile corresponding to a specific mode dictates where to position the source, whether it is a NP (metallic or molecular) above the patch or a small discontinuity (gap, dent, etc.) on the patch, in order to excite the required current distribution on the patch and, in turn, the radiation pattern and the polarization of the radiation. That is, one needs to position the source, with the dipole moment $\boldsymbol{\mu}$, where it couples the most to the electric field of the desired mode and less or none to that of the undesired mode, as the change of energy dissipation of a dipole in inhomogeneous environment is proportional to $\text{Im}\{\boldsymbol{\mu^*} \cdot \boldsymbol{E_s}\}$ [54].

Based on the modal profile in (4.1) predicted by the cavity model, $|E_z|$ is zero (has a null) at $y = b/2$ for TM_{01} mode and at $x = a/2$ for TM_{10} mode. In Figure 4-7 the corresponding cavity mode that is obtained analytically is seen upon probe feeding and with good agreement to the numerical simulation results.
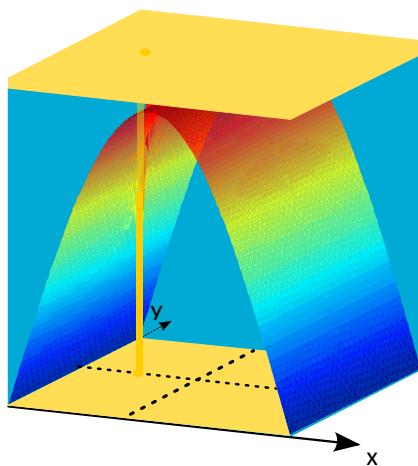
Figure 4-7: Cavity mode on cavity equivalent of RF patch antenna upon probe feeding at $(a/4, b/2)$ for TM_{10} mode excitation.

An electric dipole coupling to the optical antenna from the vicinity ($x_0 \neq a/2$, $y_0 = b/2$, $z_0 = -15$nm) will excite only the TM_{10} mode. The current distributions on the patch obtained by the Maxwell solver upon $x_0 = a/4$ and $x_0 = 3a/4$ are shown in Figures 4-8(a), 4-8(b). Although the same standing wave would be observed upon probe feeding of the RF patch antenna at $(a/4, b/2)$ and $(3a/4, b/2)$, a slight difference is observed on the standing waves upon these two feeds in optical patch antenna. The asymmetry in the standing wave affect the far field radiation as well.

Although there is no actual cavity for the optical case in Figure 4-8, the mode distributions and the radiation patterns show that the predictions of the cavity model are in good agreement with the actual results and can provide a good starting point in the design of an optical patch antenna.

(a)   (b)
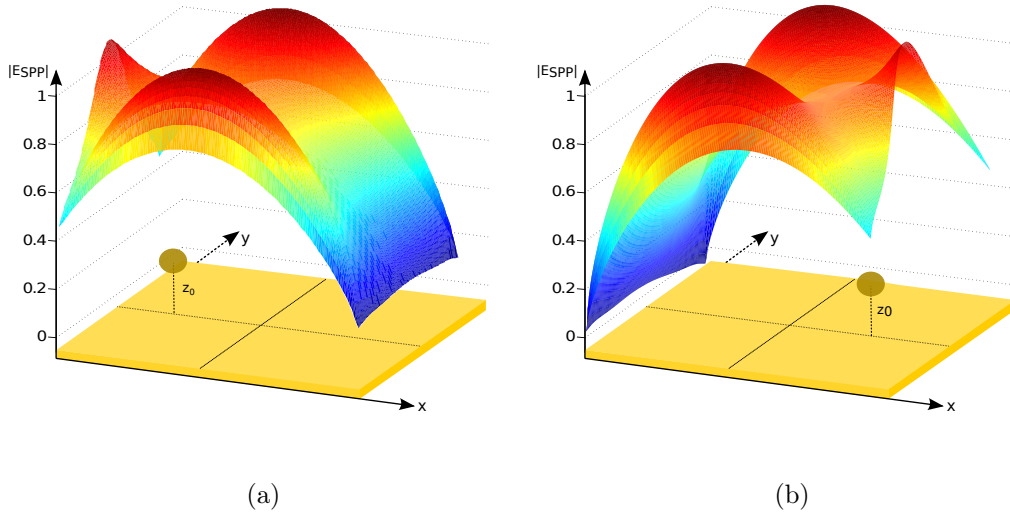
Figure 4-8: TM_{10} mode excitation on the optical patch antenna. a) Surface current distribution on optical patch antenna upon coupling to NP oscillating in the vicinity to feed point $(a/4, b/2)$. b) Surface current distribution on optical patch antenna upon coupling to NP oscillating in the vicinity to feed point $(3a/4, b/2)$. These two feedings both excite TM_{10} modes on the optical antenna with asymmetry in the mode distributions.

The radiation patterns are generally given in a similar manner as for dipole antennas on E and H planes for co (parallel) and cross (perpendicular) polarizations [3]. Therefore, before showing the radiation patterns, the E and H planes are defined for the TM_{10} mode in Figure 4-9. Electric current distribution is observed on the $x - z$ surface of the antenna for TM_{10} mode upon probe feeding; hence $x - z$ is the E plane and consequently $y - z$ is the H plane. The co-polarized radiation is from the component of the electric field that is parallel to the surface current which for TM_{10} mode is the J electric current; and the cross-polarized radiation is the one due to the fields perpendicular to J. Co-polarized radiation is stronger than cross-polarized [3].
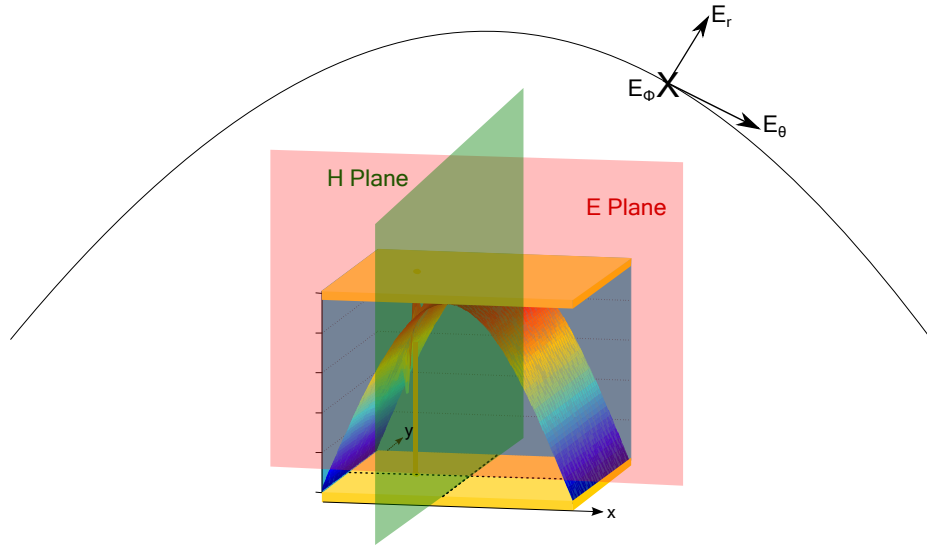
Figure 4-9: E and H planes for the far field radiation pattern of TM_{10} mode

In Figure 4-12, the parallel (co) polarization radiation patterns are given for TM_{10} mode excitations from symmetric $(a/4, b/2)$ and $(3a/4, b/2)$ locations. The co-polarization H plane radiation pattern for the optical patch antenna highly correlates with the cavity model predictions in Figures 4-10(b)-4-10(d) for both $(a/4, b/2)$ and $(3a/4, b/2)$ feedings. This is expected since a constant field distribution is observed in H plane for both RF and optical regimes. The co-polarization E plane radiation pattern for optical patch antenna, on the other hand, provides a contribution that arises from the lossy metal behavior and the imperfect reflections in this regime as given in Figures 4-10(a)-4-10(c). A tilt in the E_θ is seen instead of a uniform

pattern as predicted by the cavity model, which would have a high impact on sensor applications. The radiation is tilted in opposite directions according to the source location as seen in Figure 4-12. This behavior in the optical regime holds an advantage in sensing applications owing to the ability to differentiate between different feed locations that generate the same antenna mode, a behavior that would not be seen in RF.
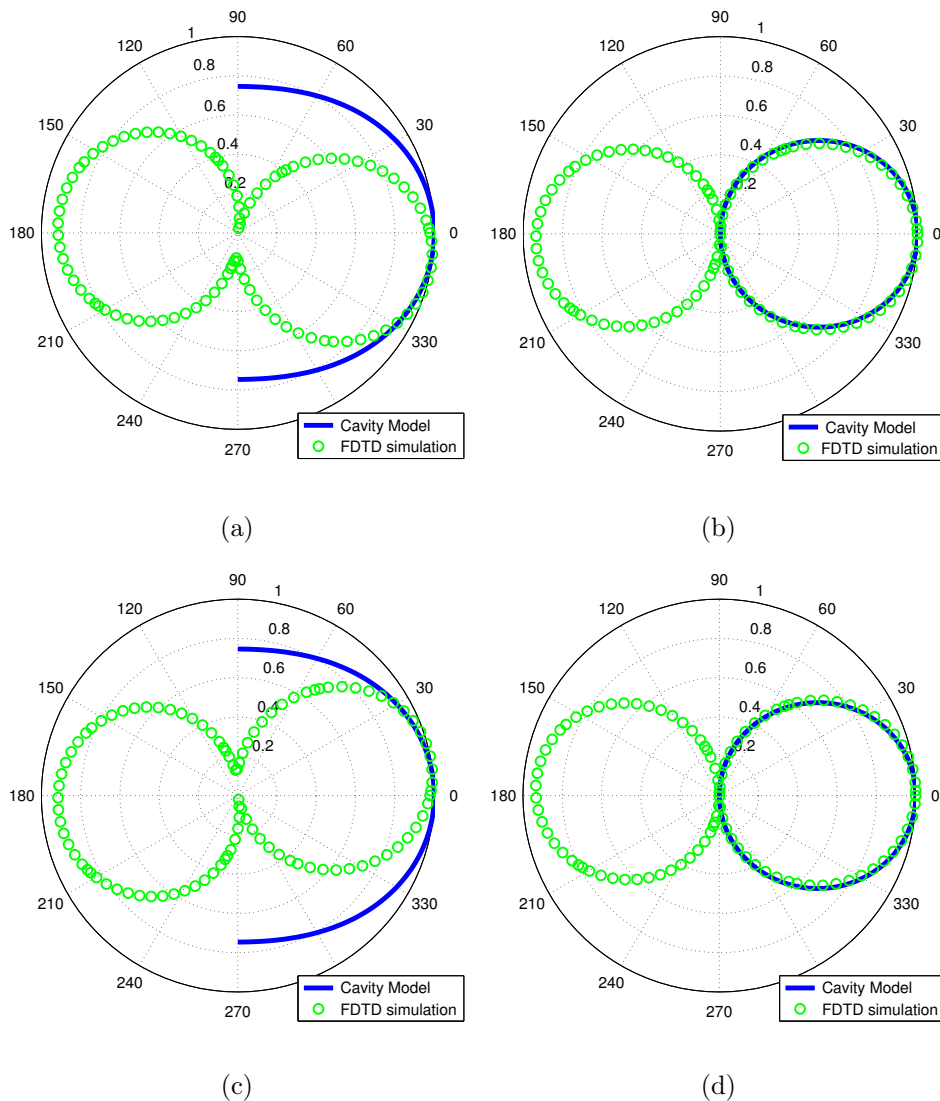
Figure 4-10: Co-polarized radiation patterns. a) $(a/4, b/2)$ feed co-polarized radiation $|E_\theta|$ in E plane b) $(a/4, b/2)$ feed co-polarized radiation $|H_\phi|$ in H plane c) $(3a/4, b/2)$ feed co-polarized radiation $|E_\theta|$ in E plane g) $(3a/4, b/2)$ feed co-polarized radiation $|H_\phi|$ in H plane. Both the cavity model and the FDTD result is obtained for the scattered field calculated in the far field of the optical patch antenna.

The co-polarization radiation pattern in $E-$plane shows that the lossy metal behavior in optical antennas result in better directivity, sensitive to the feed location. Also, cross-polarization radiation patterns in E and H planes shown in Figure 4-11 are directed oppositely with $(a/4, b/2)$ and $(3a/4, b/2)$ feedings. Cross polarization is not the desired polarization and much weaker compared to the parallel (desired) polarization.
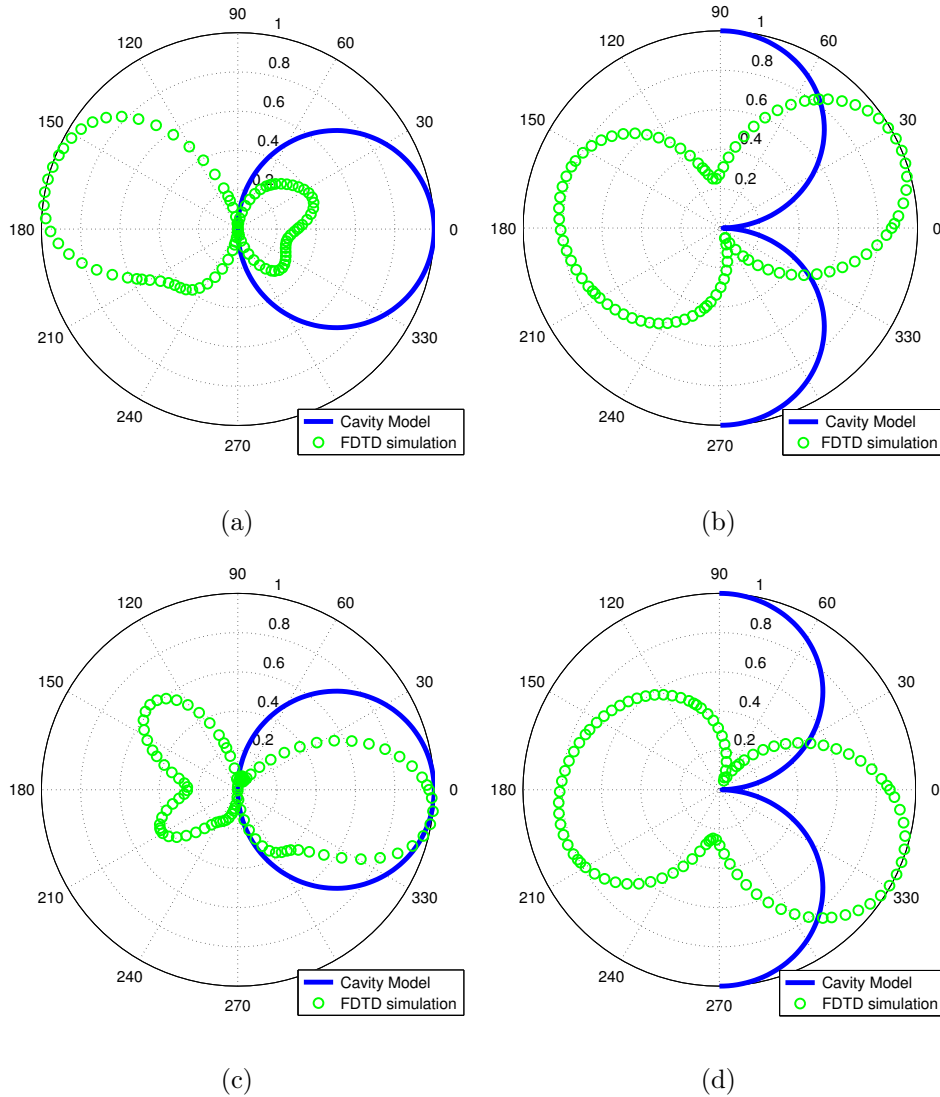
Figure 4-11: Cross-polarized radiation patterns. a) $(a/4, b/2)$ cross polarized radiation in E plane $|E_\phi|$ b) $(a/4, b/2)$ cross polarized radiation in H plane $|H_\theta|$ c) $(3a/4, b/2)$ cross polarized radiation in E plane $|E_\phi|$ d) $(3a/4, b/2)$ cross polarized radiation in H plane $|H_\theta|$. Both the cavity model and the FDTD result is obtained for the scattered field calculated in the far field of the optical patch antenna.

The parallel polarized radiation patterns of the total field due to the dipole excitation and the radiation from the optical patch antenna with TM_{10} mode excitation is given in Figure 4-12.
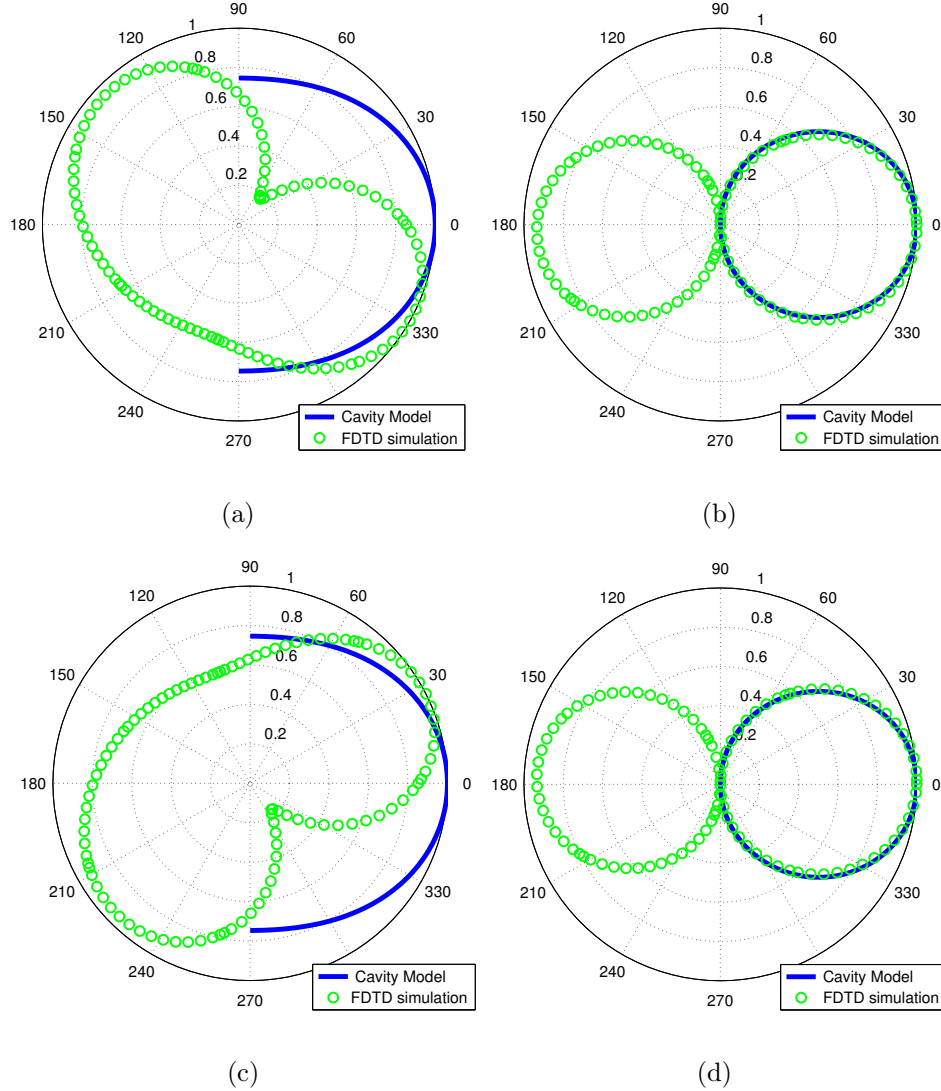
Figure 4-12: Co-polarized radiation patterns. a) $(a/4, b/2)$ feed co-polarized radiation $|E_\theta|$ in E plane b) $(a/4, b/2)$ feed co-polarized radiation $|H_\phi|$ in H plane c) $(3a/4, b/2)$ feed co-polarized radiation $|E_\theta|$ in E plane g) $(3a/4, b/2)$ feed co-polarized radiation $|H_\phi|$ in H plane. The cavity model result is for the scattered field. The FDTD result is the total field calculated in the far field of the optical patch antenna.

The asymmetric mode distribution in the optical domain resulting in a new feature of exactly distinguishing between two feeds $(a/4, b/2)$ and $(3a/4, b/2)$ as seen in Figure 4-13.
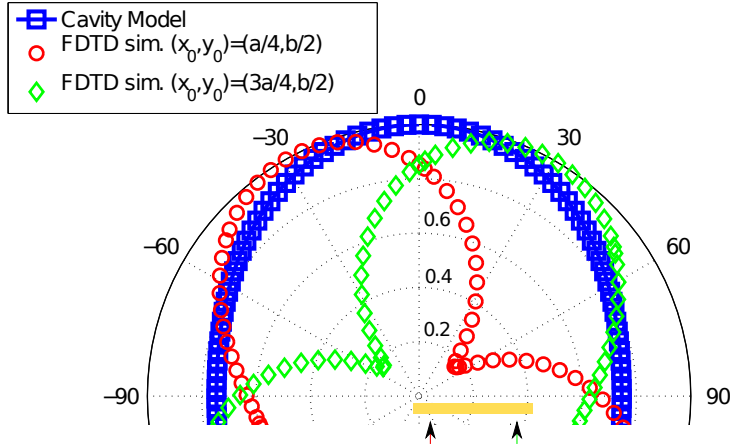
Figure 4-13: Co-polarized ($|E_\theta|$) radiation patterns of the total field in electric plane for feeds $|E_\theta|$ and $|E_\theta|$.

TM_{01} mode is excited on the optical patch antenna by feeding in the mid-x axis whereas anywhere apart from center in y-direction on $x_0 = a/2$ line. The E and H plane co-polarized radiation patterns for TM_{01} mode are shown in Figures 4-14(a) and 4-14(b) respectively. A tilt in $E-$plane is observed due to the metallic loss and the imperfect reflections in optics. Lossy metal behavior happens to be an advantage in optics with promising applications in sensing.

(a)   (b)
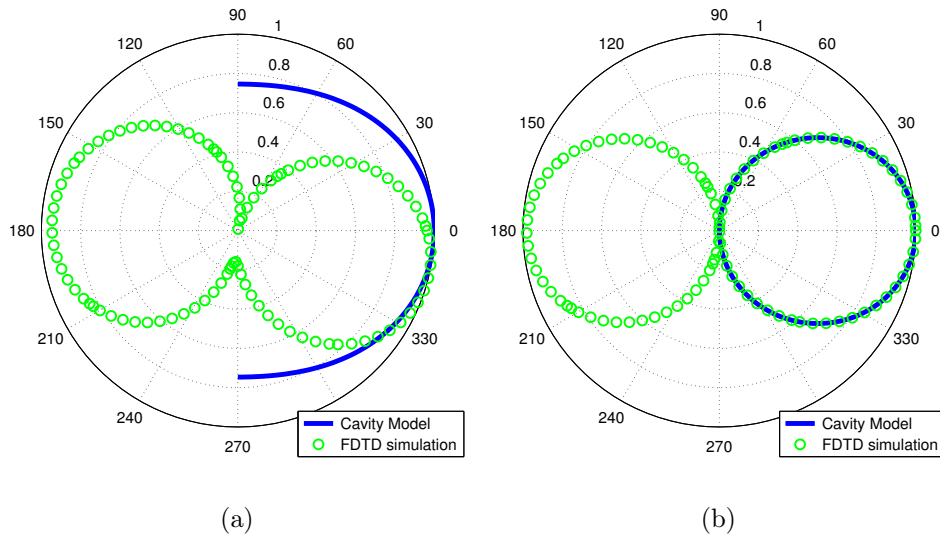
Figure 4-14: TM_{01} radiation patterns upon $(a/2, b/4)$ feeding a) co (parallel) polarized radiation in E plane E_θ b) co (parallel) polarized radiation in H plane H_ϕ.

After having extensively studied the current distributions and the radiation patterns in E and H planes for the TM_{10} and TM_{01} modes for various feed locations, here are some of the observations: i) The radiation pattern in H-plane for the optical patch antenna highly correlates with the cavity model predictions (Figures 4-10(b), 4-10(d)); ii) current density along the resonating length shows a standing wave nature, but not exactly symmetric as it is for the cavity model, which is attributed to the loss mechanism in the metal and imperfect reflections from the edges of the patch as a result of the asymmetry (Figure 4-8), iii) the radiation pattern in E plane has become more directive and tilted slightly from the broadside (Figures 4-10(a), 4-10(c)), and iv) symmetric feed locations with respect to the center of the patch provide mirror image symmetric profiles for both current density and radiation pattern, which may play an important role in sensing applications owing to the ability to differentiate between different feed locations that generate the same antenna mode, a behavior that would not be seen in RF.

Conclusion

In this chapter, after RF antennas and the cavity model have been introduced, a mapping of the cavity model to optics is proposed. Extensive study on the feeding of the antenna and the resulting mode distribution on the optical patch antenna surface even in the absence of a physical cavity together with the strong agreement of the corresponding radiation patterns is a proof for the validity of the proposed mapping.

Based on the study of the current distributions on and the radiation patterns from the rectangular patches, it has been established that the optical patch antennas can be designed by using the cavity model, at least for the initial design phase where one defines the dimensions of the patch according to the intended frequency of operation and the feed location(s) for the intended radiation pattern and polarization.

Throughout this study, the main focus has been the transfer of knowledge for the patch antennas in RF, accumulated more than three decades, into optics with special emphasis given to the cavity model; a simulation tool that has been the most popular, intuitive and accurate enough for RF patch antennas. Since the cavity model was originally proposed and developed for patch antennas that are surrounded by perfect electrical and magnetic conductors, mapping it into optics, where metals are no longer perfect conductors, has been proposed. It has been observed that the cavity model equivalent in optics has achieved the intended goal, i.e., providing intuition on the operation of the patch antennas. That is, the current distribution on the patch and the associated radiation pattern can now be imagined for a given location of the feed in optics as well.

Chapter 5

Control over Resonance and Polarization

The expression of the current distribution on the patch obtained by the cavity model can be used to decide where to feed the patch to excite a specific mode and the corresponding radiation and the polarization of the radiation, and/or how to tweak the geometry to tune the resonance, and/or where and how to feed it to get circularly polarized (CP) radiation. Knowing the current distribution of a mode or the combination of the modes of an equivalent cavity guides antenna designer where to locate the source on the patch in order to excite that mode, and provides intuition how to tune the resonance, radiation pattern and polarization of the antenna. In this chapter the tuning of the resonant frequency and the feeding for the CP operation will be discussed under the light of the cavity model.

5.1   Tuning the Resonance Frequency

For RF patch antennas, tuning the resonant frequency of a mode can simply be achieved by introducing a thin slot of length l and width w on the patch that effectively increases the resonant length of that mode, and in turn, decreases the resonant frequency as shown in Figure 5-1 for the implementation in optics.
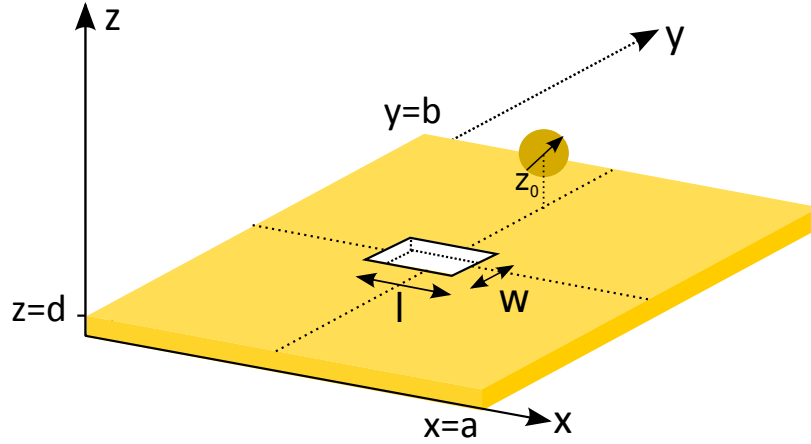
Figure 5-1: A slot of length l, width w, height d on the optical patch antenna for tuning the resonance wavelength. The antenna sizes here are $a = b = 270$nm, $d = 50$nm and the antenna is made out of gold. The dipole source is at $z_0 = -15$nm.

The general topology of the equivalent circuit of the RF patch antenna operating at its (m, n) mode band is given in Figure 5-2 [83]. The circuit interpretation of the resonance tuning is quite simple, as the narrow slot can introduce a parallel capacitor $C_{slot}(\propto ld/w)$ to the equivalent resonant circuit of the mode (m, n) [38], resulting in a shift of the resonant frequency, defined by $f = 1/2\pi\sqrt{L_{mn}(C_{mn} + C_{slot})}$.
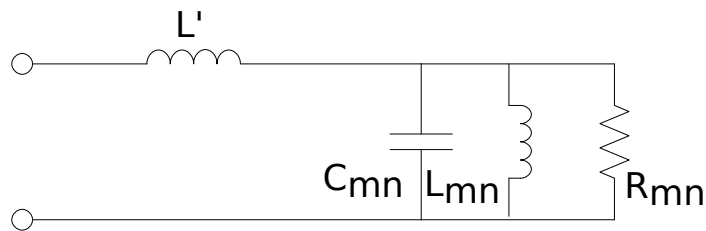
Figure 5-2: The circuit model for patch antenna operating at its (m, n) mode band where L' corresponds to the higher order modes' contribution.

The frequency is inversely and the resonant wavelength is directly proportional to $C + C_{slot}$. C_{slot} decreases with increasing w, as a result of decrease in the resonant wavelength. In Figure 5-3 the resonant wavelength has an increasing trend as slot

98

lengths gets bigger since the effective path increases, and so does the capacitance C_{slot}; whereas a decreasing trend is observed as widths get bigger due to capacitive effect.

Although the frequency tuning by introducing a slot on the patch and its simple circuit interpretation of introducing parallel capacitor have been successfully demonstrated in the optical regime, due to a complex behavior of the resonant wavelength as evidenced in Figure 5-4, a slot of different widths and lengths in a patch needs to be studied further.
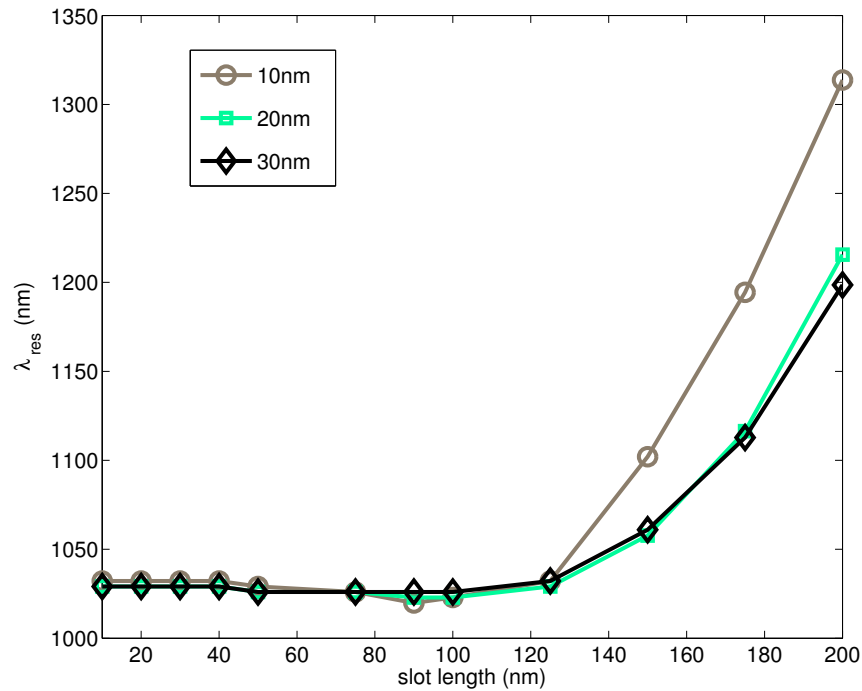
Figure 5-3: The SP resonance wavelength that the slot supports as a function of slot length for different slot widths.
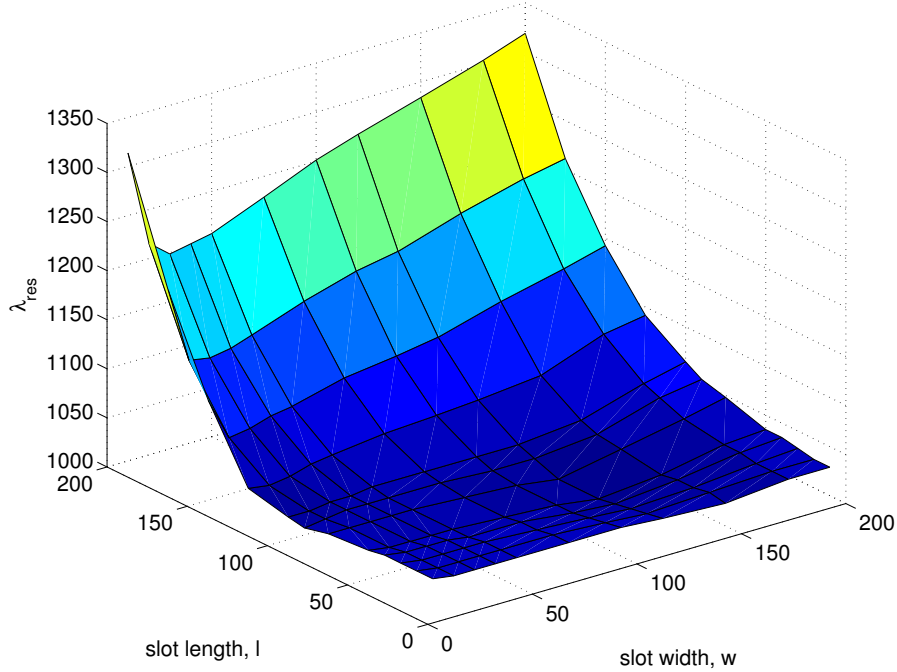
Figure 5-4: The antenna resonance wavelength surface plot wrt width and length of the slot. There is no single behavior seen that can be explained through one mechanism only.

5.2 Circular Polarization

Another attractive feature of the RF patch antennas is their ability and flexibility to produce and control the polarization of the radiation by simply selecting the position of the feed, which may become useful in sensing and imaging in optics. For RF patch antennas, a simple cavity model based approach is used to find the locations of the feed to achieve CP radiation [38]. The model mainly uses the radiation fields at the broadside of the antenna, due to the magnetic current densities for TM_{01} and TM_{10} modes at the edges of the cavity (on the PMC walls of the RF cavity equivalent), to enforce the condition for CP operation, that is, $E_y^{TM_{01}}/E_x^{TM_{10}} = \mp j$ in the far field. This leads to a quadratic equation for the position of the feed (x_0, y_0) with possibly two solutions if the discriminant is a positive real number [36]. However, since the current distributions obtained by the cavity model for the TM_{01} and TM_{10} modes on the antenna do not exactly match the actual current distributions especially near

the edges of the patch, the phases of the electric field components in the far field are expected to show some deviations from those obtained by the cavity model, whereas the magnitudes of the fields are stationary in the far-field zone with respect to small deviations in the source distribution. Moreover, for the optical patch antennas, there is one more degree of freedom for the parameters of the feed which is the polarization of the emitter in addition to its projected location on the patch.

5.2.1 Analytical Derivation of the Feed Locations for CP Operation

One important property of the cavity model is the ability to find the feed locations to drive the antenna for circularly polarized radiation. For the probe feeding case, which has a practical analog of a vertical electric dipole (VED) source excitation in optics, the x and y components of the far field radiation regarding the RF patch antenna with sizes a, b is given in (5.1).

$$E(x) \approx \frac{cos(\pi x_0/a)}{k - k_{10}}$$
$$E(y) \approx \frac{cos(\pi y_0/b)}{k - k_{01}}. \tag{5.1}$$

In order to have CP operation at the far field, the field distributions should be satisfy a ratio of $E_y/E_x \pm j$ where $+j$ refers to Left-Hand Circular Polarization (LHCP) and $-j$ refers to Right Hand (RHCP).

For a rectangular patch antenna $a > b$, one way to determine the feed locations (x_0, y_0) is through the geometric relations as shown in Figure 5-5 for phasors $k - k_{10}$ and $k - k_{01}$ at an angle of 90° [36].
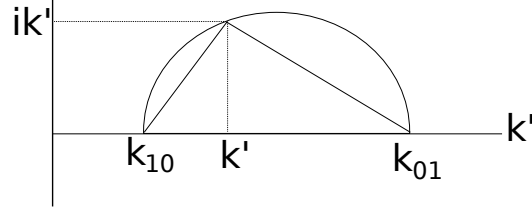
Figure 5-5: Complex k plane showing the geometric relations of phasors k_{10}, k_{01} and k for CP operation.

In order to find the feeding locations for CP operation a series of relations are followed. The ratio of the x and y components of the far field radiation (5.1) can be expressed as in (5.2) where A is defined as in (5.3) which can be expressed as in (5.4) as well.

$$\frac{E_y}{E_x} = \pm j \approx A\frac{k - k_{10}}{k - k_{01}} \tag{5.2}$$

$$A = \frac{cos(\pi y_0/b)}{cos(\pi x_0/a)} \tag{5.3}$$

$$A = \frac{|k - k_{01}|}{|k - k_{10}|} \tag{5.4}$$

The similarities of the triangles observed through phasors in Figure 5-5 lead to (5.5) and (5.6).

$$\frac{|k''|}{k_{01} - k'} = \frac{|k - k_{10}|}{|k - k_{01}|} \tag{5.5}$$

$$\frac{|k''|}{k' - k_{10}} = \frac{|k - k_{01}|}{|k - k_{10}|} \tag{5.6}$$

102

A quadratic equation for A (5.7) can be obtained by combining (5.5) and (5.6) and introducing (5.4).

$$Ak_{01} - A^2|k''| - |k''| - Ak_{10} = 0 \qquad (5.7)$$

The discriminant $\Delta = (k_{10} - k_{01})^2 - 4|k''|^2$ when solving (5.7) for A defines the solution set as two distinct roots for positive discriminant, one real root for zero discriminant and no real roots for negative discriminant. Considering the positive discriminant case two solutions $A_{1,2}$ can be obtained as given in (5.8).

$$A_{1,2} = \frac{-(k_{10} - k_{01}) \pm \sqrt{(k_{10} - k_{01})^2 - 4|k''|^2}}{2|k''|} \qquad (5.8)$$

Replacing these solutions in (5.3) the feed locations (x_0, y_0) for CP operation can be found as in (5.9).

$$\frac{cos(\pi y_0/b)}{cos(\pi x_0/a)} = \frac{\pi}{2} \frac{a-b}{ab} \frac{1}{|k''|} \pm \sqrt{(\frac{\pi}{2} \frac{a-b}{ab} \frac{1}{|k''|})^2 - 1} \qquad (5.9)$$

The current distributions obtained by the cavity model and the Maxwell solver do not exactly match as shown in the previous chapter for TM_{01} and TM_{10} modes, therefore divergence in the phases of the electric fields in the far field is expected. The direct application of the cavity-model based approach to the optical patch antenna discussed and verified earlier was not able to yield positions on the patch for a vertical dipole to generate the CP operation. However, when the optical rectangular patch antenna made out of gold, with the parameters of $a = 275nm$, $b = 265nm$, $d = 50nm$ and $z_0 = -15nm$ is studied for the location and the polarization ($\theta \in [45, 90]$ with respect to z-axis on $x - z$ plane) of an electric dipole using the Maxwell solver, the loci of the feed for the right-handed and the left-handed CP operation are obtained as shown in Figure 5-6. The orientation of the dipole (a combination of VED and HED) introduces a new degree of freedom for the CP analysis in the optical regime that needs to be further analyzed.
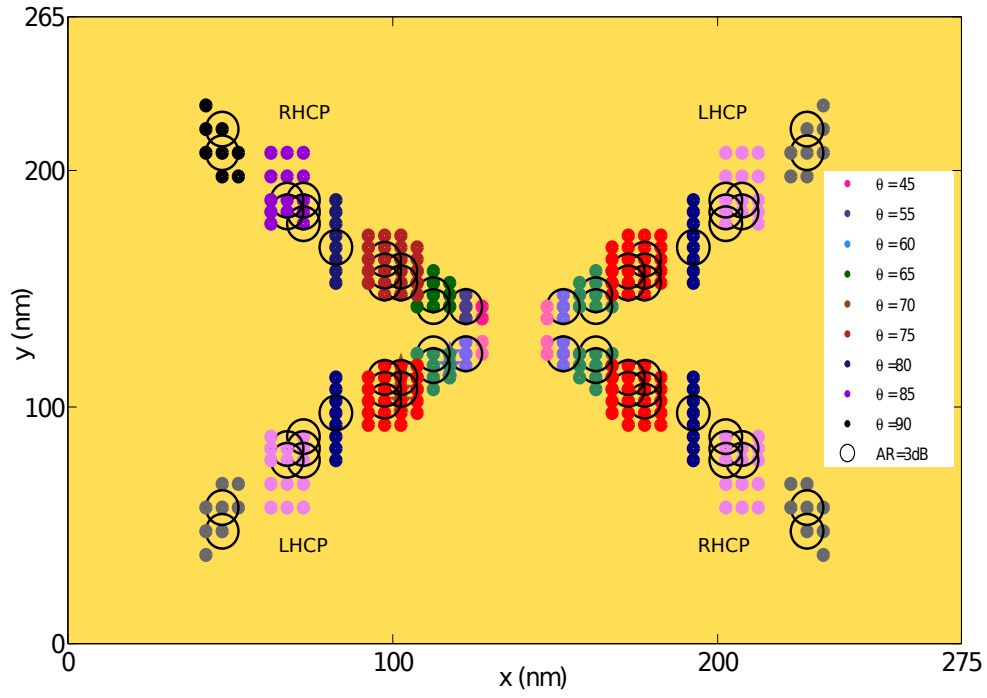
Figure 5-6: Locations and polarizations ($\theta \in [45, 90]$ on $x - z$ plane) of a dipole emitter for the right-handed CP operation of a gold patch antenna. The dots are for the axial ratio of $6dB$, and the black circles are for $3dB$. Antenna parameters: $a = 275$nm, $b = 265$nm, $d = 50$nm, $z_0 = -15nm$.

When the optical antenna with the same effective parameters as $\lambda_{eff} = 540nm$ and $k_{eff} = 1.16 \times 10^7 + i3.52 \times 10^6$ is examined using the analytical approach introduced here to identify the feed locations for CP operation, the feed locations for RHCP and LHCP operations are observed to be very close to the center. The

The solution to (5.7) under a constraint of a zero discriminant produces a curve that fits quite well to the feed locations constructed by the dipole sources with different orientations. The fitting line observed for zero discriminant in the analytical approach is shown in Figure 5-7.
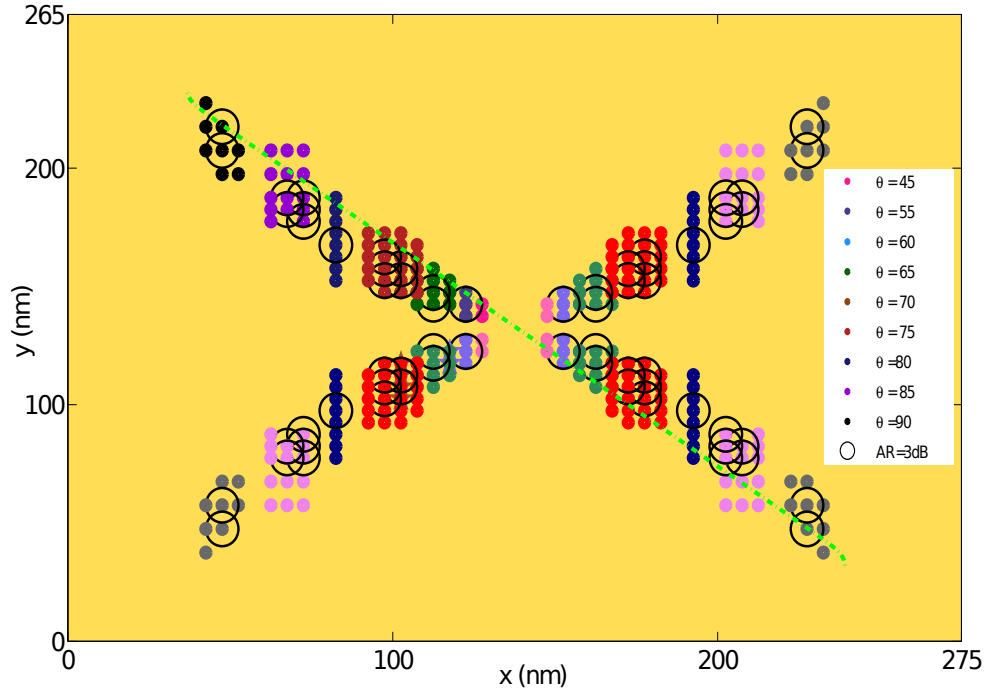
Figure 5-7: Locations and orientations ($\theta \in [45, 90]$ on $x - z$ plane) of a dipole emitter located at $z_0 = -15$nm for the CP operation of a gold patch antenna with dimensions $a = 275$nm, $b = 265$nm, $d = 50$nm. The dots are for the axial ratio of $6dB$, and the black circles are for $3dB$.The fitted (green) dash-dotted line is observed for zero discriminant in the analytical approach.

A proper way of defining the polarization is via Axial Ratio (AR) where AR is the ratio of the orthogonal components of the radiated field. AR for perfect CP is $1(0dB)$ since CP field is created by two orthogonal linear components with the same magnitude. AR tends to degrade away from the main beam, so a range is usually given to define the polarization which is generally $AR < 3dB$. The AR can be calculated by using the polarization ellipse in Figure 5-8.
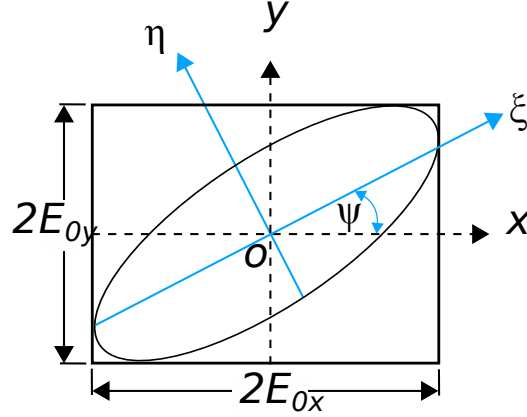
Figure 5-8: Polarization ellipse with x, y and rotated ξ, η coordinate systems and constant E_{ox}, E_{oy} amplitudes.

$E_x(z.t)$ and $E_y(z, t)$ describe sinusoidal oscillations in $x - z$ and $y - z$ planes. The equation of an ellipse in (5.10) is obtained by eliminating the time-space propagator $\omega t - kz$ where $\delta = \delta_x - \delta_y$. Since the equation refers to the polarized light, (5.10) is called the polarization ellipse where a plot of it is given in Figure 5-8.

$$\frac{Ex_{(z,t)}}{E_{ox}^2} + \frac{Ey_{(z,t)}}{E_{oy}^2} - \frac{2Ex_{(z,t)}Ey_{(z,t)}}{E_{ox}E_{oy}}cos\delta = sin^2\delta \qquad (5.10)$$

E_x and E_y field components continue to be time-space dependent and as the polarized beam propagates the polarization ellipse remains fixed due to constant E_{ox}, E_{oy} amplitudes and δ phase.

To assess the quality of the CP operation, the contour graph of the AR is given in Figure 5-9, where the contours of $AR \leq 3dB$ are shown on a surface at a constant z in the far-field zone right at the top of the patch. It is observed that almost perfect CP operation, with the AR of 1.13, is achieved by the patch antenna in optics when it is fed by a dipole emitter with the polarization of $\theta = 85^o$ on $x - z$ plane and located at $(x_0 = 72.5\text{nm}, y_0 = 182.5\text{nm}, z_0 = -15\text{nm})$.
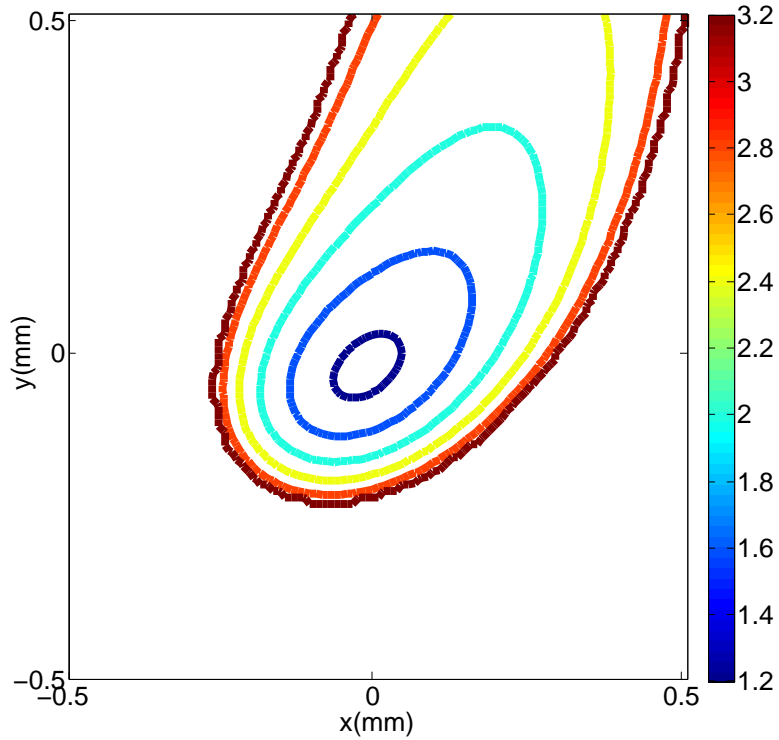
Figure 5-9: Contour plot of AR on $1mm \times 1mm$ surface at $z = 1m$ above the antenna for dipole orientation of $\theta = 85^o$ at feed location of $x_0 = 72.5\text{nm}$, $y_0 = 182.5\text{nm}$, $z_0 = -15\text{nm}$. Parameters of the antenna : $a = 275\text{nm}$, $b = 265\text{nm}$, $d = 50\text{nm}$ and the antenna is made out of gold.

The perfectly fitting curve to the feed locations observed by Maxwell solver for optics shown in Figure 5-7 corresponds to the root of (5.7) for zero discriminant. As observed in the results shown here, direct application of the cavity model based analytical approach needs to be further developed by considering the new degree of freedom, the dipole orientation.

5.2.2   A New Degree of Freedom : Dipole Orientation

The magnitudes of the fields are stationary in the far field zone with respect to small deviations in the source distribution whereas the phases of the electric field components in the far field are expected to show some deviations. The excitation of TM_{10} mode weakens as the emitter approaches to the center in x direction, and a similar behavior is observed for TM_{01} mode when the emitter approaches to center in y direction. An HED on $x - z$ surface ($\phi = 0^o$, $\theta = 90^o$) excites the x component of the electric field stronger than the y component as shown in Figure 5-10.
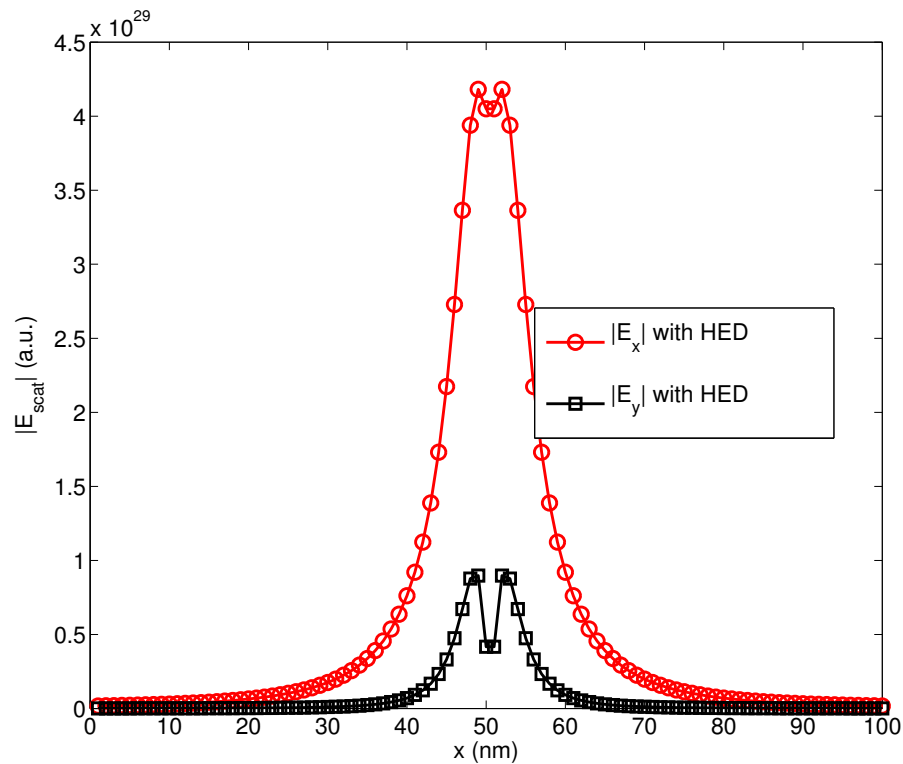
Figure 5-10: The magnitudes of the x and y components of the field excited via HED

The effect of the dipole orientation on the x and y components of the radiated electric field is not straightforward for CP operation. In order to seek for further evidence on the phase deviations, a feed location from Figure 5-7 that drives CP of $AR = 1.16$ is investigated. The excitation of the optical patch antenna is via HED $(\phi = 0^o, \theta = 90^o)$ at $(x_0 = -95\text{nm}, y_0 = 95\text{nm}, z_0 = -15\text{nm})$ feed location and $AR = 1.16$ is obtained with $|E_y|/|E_x| = 1.12$ and $\phi_y - \phi_x = -265^o$. The variations of the magnitudes and phases, and the phase differences of the x and y components of the radiated electric field and the calculated AR are given for different dipole orientations (θ angles) in Figure 5-11.
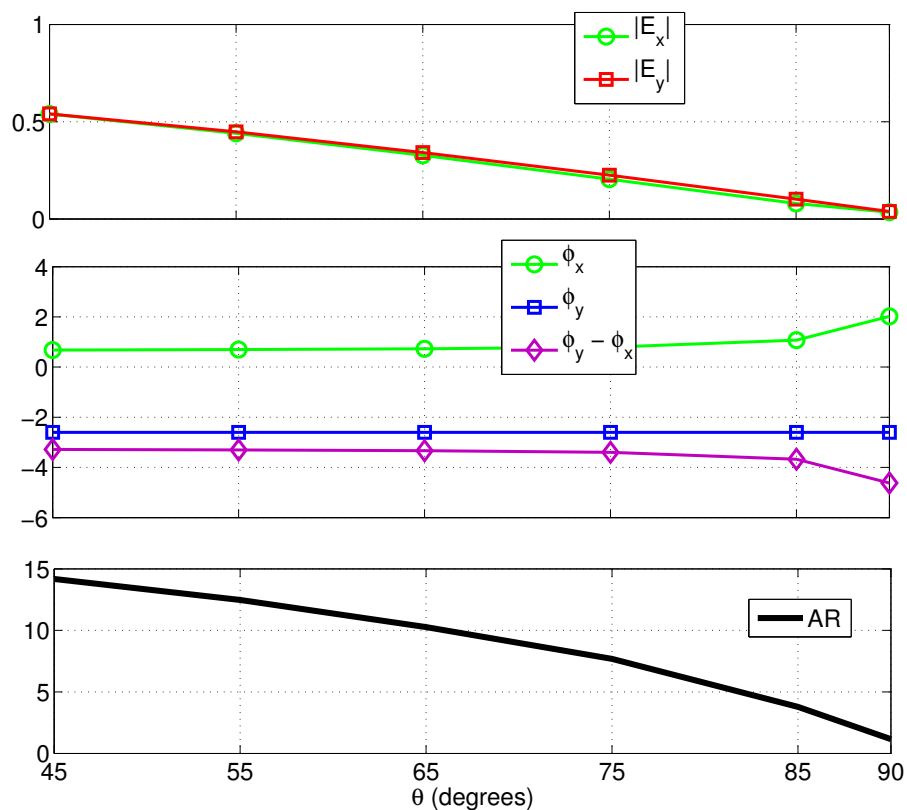
Figure 5-11: The magnitude, phase difference between the x and y components of the radiated electric field and the AR) observed computationally for an optical patch antenna fed from the vicinity of $(x_0 = -95\text{nm}, y_0 = 95\text{nm}, z_0 = -15\text{nm})$ with respect to different dipole orientations (θ).

$AR = 1.33$ is seen upon feeding with a dipole source that has $\theta = 85^o$ and is located at $z_0 = -15$nm above the feed point $(x_0 = -75$nm, $y_0 = 55$nm$)$. The magnitude and phase of the radiated field components, the phase difference between them and the AR are given for different θ angles (dipole orientations) in Figure 5-12. At $\theta = 85^o$ $|E_y|/|E_x| = 1.05$ and $\phi_y - \phi_x = -254^o$, hence CP radiation is noted.
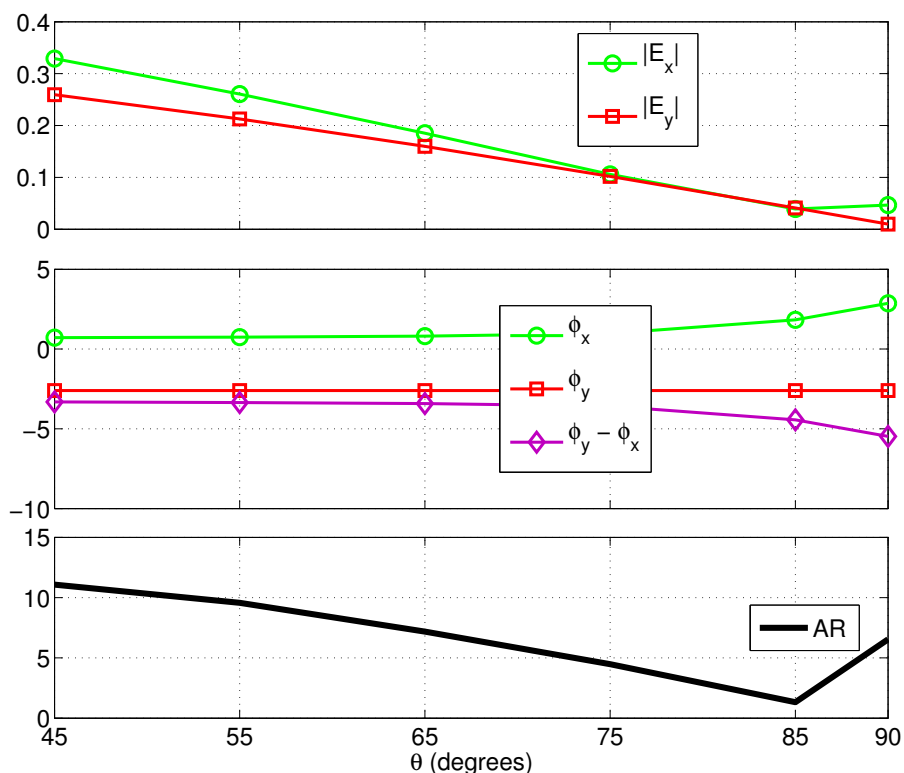
Figure 5-12: The magnitude, phase difference between the x and y components of the radiated electric field and the AR) observed computationally for an optical patch antenna fed from the vicinity of $(x_0 = -95$nm, $y_0 = 55$nm, $z_0 = -15$nm$)$ with respect to different dipole orientations (θ).

The phases of the x component changes since it can couple to HED as well as VED, whereas the y component can only couple to VED. As seen in Figures 5-11,5-12 ϕ_y does not change with dipole orientation but due to the changes in ϕ_x CP can be observed. Unless a phase difference of odd multiples of 90° is observed by default at a particular dipole orientation CP cannot be achieved by only changing the dipole's location on the optical antenna.

In order to have control over CP operation for the optical patch antennas via an analytical approach inspired by the cavity model, the new degree of freedom, the polarization of the emitter, needs to be considered in addition to its projected location on the patch.

Conclusion

Knowing the current distribution of a mode of an equivalent cavity guides us where to locate the surce in order to excite that mode, and provides intuition on how to tune the resonance, radiation pattern and the polarization. In the fifth chapter the tuning of the resonant frequency and the feeding for the CP operation are discussed under the light of the cavity model. The tuning of the resonance by introducing slots on the patch is proven to work as expected by the cavity model, yet needs to be further studied in order to count in various slot sizes. CP operation research launches a new degree of freedom, the orientation of the source, different from the RF point of view where the CP is obtained upon feeding the antenna from specific locations.

Chapter 6

Discussions and Future Work

There has been a tremondous work on the optical antennas and their applications [12–25] following the introduction of the nm-accuracy fabrication techniques. The optical antennas, up to now, mainly inherited the RF antenna geometries with some fundamental characteristics but none of the design and analysis tools that may provide intuition in development and understanding of such structures. Motivated from such an intense study and the possibility of widespread use of antennas, and the need for a design tool that builds intuition on the operation in optics, in this study we have introduced the cavity model for optical patch antenna design with a computational aspect. The full-wave computational techniques like FEM, FDTD and MoM [26–29] are impenetrable and incapable of providing any intuition to users as compared to the cavity model, that provides advancement in design, analysis and understanding of the patch antennas.

In the cavity model analysis [35–38], the patch antenna is treated as a cavity formed by the patch and the ground plane enclosed laterally by the slot-type radiators with the resonating field inside, which is equivalent to the patch with the resonating current on. Inspired by this assessment, in this study, we have initiated an establishment, or some sort of mapping, of the cavity model to the optical domain as such, this study opens a new gateway full of new design approaches and intutions in optical antennas. The integrity of the cavity model in RF, which assists efficient analysis and design of the antenna, is maintained while providing intuition upon the

operation, determination of the limitations in the performance of the antenna, and in the development of new antenna configurations or modifications to an existing antenna design.

The differences between the two frequency domains, RF and optics, are examined and necessary modifications for the use of assistance of the cavity model in optics are introduced. The cavity in optics is formed via the SPPs that replace the surface currents in RF. For a free standing rectangular optical patch antenna, the resonance in the optics is defined and the structure is designed to operate at its intrinsic resonant wavelength. With the intuition gained from the caviy model, the designed optical patch antenna is fed for specific mode excitations and analyses showed high correlations to cavity model predictions in the mode distributions and correspondingly, in the radiation patterns.

Cavity model is valid for various patch antenna shapes and with various feeding configurations. In the future, the mode excitations with the correspondent radiation patterns will be investigated in order to prove the theorem for other canonical shapes as well. The main consideration for doing so, is the complex reflection coefficient calculations in those shapes. The cavity model is proven to work accurately for rectangular optical patch antennas, which is sufficient for a proof of principle. Other excitation techniques, like plane wave excitation on a slot feed, might have better practicality in doing experiments, compared to excitation via coupling of a single emitter in a precise feed location which requires optical trapping and accurate positioning of single quantum emitters.

Based on the study of the current distributions on and the radiation patterns from the rectangular patches, we have established that the optical patch antennas can be designed by using the cavity model, where we defined the dimensions of the patch according to the intended frequency of operation and the feed locations for intended radiation pattern and polarization. The frequency tuning by introducing a slot on the patch and its circuit equivalent have been successfully demonstrated in the optical regime. In the future, slots of different widths and lengths need to be further studied since there is complex behavior due to the coupling between the parallel plates in

addition to some other possible mechanisms that need to be clarified.

Another attractive feature of patch antennas, the ability to produce and control the polarization by simply selecting the feed position, is considered to be an important tool for sensing and imaging applications in optics, hence, we have studied the CP excitation and observed that there is a new degree of freedom, the orientation of the feed, introduced for optical patches. Direct implementation of the cavity model based analytical approach was not able to yield the feed positions in optics, since it analyzes the optical patch antenna for VED feed as that is the optical analogue of a probe feed.

As we have mentioned that a metal patch over a dielectric substrate, or a metal patch over a dielectric substrate backed by another metal plane can also be considered as an optical patch antenna suitable for the cavity model, these structures will be investigated in the future. For the MIM case especially, due to a new degree of freedom which is the thickness of the insulator, it is possible to have very small-scale antennas with sizes around 20 times smaller then the operating wavelength [66].

Another idea to be explored in the future is the design of dual mode antennas with the advantage of the coupling of the SPPs in symmetric MIM and IMI structures. Two different SPPs (symmetric and asymmetric) a symmetric structures supports, by arranging the antenna resonant lengths correspondingly for each SPP, can both resonate by a single feed.

To sum up, the main focus throughout this study has been the transfer of knowledge for the patch antennas in RF into optics with special emphasis given to the cavity model, a simulation tool that has been the most popular, intuitive and accurate enough for RF patch antennas. Since the cavity model was originally proposed and developed for the patch antennas that are surrounded by perfect electrical and magnetic conductors, mapping it into optics, where metals are no longer perfect conductors has been proposed. It has been observed that the cavity model equivalent in optics has achieved the intended goal, providing intuition on the operation of the patch antennas. That is, the current distribution on the patch and the associated radiation patterns can now be imagined for a given location of the feed in optics as

well. The same analysis and intuitions can now be carried onto a range of patch geometries, in addition, some tools like adding slot to tune the resonance and designing CP operation have been proposed and implemented in optics.

Chapter 7

Appendices

7.1   Appendix A - Complex Dielectric Function

Drude model and the interband transition contributions are discussed in the Light-Matter Interaction chapter for the dispersive nature of metals in the optical regime. Here, the Drude model expressions reinforced with the interband transitions are supplied for gold, silver, aluminum and nickel. The expressions are derived according to and valid for the wavelength representations normalized to **nm** and the corresponding angular frequency representation in **eV**.

The complex dielectric function, $\epsilon(\omega)$, observed via Drude model with the reinforcement of the first interband transition is given in (7.1) for gold and silver, where $\epsilon_r = 5.967$, $\omega_p = 8.729$, $\gamma = 0.065$, $\Delta = 1.09$, $\Phi = 2.684$ and $\Gamma = 0.433$ for gold and $\epsilon_r = 4.6$, $\omega_p = 9$, $\gamma = 0.07$, $\Delta = 1.1$, $\Phi = 4.9$ and $\Gamma = 1.3$ for silver.

$$\epsilon(\omega) \quad = \epsilon_r - \left(\frac{\omega_p^2}{\omega_0(\omega_0+i\gamma)}\right) - \left(\frac{\Delta\Phi^2}{(\omega_0^2-\Phi^2+i\omega_0\Gamma)}\right) \tag{7.1}$$

For nickel and aluminum higher order interband transitions are considered for more accurate results. The complex dielectric function, $\epsilon(\omega)$, for nickel is given in (7.2) where $\epsilon_r = 1$, $\omega_{p0} = 4.62$, $\gamma_0 = 0.021$, $\omega_{p1} = 6.929$, $\gamma_1 = 1.77$, $\omega_{p2} = 7.06$, $\gamma_2 = 3.44$, $\Gamma_0 = 1.02$, $\Phi_0 = 1.46$, $\Delta_0 = 2.1$, $\Gamma_1 = 2.41$, $\Phi_1 = 3.44$, $\Delta_1 = 1.2$.

$$\epsilon(\omega) = \qquad \epsilon_r - \left(\frac{\omega_{p0}^2}{\omega_0(\omega_0+i\gamma_0)}\right) - \left(\frac{\omega_{p1}^2}{\omega_0(omega_0+i*\gamma_1)}\right) - \qquad (7.2)$$

$$\left(\frac{\omega_{p2}^2}{\omega_0(omega_0+i\gamma_2)}\right) - \left(\frac{\Delta_0\Phi_0^2}{(\omega_0^2-\Phi_0^2+i\omega_0\Gamma_0)}\right) - \left(\frac{\Delta_1\Phi_1^2}{(\omega_0^2-\Phi_1^2+i\omega_0\Gamma_1)}\right)$$

The complex dielectric function, $\epsilon(\omega)$, for aluminum is given in (7.3) where $\epsilon_r = 1$, $\omega_{p0} = 10.83$, $\gamma_0 = 0.047$, $\Gamma_0 = 0.333$, $\Phi_0 = 0.162$, $\Delta_0 = 1940.97$, $\Gamma_1 = 0.312$, $\Phi_1 = 1.544$, $\Delta_1 = 4.706$, $\Gamma_2 = 1.35$, $\Phi_2 = 1.808$, $\Delta_2 = 11.39$, $\Gamma_3 = 3.382$, $\Phi_3 = 3.473$, $\Delta_3 = 0.558$.

$$\epsilon(\omega) = \quad \epsilon_r - \left(\frac{\omega_{p0}^2}{\omega_0(\omega_0+i\gamma_0)}\right) - \left(\frac{\Delta_0\Phi_0^2}{(\omega_0^2-\Phi_0^2+i\omega_0\Gamma_0)}\right) - \left(\frac{\Delta_1\Phi_1^2}{(\omega_0^2-\Phi_1^2+i\omega_0\Gamma_1)}\right) - \qquad (7.3)$$

$$\left(\frac{\Delta_2\Phi_2^2}{(\omega_0^2-\Phi_2^2+i\omega_0\Gamma_2)}\right) - \left(\frac{\Delta_3\Phi_3^2}{(\omega_0^2-\Phi_3^2+i\omega_0\Gamma_3)}\right)$$

The experimentally obtained Johnson and Christy data for gold and silver are given below in tables (7.1) and (7.2) respectively, for three columns showing to the λ (μm), $re\{n\}$, $im\{n\}$ where n is the refractive index.

Table 7.1: Johnson and Christy data for gold

0.1879 1.28 1.188
0.1916 1.32 1.203
0.1953 1.34 1.226
0.1993 1.33 1.251
0.2033 1.33 1.277
0.2073 1.30 1.304
0.2119 1.30 1.350
0.2164 1.30 1.387
0.2214 1.30 1.427
0.2262 1.31 1.460
0.2313 1.30 1.497
0.2371 1.32 1.536
0.2426 1.32 1.577
0.2490 1.33 1.631
0.2551 1.33 1.688
0.2616 1.35 1.749
0.2689 1.38 1.803
0.2761 1.43 1.847
0.2844 1.47 1.869
0.2924 1.49 1.878
0.3009 1.53 1.889
0.3107 1.53 1.893
0.3204 1.54 1.898
0.3315 1.48 1.883
0.3425 1.48 1.871
0.3542 1.50 1.866
0.3679 1.48 1.895
0.3815 1.46 1.933
0.3974 1.47 1.952
0.4133 1.46 1.958
0.4305 1.45 1.948
0.4509 1.38 1.914
0.4714 1.31 1.849
0.4959 1.04 1.833
0.5209 0.62 2.081
0.5486 0.43 2.455
0.5821 0.29 2.863
0.6168 0.21 3.272
0.6595 0.14 3.697
0.7045 0.13 4.103
0.7560 0.14 4.542
0.8211 0.16 5.083
0.8920 0.17 5.663
0.9840 0.22 6.350
1.0880 0.27 7.150
1.2160 0.35 8.145
1.3930 0.43 9.519
1.6100 0.56 11.21
1.9370 0.92 13.78

Table 7.2: Johnson and Christy data for silver

0.1879 1.07 1.212
0.1916 1.10 1.232
0.1953 1.12 1.255
0.1993 1.14 1.277
0.2033 1.15 1.296
0.2073 1.18 1.312
0.2119 1.20 1.325
0.2164 1.22 1.336
0.2214 1.25 1.342
0.2262 1.26 1.344
0.2313 1.28 1.357
0.2371 1.28 1.367
0.2426 1.30 1.378
0.2490 1.31 1.389
0.2551 1.33 1.393
0.2616 1.35 1.387
0.2689 1.38 1.372
0.2761 1.41 1.331
0.2844 1.41 1.264
0.2924 1.39 1.161
0.3009 1.34 0.964
0.3107 1.13 0.616
0.3204 0.81 0.392
0.3315 0.17 0.829
0.3425 0.14 1.142
0.3542 0.10 1.419
0.3679 0.07 1.657
0.3815 0.05 1.864
0.3974 0.05 2.070
0.4133 0.05 2.275
0.4305 0.04 2.462
0.4509 0.04 2.657
0.4714 0.05 2.869
0.4959 0.05 3.093
0.5209 0.05 3.324
0.5486 0.06 3.586
0.5821 0.05 3.858
0.6168 0.06 4.152
0.6595 0.05 4.483
0.7045 0.04 4.838
0.7560 0.03 5.242
0.8211 0.04 5.727
0.8920 0.04 6.312
0.9840 0.04 6.992
1.0880 0.04 7.795
1.2160 0.09 8.828
1.3930 0.13 10.10
1.6100 0.15 11.85
1.9370 0.24 14.08

7.2 Appendix B - Derivation of the Cavity Model

The thickness of the patch is very small $(d << \lambda)$. So the field variations along the height are constant and the fringing fields along edges of the patch are small. The electric field is normal to the surface patch which means that the patch only supports TM_z configurations within the cavity. We have $E = \hat{z} E_z(x,y)$ whereas $E_x = E_y = 0$ and J_z for the probe feeding case.

First, take the Faraday Equation

$$\nabla \times E = -j\omega\mu H \tag{7.4}$$

$$\begin{vmatrix} \hat{x} & \hat{y} & \hat{z} \\ \frac{\partial}{\partial x} & \frac{\partial}{\partial y} & \frac{\partial}{\partial z} \\ 0 & 0 & E_z \end{vmatrix} = -j\omega\mu(\hat{x}H_x + \hat{y}H_y)$$

$$\tag{7.5}$$

from where we get 2 equations

$$\frac{\partial E_z}{\partial y} = -j\omega\mu H_x \text{ and } -\frac{\partial E_z}{\partial x} = -j\omega\mu H_y. \tag{7.6}$$

Solving Equation 7.6 under the boundary conditions 7.7

$$H_x(x, y = 0) = H_x(x, y = b) = 0$$

$$H_y(x = 0, y) = H_y(x = a, y) = 0 \tag{7.7}$$

we can write E_z as a superposition of all orthonormal modes Ψ_{mn} as :

$$E_z = \sum_{m,n=0}^{\infty} E_{mn}\Psi_{mn} \tag{7.8}$$

Solving the Ampere's law with the same methodology and introducing the electric current J_z into all the equations one can easily obtain the field components as:

$$E_z(x, y) = -i\omega\mu I_0 l \sum_{m,n=0}^{\infty} \frac{\Psi_{mn}(x_0, y_0)}{k^2 - k_{mn}^2} \Psi_{mn} sinc(\frac{m\pi l}{2a}) \tag{7.9}$$

The mode with the lowest order resonant frequency is the dominant mode. The surface current distributions on the patch surface J_x and J_y can be obtained through H_y and H_x from E_z.

Standing wave is a wave that remains in a constant position. In patch antennas, standing wave occurs as a result of the interference between two waves traveling in opposite directions. The wave from one end is made to reflect from the other end, so the transmitted and the reflected waves superpose forming a standing wave pattern.

The electric field is zero at the center of the patch, maximum (positive) at one side, and minimum (negative) on the opposite side. It should be mentioned that the minimum and maximum continuously change sides according to the instantaneous phase of the applied signal. The electric field does not stop abruptly at the patch's periphery as in a cavity; rather, the fields extend the outer periphery to some degree. These field extensions are known as fringing fields and cause the patch to radiate.

For a rectangular patch antenna $\Psi_{mn}(x, y) \approx cos(m\pi x/a)cos(n\pi y/b)$. The far field components of the radiated electromagnetic field from the antenna can be calculated from

$$E(\hat{r}) = \frac{-i\omega\mu e^{jkr}}{4\pi r\eta}\hat{r} \times \oint ds' e^{-ik\hat{r}\cdot\hat{r}'} \bar{M}_s(\hat{r}') \tag{7.10}$$

where M_s can be obtained via

$$\bar{M}_s = \hat{x}2[E_z(x,0)\delta(y) - E_z(x,b)\delta(y-b)][U(x) - U(x-a)] + \tag{7.11}$$
$$\hat{y}2[E_z(a,y)\delta(x-a) - E_z(0,y)\delta(x)][U(y) - U(y-b)]$$

Bibliography

[1] B. R. Green and W. W. Parson, editors. *Light-Harvesting Antennas in Photosynthesis*, volume 13 of *Advances in photosynthesis and respiration*. Kluwer Academic Publishers, Dordrecht, The Netherlands, 2003.

[2] Y. T. Lo and S. W. Lee. *Antenna Handbook*. Van Nostrand Reinhold Company, New York, 1988.

[3] C. A. Balanis. *Antenna Theory: Analysis and Design*. John Wiley & Sons, Inc., New York, 2 edition, 1997.

[4] J. J. Carr. *Practical Antenna Handbook*. McGraw-Hill/TAB Electronics, 4 edition, 2001.

[5] J. D. Kraus and R. J. Marhefka. *Antennas for all Applications*. McGraw-Hill Book Company, 3 edition, 2001.

[6] R. D. Grober, R. J. Schoelkopf, and D. E. Prober. Optical antenna: Towards a unity efficiency near-field optical probe. *Appl. Phys. Lett.*, 70:1354–1356, Mar. 1997.

[7] D. W. Pohl. Near field optics seen as an antenna problem. In M. Ohtsu and X. Zhu, editors, *Near-Field Optics: Principles and Applications*, pages 9–21. World Scientific, Singapore, 2000.

[8] C. Fumeaux, M. A. Gritz, I. Codreanu, W. L. Schaich, F. J. Gonzalez, and G. D. Boreman. Measurement of the resonant lengths of infrared dipole antennas. *Infrared Phys. Technol.*, 41(5):271–281, Oct. 2000.

[9] J. N. Farahani, D.W. Pohl, H. J. Eisler, and B. Hecht. Single quantum dot coupled to a scanning optical antenna: A tunable superemitter. *Phys. Rev. Lett.*, 95(1):017402, June 2005.

[10] P. J. Schuck, D. P. Fromm, A. Sundaramurthy, G. S. Kino, and W. E. Moerner. Improving the mismatch between light and nanoscale objects with gold bowtie nanoantennas. *Phys. Rev. Lett.*, 94(1):017402, Jan. 2005.

[11] P. Muhlschlegel, H.J. Eisler, O. J. F. Martin, B. Hecht, and D. W. Pohl. Resonant optical antennas. *Science*, 308:1607–1609, June 2005.

[12] T. H. Taminiau, R. J. Moerland, F. B. Segerink, L. Kuipers, and N. F. van Hulst. $\lambda/4$ resonance of an optical monopole antenna probed by single molecule fluorescence. *Nano Lett.*, 7(1):28–33, Jan. 2007.

[13] L. Novotny. Effective wavelength scaling for optical antennas. *Phys. Rev. Lett.*, 98:266802, June 2007.

[14] Y. Alaverdyan, B. Sepulveda, L. Eurenius, E. Olsson, and M. Kall. Optical antennas based on coupled nanoholes in thin metal films. *Nature Phys.*, 3:884–889, Nov. 2007.

[15] G. Kino. Optical antennas: Tuning in to optical wavelengths. *Nature Photonics*, 2(4):210–211, Apr. 2008.

[16] T. H. Taminiau, F. D. Stefani, F. B. Segerink, and N. F. van Hulst. Optical antennas direct single-molecule emission. *Nature Photonics*, 2(4):234–237, Apr. 2008.

[17] J. Merlein, M. Kahl, A. Zuschlag, A. Sell, A. Halm, J. Boneberg, P. Leiderer, A. Leitenstorfer, and R. Bratschitsch. Nanomechanical control of an optical antenna. *Nature Photonics*, 2(4):230–233, April 2008.

[18] A. Kinkhabwala, Z. Yu, S. Fan, Y. Avlasevich, K. Mullen, and W. E. Moerner. Large single-molecule fluorescence enhancement produced by a bowtie antenna. *Nature Photonics*, 3:654–657, 2009.

[19] P. Bharadwaj, B. Deutsch, and L. Novotny. Optical antennas. *Adv. Opt. Photon.*, 1:438–483, 2009.

[20] T. Kosako, Y. Kadoya, and H. F. Hofmann. Directional control of light by a nano-optical yagi-uda antenna. *Nature Photonics*, 4:312–315, 2010.

[21] J. Dorfmuller, R. Vogelgesang, W. Khunsin, C. Rockstuhl, C. Etrich, and K. Kern. Plasmonic nanowire antennas: experiment, simulation, and theory. *Nano Letters*, 10, 2010.

[22] L. Novotny and N. van Hulst. Antennas for light. *Nature Photonics*, 5:83–90, February 2011.

[23] L. Yousefi and A. Foster. Waveguide-fed optical hybrid plasmonic patch nano-antenna. *Optics Express*, 20(16):18326–18335, 2012.

[24] M. Agio and A. Alu. *Optical Antennas.* Cambridge University Press, 2013.

[25] L. Peng and N. A. Mortensen. Plasmonic-cavity model for radiating nano-rod antennas. *Nature Scientific Reports*, 4, 2014.

[26] J. Jin. *The finite element method in electromagnetics.* John Wiley & Sons, 2014.

[27] K. S. Kunz and R. J. Luebbers. *The Finite Difference Time Domain Method for Electromagnetics.* CRC Press, 1993.

[28] A. Taflove. *Computational Electrodynamics.* Artech House, Norwood, MA, 1995.

[29] R. F. Harrington and J. L. Harrington. *Field Computation by Moment Methods.* Oxford University Press, 1996.

[30] A. Alu and N. Engheta. Theory, modeling and features of optical nanoantennas. *IEEE transactions on antennas and propagation*, 61(4):1508–1517, 2013.

[31] G. A. Deschamps. Microstrip microwave antennas. presented at the Third USAF Symp. on Antennas, 1953.

[32] R. E. Munson. Flat aerial for ultra high frequencies. U.S. Patent no. 3 921 177 113, November 1975.

[33] K. F. Lee and W. Chen, editors. *Advances in Microstrip and printed antennas.* John Wiley & Sons, Inc., New York, 1997.

[34] D. Guha and Y. M. M. Antar, editors. *Microstrip and printed antennas: new trends, techniques and applications.* John Wiley & Sons Ltd., 2011.

[35] S. L. Chuang, L. Tsang, and W. C. Chew. The equivalence of the electric and magnetic surface current approaches in microstrip antenna studies. *IEEE Trans. on Antennas and Prop.*, 28(4), 1980.

[36] W.F. Richards, Y.T. Lo, and D. D. Harrison. Improved theory for microstrip antennas. *Electronics Letters*, 15(2):42–44, January 1979.

[37] Y. T. Lo, D. Solomon, and W. F. Richards. Theory and experiment on microstrip antennas. *IEEE Trans. Antennas Propag.*, 27:137–145, March 1979.

[38] W. F. Richards, Y. T. Lo, and Daniel D. Harrison. An improved theory for microstrip antennas and applications. *IEEE Trans. Antennas Propag.*, 29:38–46, January 1981.

[39] H. G. Frey, S. Witt, K. Felderer, and R. Guckenberger. High-resolution imaging of single fluorescent molecules with the optical near-field of a metal tip. *Phys. Rev. Lett.*, 93(20):200801, Nov. 2004.

[40] P. Bharadwaj, P. Anger, and L. Novotny. Introducing defects in 3d photonic crystals: state of the art. *Nanotechnology*, 18(4):044017, Jan. 2007.

[41] B. Berland. Photovoltaic technologies beyond the horizon: Optical rectenna solar cell. Technical report, ITN Energy Systems, 2002.

[42] Nano antenna photo voltaic cells. http://www.inl.gov/featurestories/2007-12-17.shtml, Jan. 2008.

[43] E. J. Smythe E. Cubukcu and Federico Capasso. Optical properties of surface plasmon resonances of coupled metallic nanorods. *Optics Express*, 15(12):7439–7447, June 2007.

[44] N. Yu and F. Capasso. Flat optics with designer metasurfaces. *Nature Materials*, 13:139–150, February 2014.

[45] Y. Yao, R. Shankar, P. Rauter, Y. Song, J. Kong, M. Loncar, and F. Capasso. High-responsivity mid-infrared graphene detectors with antenna-enhanced photocarrier generation and collection. *Nano Letters*, 14, June 2014.

[46] R. Kappeler, D. Erni, C. Xudong, and L. Novotny. Field computations of optical antennas. *Journal of Computational and Theoretical Nanoscience*, 4:686–691, 2007.

[47] H. Gao, K. Li, F. M. Kong, H. Xie, and J. Zhao, editors. *Optimizing nano-optical antenna for the enhancement of spontaneous emission*. Progress in Electromagnetics Research, JPIER, 2010.

[48] R. Esteban, T. V. Teperik, and J. J. Greffet. Optical patch antennas for single photon emission using surface plasmon resonances. *Phys. Rev. Lett.*, 104:026802, Jan 2010.

[49] C. Belacel, B. Habert, F. Bigourdan, F. Marquierand J.P. Hugonin, S. M. de Vasconcellos, X. Lafosse, L. Coolen, C. Schwob, C. Javaux, B. Dubertret, J.J. Greffet, P. Senellart, and A. Maitre. Controlling spontaneous emission with plasmonic optical patch antennas. *Nano Letters*, 13, March 2013.

[50] C. Ciraci, J. B. Lassiter, A. Moreau, and D. R. Smith. Quasi-analytic study of scattering from optical plasmonic patch antennas. *Journal of Appl. Phys.*, 114(163108):1516–1521, 2013.

[51] A. Mekis, J. C. Chen, I. Kurland, S. Fan, P. R. Villeneuve, and J. D. Joannopoulos. High transmission through sharp bends in photonic crystal waveguides. *Phys. Rev. Lett.*, 77:3787–3790, Oct 1996.

[52] S. A. Maier, M. L. Brongersma, P. G. Kik, S. Meltzer, A. A. G. Requicha, and H. A. Atwater. Plasmonics - a route to nanoscale optical devices. *Advanced Materials*, 13(19):1501–1505, Oct 2001.

[53] R. Feynman. There's plenty of room at the bottom. APS Meeting, 1959.

[54] L. Novotny and B. Hecht. *Principles of Nano-Optics*. Cambridge Univ. Press, 2006.

[55] P. Drude. Elektronentheorie der metalle. *Annalen der Physik*, 1:566–613, Feb 1900.

[56] G. V. Naik, V. M. Shalaev, and A. Boltasseva. Alternative plasmonic materials: Beyond gold and silver. *Advanced Materials*, 25(24):3264–3294, 2013.

[57] P. B. Johnson and R. W. Christy. Optical constants of the noble metals. *Phys. Rev. B*, 6:4370–4379, Dec 1972.

[58] R. H. Ritchie. Plasma losses by fast electrons in thin films. *Physical Review*, 106(5):874–881, 1957.

[59] C. J. Powell and J. B. Swan. Origin of the characteristic electron energy losses in aluminum. *Phys. Rev.*, 115:869–875, Aug 1959.

[60] C. J. Powell and J. B. Swan. Origin of the characteristic electron energy losses in magnesium. *Phys. Rev.*, 116:81–83, Oct 1959.

[61] E. A. Stern and R. A. Ferrell. Surface plasma oscillations of a degenerate electron gas. *Phys. Rev.*, 120:130–136, Oct 1960.

[62] W. L. Barnes, A. Dereux, and T. W. Ebbesen. Surface plasmon subwavelength optics. *Nature*, 424:824–830, 2003.

[63] S. A. Maier. *Plasmonics: Fundamentals and Applications*. Springer (New York), 2007.

[64] C. Clavero. Plasmon-induced hot-electron generation at nanoparticle/metal-oxide interfaces for photovoltaic and photocatalytic devices. *Nature Photonics*, 8, Feb 2014.

[65] E. T. Arakawa, M. W. Williams, R. N. Hamm, and R. H. Ritchie. Effect of damping on surface plasmon dispersion. *Phys. Rev. Lett.*, 31:1127–1129, Oct 1973.

[66] H. T. Miyazaki and Y. Kurokawa. Squeezing visible light waves into a 3nm thick and 55nm long plasmon cavity. *Physical Review Letters*, 96:097401, 2006.

[67] H. A. Atwater. The promise of plasmonics. *Scientific American*, 4:56–62, 2007.

[68] E. N. Economou. Surface plasmons in thin films. *Phys. Rev.*, 182(2):539–554, June 1969.

[69] N.Kinayman and M.I.Aksun. *Modern Microwave Circuits*. Artech House, Norwood, MA, 2005.

[70] PhotonicsGlobal@ Singapore, 2008. IPGC 2008. *Thickness dependent behavior of surface plasmon polaritons in layered media*. IEEE, 2008.

[71] C. F. Bohren and D. R. Huffman, editors. *Absorption and Scattering of Light by Small Particles*. John Wiley & Sons, Inc., New York, 1998.

[72] P. Anger, P. Bharadwaj, and L. Novotny. Enhancement and quenching of single-molecule fluorescence. *Physical Review Letters*, 96:113002, 2006.

[73] A. Chandran, E. S. Barnard, J. S. White, and M. L. Brongersma. Metal-dielectric-metal surface plasmon-polariton resonators. *Physical Review B*, B 85(085416), 2012.

[74] R. Gordon. Light in subwavelength slit in a metal : Propagation and reflection. *Physical Review B*, B 73(153405), 2006.

[75] E. S. Barnard, J. S. White, A. Chandran, and M. L. Brongersma. Spectral properties of plasmonic resonator antennas. *Optics Express*, 16, 2008.

[76] R. Zia, A. Chandran, and M. L. Brongersma. Dielectric waveguide model for guided surface polaritons. *Optics Letters*, 30(12):1473–1475, June 2005.

[77] R. Gordon. Vectorial method for calculating the fresnel reflection of surface plasmon polaritons. *Physical Review B*, B 74(153417), 2006.

[78] F. L. Pedrotti and L. Pedrotti. *Introduction to Optics*. Prentice-Hall Inc., NJ, 1987.

[79] J. Yang, C. Sauvan, A. Jouanin, S. Collin, J.L-Pelouard, and P. Lalanne. Ultra-small metal-insulator-metal nanoresonators : impact of slow-wave effects on the quality factor. *Optics Express*, 20(16880), 2012.

[80] M. W. Knight, N. K. Grady, R. Bardhan, F. Hao, P. Nordlander, and N. J. Halas. Nanoparticle-mediated coupling of light into a nanowire. *Nano Lett.*, 7(8):2346–2350, Aug. 2007.

[81] Lumerical Solutions, Inc. http://www.lumerical.com/tcad-products/fdtd/.

[82] W. Richards. An improved theory for microstrip patches. *IEE Proc.*, 132:93âĂŞ98, 1985.

[83] M. Ansarizadeh and A. Chorbani. An approach to equivalent circuit modeling of rectangular microstrip antennas. *Progress in Electromagnetics Research B*, 8, 2008.